The Effect of Prior Austenite Grain Size on Transformation Behaviour as a Function of Cooling Rate in Nuclear Pressure Vessel Steel SA508 G4N

By:

Hussain Alsalamah

A thesis submitted for the degree of Doctor of Philosophy

The University of Sheffield

Department of Material Science and Engineering

Supervisor

Professor Bradley P Wynne

Submission Date

JUL 2020

Abstract

A key element of many nations' future baseline energy supply is earmarked to be based on nuclear fission. A critical component of a civil nuclear reactor is the Reactor Pressure Vessel (RPV). The RPV is exposed to a harsh environment of high pressure and high temperature concurrently with neutron irradiation. The majority of RPVs in-service use low alloy steel grade SA508 Gr.3 (Mn–Mo–Ni) or its international equivalent. However, there is a drive to run at higher pressures and temperatures for future nuclear reactors, which requires higher RPV wall thicknesses than currently operating. This has led to the development of SA508 Gr.4N (Ni-Mo-Cr), which has higher hardenability, toughness, and strength, allowing for the design thickness of the reactor wall to be more than 200 mm, increasing the efficiency, power, and lifespan of the nuclear reactor to potentially well over 50 years. A potential major problem going to larger size RPVs will be a possible variation in Prior Austenite Grain Size (PAGS) generated because of the complex thermomechanical processing route the RPV material will experience and its interaction with varying cooling rates between the surface and centre during quenching. There has been much debate about the effect of PAGS on microstructure evolution in RPV materials, in particular the bainite transformation. In this research, the impact of PAGS on microstructure evolution during heat treatment has been investigated in order to understand the complex relations between processing, microstructure and physical properties to help understand if there are going to be complications during the operational stages of the RPV.

Austenitisation was undertaken at different times and temperatures to produce 3 different PAGS sizes, fine (23 μm), medium (84 μm), and coarse (412 μm). They were then subjected to three different cooling rates: 0.07 °C/s and 0.3 °C/s and 3 °C/s. A lath microstructure dominated at fine PAGS at the slowest cooling rate of 0.07 °C/s, while at the largest PAGS the microstructure was mostly granular bainite. The average bainitic lath width is inversely proportional to the size of the PAGS. A larger prior austenite grain size resulted in a greater volume fraction of granular bainite and blocky MA islands. A fully martensitic microstructure was present at the highest cooling rate of 3 °C/s for all PAGSs, while a combination of lower bainite and martensite were present at the intermediate cooling rate and increasing PAGS also lead to a slightly greater level of tempered martensite volume fraction.

The effect of tempering times (6h and 24h) at a tempering temperature of 550 °C was also studied. In case of the slowest cooling rate at 0.07 °C/s, bainitic lath width increases during the

tempering stage, also some laths coarsen and consume neighbouring laths and there is also some indication of laths bulging out. In addition, the carbides inside the coarse laths appear to be coarsening at a much faster rate than the fine carbides within a fine lath structure. Some of the martensite/austenite islands (MA) within granular bainite decomposed with tempering time to form new bainite and fresh carbides that increased the bainite volume fraction, while other untransformed MA increased its size and then disappeared with longer tempering times. Moreover, a larger PAGS led to a greater amount of carbide clusters forming at austenite triple junctions (for the longer tempering time), furthermore some of the blocky-like shape MA stabilised more than needle-like shape.

For certain martensitic regions of the microstructure, laths were observed coarsening, which consumed adjacent laths. At a cooling rate of 3 °C/s with tempering time, carbides were not seen in the medium PAGS. Carbides were observed at triple junction boundary for coarse PAGS with 6h tempering, and after 24h tempering in the fine prior austenite grains.

Increasing PAGS leads to decrease in the hardness value in the bainitic microstructure. On the other hand, increasing PAGS leads to an increase in the hardness values in the martensitic and mixture microstructures. Also, increasing cooling rates increases hardness as a result of transformation to a harder microstructural constituent.

Acknowledgements

First and foremost, I would love to eagerly express my profound thanks to Professor Bradley P Wynne supervisors for his supervision, enlightenment and encouragement throughout the course of my PhD study. Secondly, I would like to thank Professor M Jackson for his remarks and also for supporting me during my studies. I also want to thank all the technical staff in the Department of Materials Science and Engineering for assisting me to carry out my experiments and providing laboratory facilities and laboratory help, especially, Neil Hind, Tes Monaghan, Dean Haylock and Mike Bell. I want to express my thanks to the Ministry of Higher Education and Scientific Research in Saudi Arabia and its representative in the United Kingdom, Royal Embassy of Saudi Arabia Cultural Bureau. I am also appreciative to Saudi Standard, Metrology and Quality Organization (SASO) Riyadh for supported and giving me this opportunity to obtain a PhD. Many thanks to my friends in the group, Dr Ismail, Hasn, Sameer, Dr Ali, Eduardo, Raghdan, and Carl for their friendship, comments, and helpful advice throughout my PhD study. Finally, I would like to express my gratitude and appreciation to my family (father, mother, lovely sons -Abdulamala, Mubarak, Muaml-, my fabulous wife and my siblings) for their encouragement and supporting during the study.

Contents

List of Figures

List of tables

Nomenclature

A	Austenite solidification mode
AF	Austenite ferrite solidification mode
AISI	American Iron and Steel Institute
ASTM	American Society for Testing and Materials
BCC	Body Cantered Cubic
BM	Base Metal
BS	British Standard
CCT	Continuous Cooling Transformation
CAD	Computer Aided Design
DWR	Depth to Width Ratio
EBW	Electron Beam Welding
EDM	Electrical Discharged Machining
F	Ferrite
FA	Ferrite Austenite
FCC	Face Centred Cubic
DBTT	Ductile-brittle transition temperature
FZ	Fusion Zone
FTTU	Fast Thermal Treatment Unit
HAGBs	High Angle Grain Boundaries
HT	Heat treatment
HAZ	Heat Affected Zone
HCP	Hexagonal Closed Pack
IHT	Intercritical Heat Treatment
TP	Tempering parameter
USE	Upper shelf energy
TEM	TEM Transmission electron microscopy
EBSD	EBSD Electron backscatter diffraction
EDX	Energy dispersive X-ray
J	J-factor
Ae1	Lower temperature limit of the equilibrium ferrite-austenite phase field
Ae3	Upper temperature limit of the equilibrium ferrite-austenite phase field
Ac1	Temperature at which austenite begins to form during heating at a specified rate
Ac3	Temperature at which transformation of ferrite to austenite is completed during heating at a specified rate
f Mo2C	Volume fraction of Mo2C
D	Grain size (mm)
$D0$	Initial grain size (mm)
T	Holding time (sec)
T	Holding temperature (Kelvin)
LB	Lower Bainite
GB	Granular Bainite

PWR	Pressurised water reactor
Ms	Martensite Start Temperature
Mf	Martensite Finish Temperature
NAMR	Nuclear Advanced Manufacturing Research Centre
PWHT	Post Weld Heat Treatment
P	Pearlite
PH	Precipitation Hardened
QHT	Quality Heat Treatment
Q/V	Heat input per unit length
RPEBW	Reduced Pressure Electron Beam Welding
RPV	Reactor Pressure Vessel
R	Solidification rate
Rc1	Critical growth rate
Rc2	Higher growth rate
SA	Steel Alloy
SEM	Scanning Electron Microscopy
TMC	Thermomechanical Compression
TWI	The Welding Institute
VH	Vickers Hardness
UB	Upper Bainite
UTS	Ultimate Tensile Strength
WRC	Welding Research Council
XRD	Radiographic Inspection
Wt%	Weight Percentage
YS	Yield Strength
Q	Activation energy for grain growth
V	Boundary and migration velocity
M	Effective interface mobility
$Gint$	Driving force for interface movement
Vm	Molar volume
R	Universal gas constant
Dc	Critical carbide size
E	Young's modulus
$"p$	Surface energy
$T0$	Transition temperature
95% , CI 95%	Confidence interval
	Standard deviation
NLI	Number of linear intercept lines
% RA	Percent relative accuracy
LI	Average linear intercept
Ng	Number of measured grains
G	Gravitational acceleration
V	Volume fraction
D	Second phase particles size
L	Austenite grain size
h	Heat transfer coefficient
$Tmax$	Tempering temperature
Tth	Isothermal holding time for the tempering stage

1. Introduction & Industrial Context

1.1 Introduction

In recent years, the global population has rapidly increased, and with it the industrial sector grows and is expected to continue to rise within the coming decades. This will lead to a significant requirement for more energy generation, which if not addressed will lead to significant energy shortfalls across the globe. This shortage of energy power can be addressed by nuclear power, as it has the potential to solve the energy shortage with less ecological impact because of its lower green gas emissions, less fossil fuel consumption, reduced dependence on natural sources, less carbon dioxide being released, and is highly reliable and safe [1], [2]. There have been a large number of new nuclear power plants built recently in the world claiming zero carbon emission energy [3], [4]. Moreover, the United Kingdom is targeting to decrease carbon emissions by 80% by 2050, compared to 1990 levels, and there is a significant interest in new nuclear plant building [5]. Nuclear power stations are, however, expensive to build so a key element of making such systems viable is confidence in their long term operation, for example the new builds in the UK are planned to be operating for 60 years [6].

Reactor Pressure Vessels (RPV) are essential components at nuclear reactors. The RPV is a steel container with thick walls, employed to keep nuclear fuel inside and to work as a barrier to keep the radioactive matter from the outside environment. The vessel plays the primary role in deciding the life of the reactor power plant, it is a life limiting component – it cannot be replaced [6]. To avoid operational failure, optimal strength, toughness, and hardenability are desired [7]. Moreover, nuclear reactor capacity rises with expanding the RPV size, and this leads to an increase in the wall thickness of the RPV [8], [9]. In these circumstances, it is essential to consider the safety, the durability of a nuclear reactor and weldability besides optimal mechanical properties [7].

Manufacturing a nuclear vessel is a very challenging process, especially with increasing the vessel wall thickness, for instance the variation of the microstructure of RPV wall [10], [11]. During the heating and cooling fabrication process with thicker wall thickness, the cooling rates and temperature can vary through the thickness of the wall, and this variation will change the microstructures between the wall surface – (A) higher cooling rate -, and (B) the centre of the wall, - lower cooling rate -, Figure 1-1 [10]. Hence, the mechanical properties, as a

consequence of the variation of cooling rates, will vary through thickness, and this may lead to premature failure of the nuclear power plant [11].

Innumerable attempts have been made to develop new materials with good physical characteristics for structural critical systems in power generation applications. However, steel still proves to be the choice in nuclear power plants because it provides a good combination of properties, easy manufacturing routes, trustable materials, and is relatively cheap. The steel grade SA508 G3 has been utilized for more than 40 years in RPV designs [6], [8]. However, as a result of increasing the wall thickness in the next generation of reactors, manufacturing an RPV with SA508 G3 for a wall thickness around 300 mm will face difficulties as the cooling rate during quenching within the centre region will below the critical value for the formation of ferrite. This, in turn, will have a negative impact on toughness of the RPV [10]. Hence, future RPVs will require a new steel grade that can provide higher tensile stress and outstanding impact toughness with good hardenability and weldability.

A new steel grade SA508 Grade 4N has been developed that has higher toughness and tensile properties in comparison to Grade 3 [6], [7], [12]. To optimise steels mechanical properties, the heat treatment and chemical composition are the main factors to be considered. Toughness and strength can be significantly increased by changing the percentage of alloy elements such as Ni and Cr, which increase the hardenability and thus reduce the likelihood of ferrite formation [13]–[15]. SA508 Grade 4N has higher Ni and Cr levels than SA508 Grade 3 and has better mechanical properties and normally a finer grain size. This makes SA508 G4N an attractive candidate to be used in the nuclear industry due to its enhanced fabrication capabilities, higher mechanical properties, and weldability.

In this work we will investigate the effect of Prior Austenite Grain Size (PAGS) on transformation microstructure during quenching and subsequent tempering for SA508 G4N. PAGS can play a crucial part in predicting the mechanical properties of materials [16]. PAGS can be controlled by the chemical composition or heat treatment stages. In the case of SA508 G4N the chemical composition variability is limited because the range of alloying elements is restricted to the ASTM standards [17]. Consequently, heat treatment processes are the main way of controlling the grain size, either by increasing the austenitisation temperature or level of holding time at temperature. Furthermore, this study will focus on the decomposition of austenite to either baintite and martensite or both in the SA508 G4N under cooling conditions expected during manufacture of thick walled RPVs.

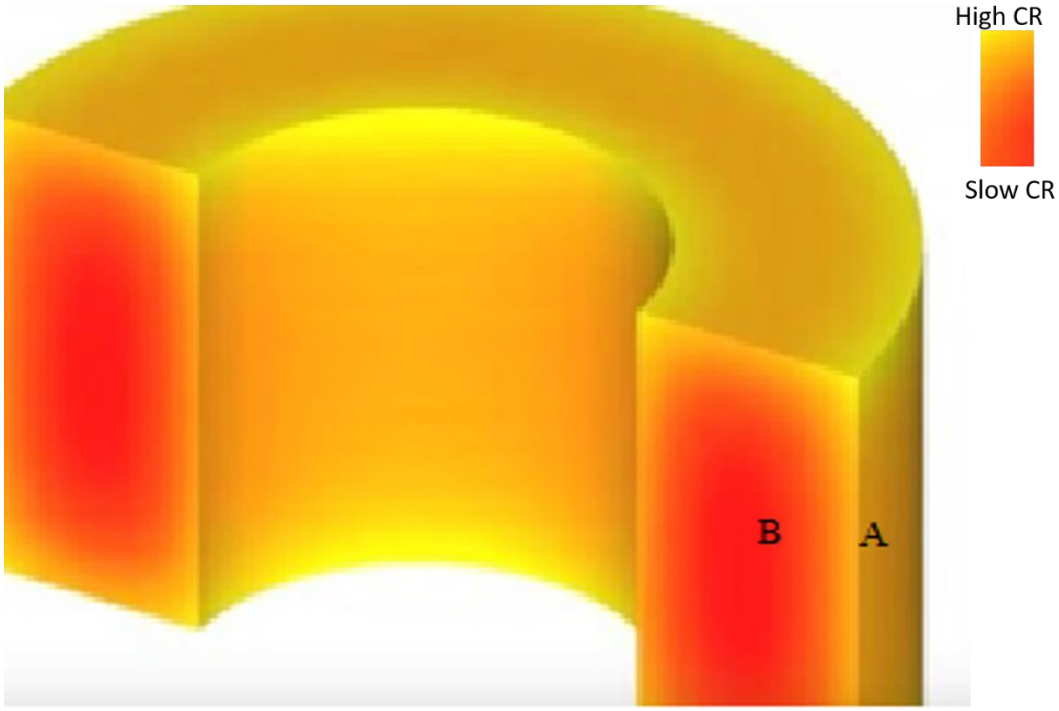

Figure 1-1: RPV variation of wall cooling rates (CR) during cooling stages (A) higher cooling rate, (B) lower cooling rate.

1.2 Aims

- The purpose of this study is to shed light on the transformation behaviour of austenite to bainite and martensite and explore the effect of the different cooling rate on the microstructures and mechanical characteristics of SA508 G4N steel for use in future RPV.
- It is crucial to understanding the effect of PAGS on transformation of austenite to bainite, mixture of bainite and martensite and fully martensite, by varying cooling rates with respect to prior sample heat-treatment regimes.

1.3 Thesis Outline

Chapter 2

The chapter will review the literature and background that has been studied by previous researcher, in addition to the alloys that employed in RPVs. Nuclear power plant history and the design requirements of the RPV are highlighted. Finally, the chapter will include a description of the current understanding of the effect of varying PAGS on transformed microstructure.

Chapter 3

The chapter describes the methodology of that were utilized in this project and designates the designs of the heat treatments. Moreover, this chapter delivers a description of the samples preparation in order to investigate the development in microstructure.

Chapter 4

This chapter provides the results and discussion of the development of microstructure with different cooling rates of as-cooled samples with material of RPVs SA508 G4N. In addition, it describes the effect of PAGS on the microstructure evolution as a function of cooling rates. This presents a detailed investigation of the microstructure in the as-cooled and in the heat treated state.

Chapter 5

The chapter delivers and explores the result of the effect of variation of quality heat treatment -tempering parameters- with variation of PAGS and its impact on the hardness.

Chapter 6

This chapter gives a brief overview of the main outcomes of this research, focused on the quality heat treatment as an example austenitisation temperature and tempering stage, to further understand the effect of PAGS on the microstructural evolution seen in SA508 G4N steel. Continued research objectives for future experimental work are stated.

2 Literature Review

2.1 Chapter Overview

This literature review covers the main background topics required to undertake the project and to achieve its aims and objectives. Firstly, nuclear power plant history and the design requirements of the RPV are highlighted, as well as future energy demands in the context of lower carbon emission requirements. This is then followed by how nuclear power plants can address future energy demands with thicker wall RPVs. However, it is shown that thicker walled RPVs come with issues during manufacture, with significant variation in cooling rate in the wall during heat treatment, leading to variation in properties using conventional materials. After that, an overview of High Strength Low Alloy (HSLA) steel and the decomposition of austenite to different microstructures during quality heat treatment is described. Finally, the chapter will conclude with a description of the current understanding of the effect of varying PAGS on transformed microstructure and its impact on mechanical properties.

2.2 Nuclear Power Plant

2.2.1 Nuclear Power Plant History

The potential of nuclear energy was first brought to the world's attention at the beginning of the last century by Ernst Rutherford and later by Albert Einstein. The first commercial nuclear plant that produced electricity was on the 20th December 1951 and it reached full power onto the grid in 1957. Between the 1950s to 1970s, a large number of new nuclear power plants were constructed, producing zero carbon emission energy [3], [4]. Moreover, The United Kingdom is aiming to decrease its carbon emission by 80% by 2050 in comparison to 1990 levels and this has led to a significant interest in new nuclear plant build [5]. This also appears to be happening in many parts of the world as well. According to the World Nuclear Association, 10.2 % of electricity energy is currently produced from civil nuclear plants (2019), Figure 2-1, and there are around 65 new nuclear power plants under construction [1], for example, Saudi Arabia, Nigeria, China, India, Chile, Vietnam and some European countries, Figure 2-2 [18].

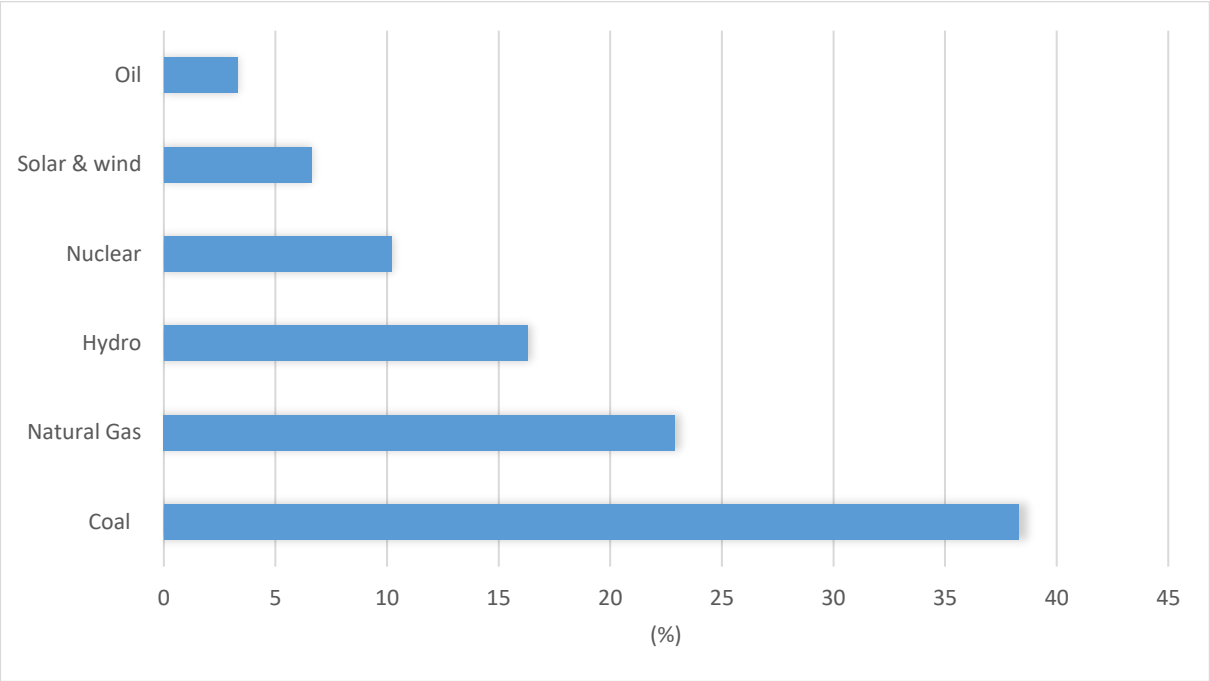

Figure 2-1 World electricity production 2019 [1].

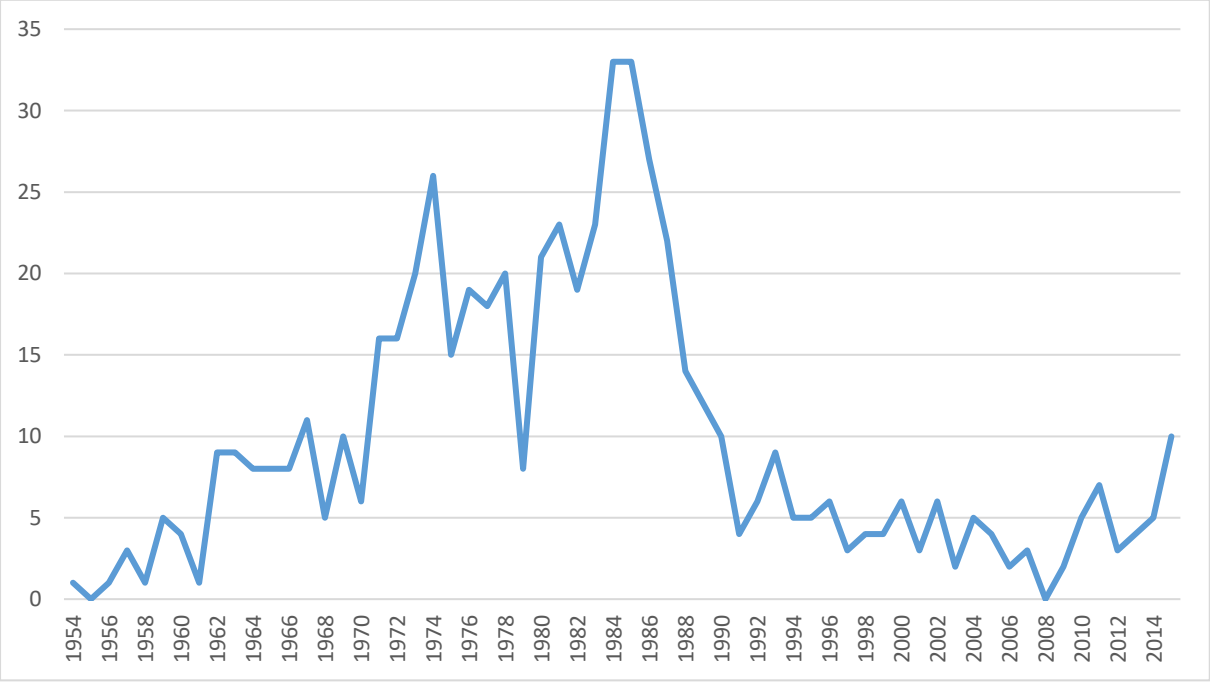

Figure 2-2 New nuclear power plants connected to the network in the world between (1954-2015) [18].

2.2.2 Reactor Pressure Vessel (RPV)

The Reactor Pressure Vessel (RPV) is a key component of the nuclear power plant, made of thick steel (> 150 mm wall thickness) and operating at pressures up to 17.5 MPa, employed to keep nuclear fuel inside safe and to work as a barrier to keep radioactive matter from the outside environment [19]. Optimisation of the design and manufacture of the RPV has been a continuous feature of all new nuclear builds in order to increase reactor capacity, lifetime and safety. The main driver for RPV research and development has been improvement in mechanical properties, e.g., toughness and strength as well as fabrication, weld quality. The RPV is a life limiting component of the plant and therefore maximising its structural integrity is key to maximising the life of the power plant. New generation reactors to be economically viable need to have a lifetime of 60 years and thus the RPV must have the design confidence to be operationally structurally sound for well over 60 years [8].

Manufacturing a nuclear RPV is a very challenging process, time consuming and costly because of the absolute necessity for a high level of quality assurance. They must be fabricated using guidelines that follow the American Society of Mechanical Engineers (ASME) Boiler and Pressure Vessel or an equivalent international designation. RPVs are constructed with steel according to the American Society for Testing and Materials (ASTM) SA508 standard for "Quenched and Tempered Vacuum-Treated Carbon and Alloy Steel Forgings for Pressure Vessels". Details of the two most recent variants of SA508 steels, SA508 grade 3 and grade 4N, chemistry and mechanical properties are given in Table 2-1 and Table 2-2. In addition, the ASME and ASTM standards provide some details of the manufacturing processes and heat treatment requirements but no normative rules to define what is good practice in the manufacture of the RPV to ensure that target properties are hit [17]. New RPVs are required to withstand an aggressive radiation environment at temperatures up to 350 °C and pressures up to 17.5 MPa [1], [20]. Key mechanical properties such as tensile strength and toughness are directly related to chemical composition and microstructure, which in turn, are sensitive to its manufacturing history, e.g., casting chemistry inhomogeneity, variation in recrystallisation during forging, and different cooling rates during quenching. Thus, it is key to understand the impact of different processing variables on microstructure of the SA508 grades of steels in order to maximise the lifetime of the RPV [20].

Table 2-1 Chemical composition regarding to ASTM 508 G3 and G4N, all in wt% [17].

SA508	C	Mn	Ni	Cr	Mo	Si	P	S	V	Cu	B	Ca	Ti	Al
G3	0.25<	1.2-1.5	0.4-1.00	0.25	0.45-0.6	0.4<	0.025	0.025	0.05	0.2	0.003	0.015	0.015	0.025
G4N	0.23<	0.2-0.4	2.8-3.9	1.5-2.00	0.4-0.6	0.4<	0.025	0.025	0.03	0.25	0.003	0.015	0.015	0.025

Table 2-2 Tensile and Charpy tests requirements [17].

SA508	Tensile strength (MPa)	Yield strength (MPa)	Elongation, %	Reduction of area, %	Charpy impact, Min of one sample(-29°C)	Charpy impact, Min average of three samples (-29°C)
G4N Cl1	725-895	585	18	45	30	35
G4N Cl2	975-965	690	16	45		
G4N Cl3	620-795	485	20	48		

2.2.3 High Strength Low Alloy Steel

Innumerable attempts have been made to develop new materials with good physical characteristics for structural critical systems in power generation applications. However, steel still proves to be the choice in nuclear power plants because it provides a good combination of mechanical properties, easy manufacturing routes and is relatively cheap [10], [14], [21].

High Strength Low Alloy (HSLA) steels have many standards and grades that are used in the nuclear industry to provide a long-life span and long-term safety in an aggressive environment, caused by high temperatures, high pressures and neutron irradiation [22], [11]. Additionally, this 'aggressive' environment caused by continuous neutron irradiation during operational life, weakens the material toughness [23]. HSLA steels attain their mechanical characteristics by adding a small quantity of alloying elements, which when combined with well-defined process conditions, results in a fine-grained microstructure with an excellent combination of strength and toughness. A key element of the process is control of the decomposition of austenite to equilibrium and non-equilibrium phases such as ferrite, bainite,

and martensite during final heat treatment. The next sections will describe these processes and microstructures in detail.

2.3 Phase Diagram and Equilibrium Phases of Steel

Figure 2-3 shows the iron-carbon phase equilibrium diagram and it represents the phases that are thermodynamically stable at a specific temperature and carbon content at a constant one atmosphere pressure. Phases in the diagram have distinct physical and mechanical properties, for instance, ferrite is relatively soft, while cementite is hard and brittle. Each specific section within the phase diagram represents the phase or phases for a certain alloy composition for instance, the phase area are the ferrite, cementite (Fe_3C), austenite, ferrite + cementite, ferrite + austenite, and austenite + cementite phase fields [24].

Pure iron is allotropic. At temperatures below 912 ºC iron is Body Centred Cubic (BCC) and is known as alpha-ferrite, between 912 ºC and 1394 ºC it has a Face Centred Cubic (FCC) structure known as gamma-austenite, and between 1394 ºC and 1538 ºC it returns to BCC, known as delta-ferrite. Steel alloys that have a low carbon content decompose from austenite through a Eutectoid reaction at 727 ºC to form a combination of low temperature alpha-ferrite and carbon rich cementite [24]. Typically, the morphology of the ferrite and cementite formed through the Eutectoid reaction is thin alternating lamellar of ferrite and cementite, that has a similar look to mother of pearl, and is known as pearlite.

2.4 Continuous Cooling Transformation of Austenite to Various Phases

During continuous cooling of steel, microconstituents can form which are not observed in the equilibrium phase diagram. The most common examples are martensite and bainite. These non-equilibrium phases transform from austenite under relatively rapid cooling conditions or when alloying elements are added to supress the formation of ferrite.

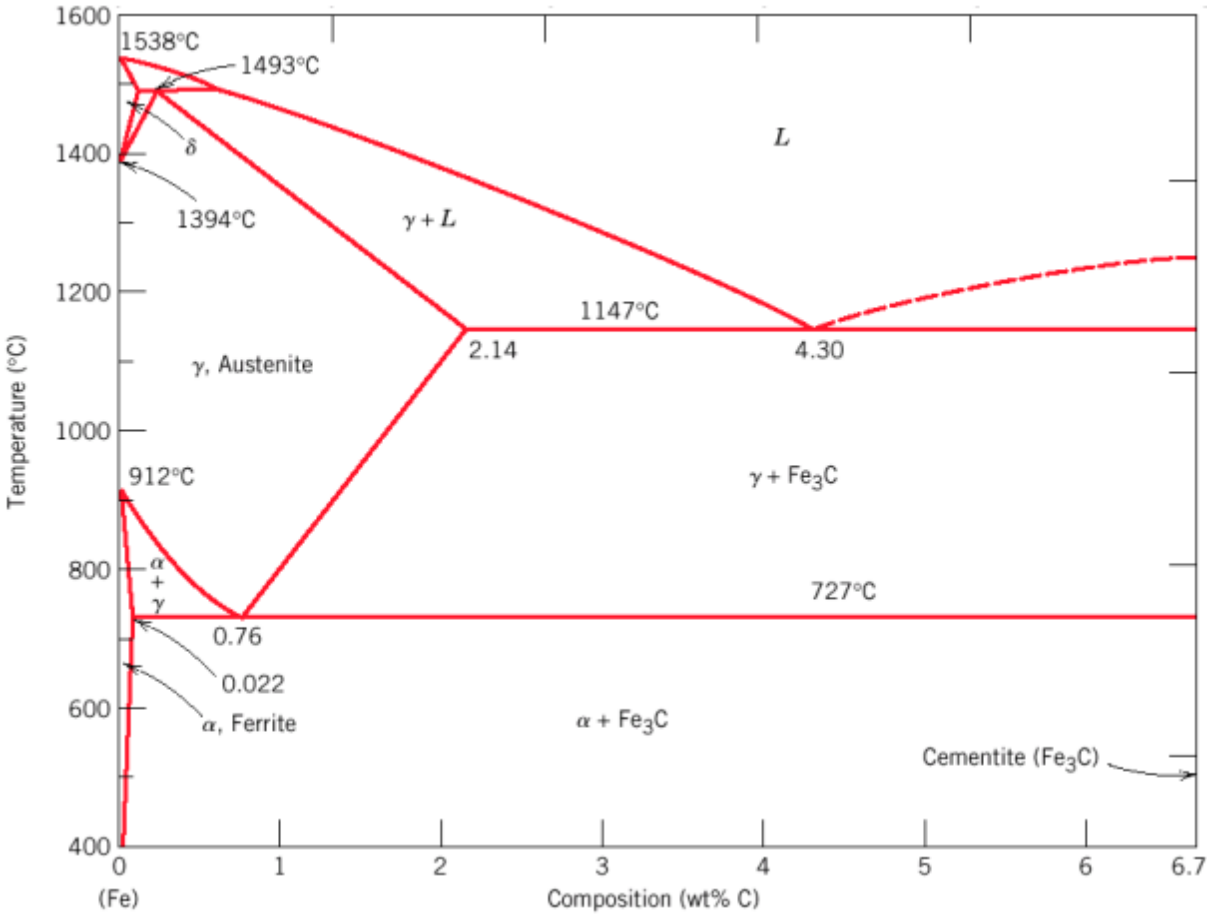

Figure 2-3 Iron-carbon equilibrium phase diagram [24].

The Continuous Cooling Transformation (CCT) diagram, Figure 2-4, describes the phases formed as a function of cooling rate for a specific composition of steel from a defined austenitisation temperature, for a specific austenite grain size. As shown in Figure 2-4, a HSLA like steel CCT diagram has 3 key features: 1. A high temperature ferrite/pearlite nose, which is only crossed at relatively slow cooling rates, 2. An intermediate bainite nose, and 3. A low temperature martensite field. The noses can be manipulated by the addition of alloying elements. For example, increasing elements such as manganese, chromium and nickel pushes the nose to the right of the diagram making it possible to form bainite and martensite at slower cooling rates [25]. This makes is possible to form these phases to a greater depth in larger components or to produce these phases at slower cooling rates, reducing the possibility of quench cracking. Changing Prior Austenite Grain Size (PAGS) also influences the nose location. By increasing the austenite grain size there are less potential nucleation sites for ferrite pushing the ferrite nose further to the right, making the formation of bainite or martensite more likely [18-20].

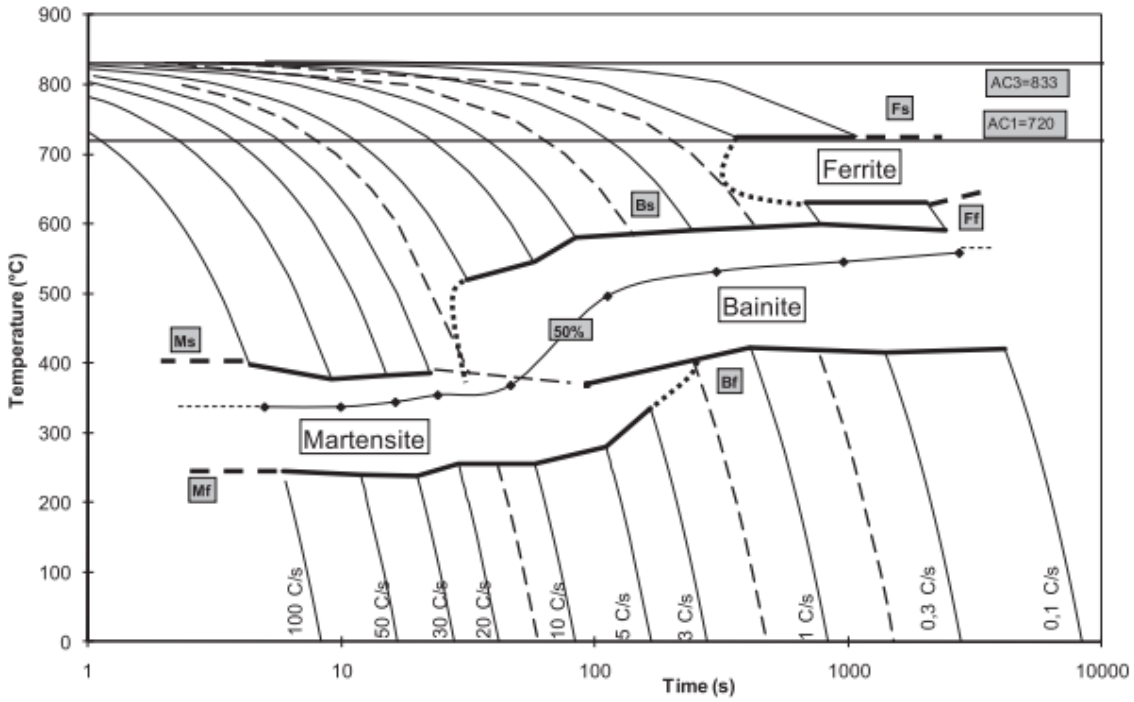

Figure 2-4 CCT diagram of SA508 G3 (austenitisation 1100 °C, ½ h). The dotted lines represent the critical cooling rates of the different phases [22].

The mechanism of solid-state steel phase formation sits in two broad categories 1. Diffusion controlled (reconstructive) and 2. Diffusionless (displacive). For a diffusion-controlled process, nucleation and growth of the new phases takes place via diffusion assisted atomic motion, thus it is very sensitive to cooling rate. Ferrite and pearlite are formed through this mechanism. For a displacive controlled process, transformation is by shear of atoms by less than one atomic displacement and the movement of all the participating atoms is coordinated, creating a new crystal structure without any diffusion. Martensite is the classic example of the phase formed by this mechanism [26]. Detailed descriptions of the key phases of steel are presented below.

2.4.1 Ferrite

Austenite decomposition on cooling occurs at the eutectoid region of the Fe-C phase resulting in the formation of ferrite and a carbon rich phase, cementite. Different types of proeutectoid ferrite morphology precipitates on austenite grain boundaries as the temperature is lowered Figure 2-5. They are typically classified by their different shapes as side plates, saw teeth and allotriomorph. Allotriomorph ferrite nucleates preferentially at the austenite grain boundaries and then starts to grow along the grain boundary. They are usually equiaxed or lenticular in shape [26].

Ferrite also can precipitate in a morphology known Widmanstatten plates, which are in the form of needles or plates. They also nucleate on the austenite grain boundaries but grow in preferred orientation on well-defined crystallographic planes. The plates nucleate either on the pre-existing allotriomorph ferrite or directly on austenite grain boundaries.

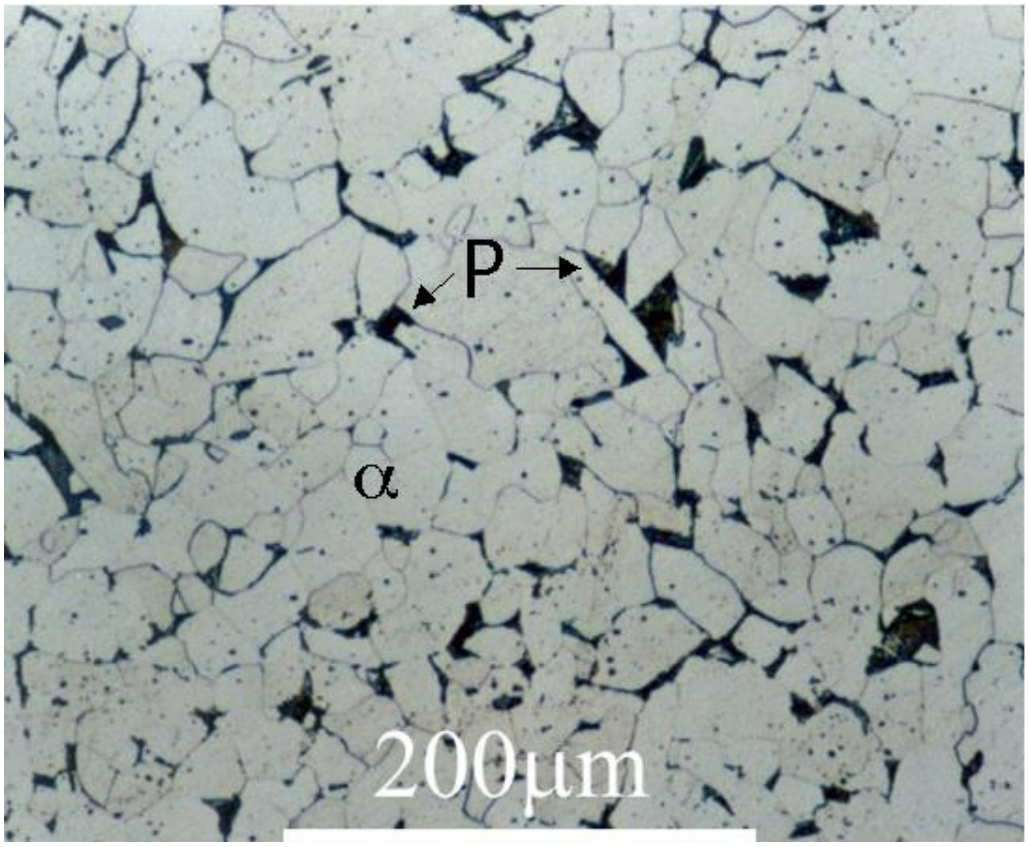

Figure 2-5 SEM micrograph of ferrite (α), and perlite (P)[26].

2.4.2 Bainite

Bainite, originally identified by Davenport and Bain in the 1920s [26], [27], [28]**,** is a non-lamellar aggregate of ferrite and carbides produced due to austenite decomposition at a temperature higher than the Martensite start temperature and below that of fine pearlite formation. In general, bainite is formed at relatively high cooling rates.

The formation of bainite is a complex phenomenon in comparison to the other microstructures formed during decomposition of austenite. The main structure of bainite is clusters of platelets or laths of ferrite, which are differentiated by particles of metal carbides or cementite. The ferrites plates are very fine making them difficult to be detected with an optical microscope. Bainite also has a variation of morphologies that typically form at different starting temperatures, as an example granular, upper and lower bainite are shown in Figure 2-6. There

has also been much debate about the mechanisms of transformation of austenite to bainite, [29]–[33]. Bainite formation exists when plates of laths of bainite nucleate by the same mechanism of martensite, however at a relatively high transformation temperature. In addition, bainite occurs when austenite is weak and cannot elastically support large deformations. Bainite sheaves grow to a limited size as a result of incomplete transformation that limits their size and become smaller with decreasing PAGS [32].

Upper and lower bainite are the most prevalent types of bainite morphologies described in the literature. Aggregates of plates (sheaves) of ferrite are the main feature of both upper and lower bainite, Figure 2-6 [29]. In general, upper bainite starts to form at high temperatures between (550-530) ºC, while lower bainite nucleates at low temperatures around (350-250) ºC. In upper bainite, austenite decomposes through a shear transformation to form plates or laths of ferrite that nucleate side by side to form similarly orientated packets. At these temperatures the carbon is mobile enough for it to diffuse rapidly in the austenite in front of the growing ferrite interface, meaning at end of transformation there are carbon rich regions between the laths that eventually transform to carbides. For the lower bainite, the temperature is too low for carbon diffusion meaning that the ferrite laths become saturated in carbon. This results in carbides precipitating inside the laths with identical orientation, typically 55 º, within the ferrite laths [34].

2.4.2.1 Granular Bainite

Granular bainite is another form of bainitic morphology that is usually seen in low carbon or medium alloys steel containing Mn or Mo. The main morphology of granular bainite is non-acicular Figure 2-7. It consists of a matrix of ferrite with a second phase that are islands of martensite and retained austenite (MA) [30]. Granular bainite nucleates in continuously cooled steel at rates of 3-50 ºC/min and starts to nucleate at higher temperatures than upper bainite [30], [35]. It has an appearance of blocks of ferrite and MA when viewed in the optical microstructure, thus the term granular bainite.

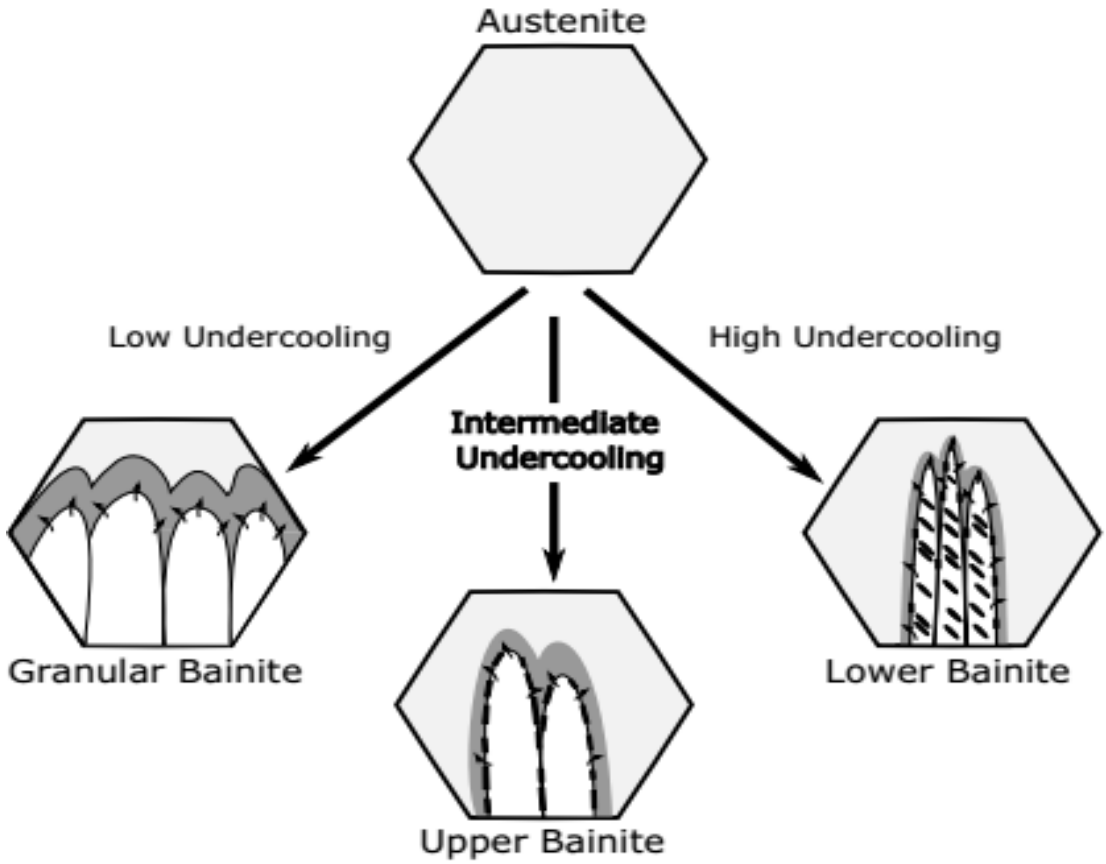

Figure 2-6 The process of the bainite transformation in steel [29].

At slow cooling rates there is rapid diffusion of carbon away from the ferrite/austenite interface inhibiting the precipitation of carbides [30], [36]. This carbon plus other austenite stabilising elements leads to the stabilisation of the austenite, leading to a microstructure consisting of granular ferrite surrounding stabilised islands of, austenite. On further cooling to room temperature some of the austenite may transform to martensite producing a microstructure of granular bainite containing islands of blocky MA islands. The MA shape is affected by the surrounding bainitic ferrite structure [37].

As a general rule, steel mechanical behaviour is degraded as a result of granular bainite formation in comparison to upper and lower bainite. The hardness between MA and surrounding bainitic ferrite is high, so cracks start easily at the MA and bainitic ferrite interface leading to poor strength and toughness [38]. Consequently, a tempering stage is highly valuable to modify these poor mechanical properties from the as-quenched granular bainite microstructure [35], [36].

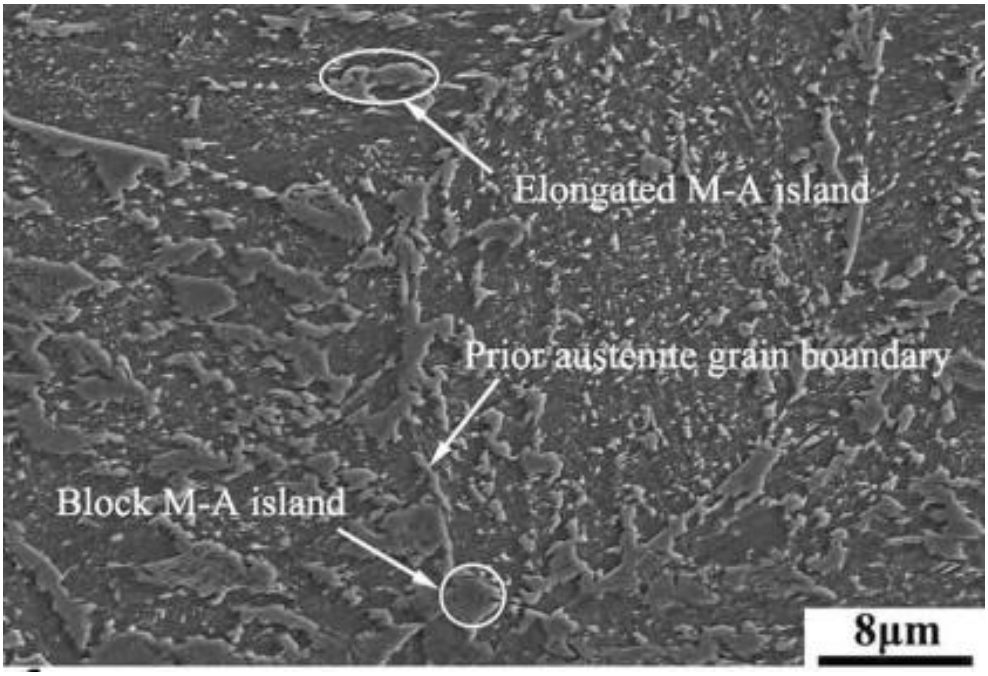

Figure 2-7 SEM micrograph represent the granular bainite with MA island [39].

2.4.3 Martensite

Martensite is a metastable body centred tetragonal phase that has a plate or acicular morphology formed in fast cooled steels through a shear mechanism. Owing to the high cooling rate, martensite is composed of a supersaturated solid solution of carbon in iron. The martensitic transformation is characterized as a diffusionless transformation in which the parent and the product phase have identical chemical compositions [40]. This leads to a large number of dislocations and an increase in strength of the steel but a significant reduction toughness. Martensite start temperature (Ms) can vary due to the level of stabilizing alloys element in the steel, with increasing carbon or austenite stabilizing alloy elements content lowering the Ms. The martensite transformation is athermal, i.e., for the transformation to continue there must be a reduction temperature, with full transformation occurring at the martensite finish temperature (Mf) [40].

Plates or laths are the main microstructure morphologies of the martensite phase. Martensite plates start to form when carbon content is more than 0.2 wt%. Most of the martensite in low carbon steel is lath martensite. Colour etching techniques help to distinguish between martensite and bainite, but it is also useful to use a hardness test to distinguish martensite from bainite, owing to martensite having a much higher hardness. At higher magnifications, such as those used in transmission electron microscopy, martensite has a much finer dislocation sub-

structure, lath substructure and higher dislocation density, making it much easier to distinguish from bainite [29], [41].

An enormous number of studies on the martensite phase have been undertaken, primarily to investigate its morphology and crystallography, however much less research has been undertaken about carbide characteristics in comparison to the detailed work in bainite, at least over the last 20 years [42]. Lower bainite morphology and tempered martensite morphology are generally considered similar. Some research, however, distinguishes between them with wavy lath boundaries and ledge-like protrusions for the martensite [43].

2.5 Effect of Alloying Elements on HSLA

The addition of alloying elements to steel generally tends to either broaden the austenite field, promoting high austenite stability over a range of compositions, or diminish the austenite field, maintaining the formation of ferrite over a range of composition. This section will go over some of the key elements present in steel and their effect on austenite and ferrite stability and their impact on non-equilibrium transformation behaviour [44]–[49].

2.5.1 Molybdenum (Mo)

Molybdenum (Mo) has a bcc crystal structure and works as ferrite stabiliser, is a strong carbide former, and small additions significantly increase hardenability. Additions as small as 0.05 to 0.25 wt % in combination with manganese and nickel can suppress the formation of pearlite, moving the pearlite nose in the CCT diagram to over 10000 seconds, therefore promoting the formation of bainite [50], [51]. The bainite start temperature is also suppressed leading to more refined bainite sheaves, with fine Mo_2C carbides, which significantly enhances strength. The promotion of Mo_2C carbides at the expense of cementite also significantly improves toughness, including a reduction in the ductile to brittle transition temperature.

2.5.2 Nickel (Ni)

Nickel is a large austenite stabiliser, significantly opening the range of the austenite phase field [6], [15], [52]. If added, in large amounts it can stabilise austenite to room temperature, e.g., austenitic stainless steels. However, in relatively small amounts (<5 wt%) its main effect is to increase hardenability, making both martensite and bainite formation easier. It also reduces the transformation temperatures promoting the formation of a finer lath structure [53].

2.5.3 Chromium (Cr)

Chromium (Cr) forms hard stable carbides and improves the steel hardenability, e.g., raising Cr percentage decreases the bainite start temperature [45]. This phenomenon provides steel with a high potential to hinder softening during tempering and improves steel properties where high wear resistance is required but makes the steel sensitive to temper embrittlement. Furthermore, because carbide formation is easy with Cr incorrect heat treatment can lead to large carbides forming leading to a detriment in properties [11].

In the case of SA508 G4N, Cr has a large influence on carbide precipitation. The main observation that has been observed is that when Cr content increases the carbide size reduces. Thus, there is a reduction on the number of carbides with the critical size of carbide that can initiate a crack, therefore increasing the toughness [52]. In addition, Cr enables the formation of a coherent oxidation layer that enhances corrosion resistance.

2.5.4 Vanadium (V)

The main effect of Vanadium (V) in high strength steels is to inhibit grain growth during austenitisation. Also, carbide size tends to decrease as the amount of V increases, increasing elongation to failure, ultimate tensile strength increases, and DBTT. It has, however, been observed the addition of V impedes the appearance the other precipitation such as M_7C_3, owing to it being a stronger carbide former [54].

2.5.5 Manganese (Mn)

Manganese (Mn) often tends to form microstructure of carbide-free bainite with a high fraction of retained austenite [55]. This is because is a strong austenite stabiliser [46]. In addition, martensite start temperature decreases as Mn volume fraction increases [56].

2.5.6 Carbon (C)

Carbon has a significant effect on iron mechanical properties even in very small additions. In austenite it forms an interstitial solid solution at high temperature but has significantly lower solid solubility at room temperature, meaning the carbon is rejected from the solution in the form of cementite or metal carbides. Carbon is essential in developing solid solution hardening, enhancing hardenability, and in controlling strength through the formation of cementite and other carbides [6]. Carbon is an austenite stabilizer, enhancing the formation of bainite and martensite, and lowering their starting temperatures [33], [57]. The mean the sizes of both

martensite and bainite packets and blocks decrease with an increase in carbon content [57]. Moreover, increasing the carbon content enhances the formation of coarse carbide, and it degrades the steel toughness [58].

2.6 Dilatometry

One of the most popular techniques used to investigate and study solid to solid phase transformations in steel is dilatometry. In this method, the linear expansion of a relatively small standard cylindrical specimen is measured as a function of temperature cycle, which is then plotted in the form of a dilatation curve [40], [59], [60]. If there are no phase transformations present within the temperature range measured, then the slope of the curve is the coefficient of thermal expansion (CTE) of the material. However, if there is a phase change process undertaken within that temperature range there will be a deviation from the CTE slope owing to the change in volume associated with the rearrangement of atoms into a different crystal [40], [59]. More importantly, when the transformation begins, the dilation curve deviates from linearity and a clear transformation start temperature can be defined, and once the transformation ends it again returns to linear behaviour, representing the transformation end temperature. because of the change of crystal structure of the transforming phase has a different specific volume, and often because of the latent heat released by the transformation affects heat transfer too. Once a transformation is completed, the dilatation returns to a linear relationship with temperature. An example of this is shown in Figure 2-8. Note, since the phases will be different prior and post transformation the CTEs will be different leading to different linear slopes as shown in Figure 2-8.

In most experimental dilatometers sample heating can be to a wide range of austenitisation temperatures and then be cooled down at a relatively wide range of cooling rates, allowing the temperatures at which transformations occur to be determined as a function of that austenitisation temperature and cooling rate. This then allows for the construction of a CCT diagram as outlined previously.

A key element in constructing an accurate CCT diagram from dilatometry data is precise identification of the transformation temperatures. As, outlined above, the transformation temperatures are defined as the beginning of the deviation from linearity of the dilatation plot. The small volumes of the transforming material, however, does not cause large deviations of linearity, making it non-trivial to accurately identify the transformation temperatures. For

example, Figure 2-9, shows the small ferrite transformation (Fs). As such, many different methods have been developed to identify the transformation temperatures from dilatometric data. The simplest method is the differentiation method.

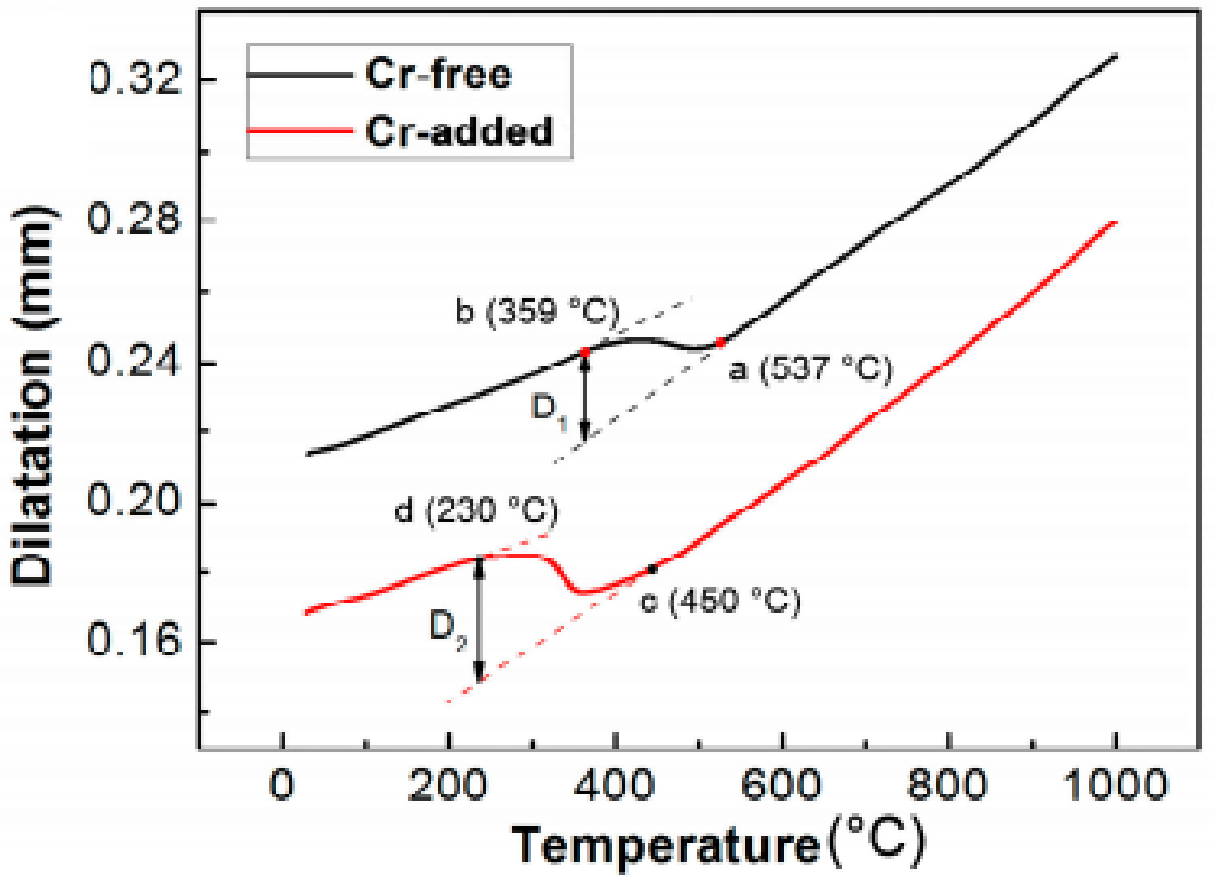

Figure 2-8 Shows the effect of Cr ally element in bainite start temperature [45].

The first step in the differentiation method is to plot the change in length (dL) normalised by the original length (Lo) as a function of temperature Equation 2-1. This is known as the true coefficient of thermal expansion (α_T) and can be described as:

$$\alpha_T = \frac{d}{dT}\left(\frac{dL}{Lo}\right)$$

Equation 2-1 [61]

The derivative of α_T with respect temperature is zero if there is no phase transformation and thus is changing during phase transformation, Equation 2-2. The transformation start and finish

temperatures are therefore defined as the deviations from zero on a plot of $d\alpha_T/dT$ against T, i.e.,

$$\frac{d\alpha_T}{dT} \neq 0; \quad when; \frac{dL}{Lo} \neq AT + B \qquad \text{Equation 2-2 [61]}$$

An example of this methodology is shown in Figure 2-9 , showing three clear deviations from linearity for ferrite (Fs), bainite (Bs), and martensite (Ms) [61].

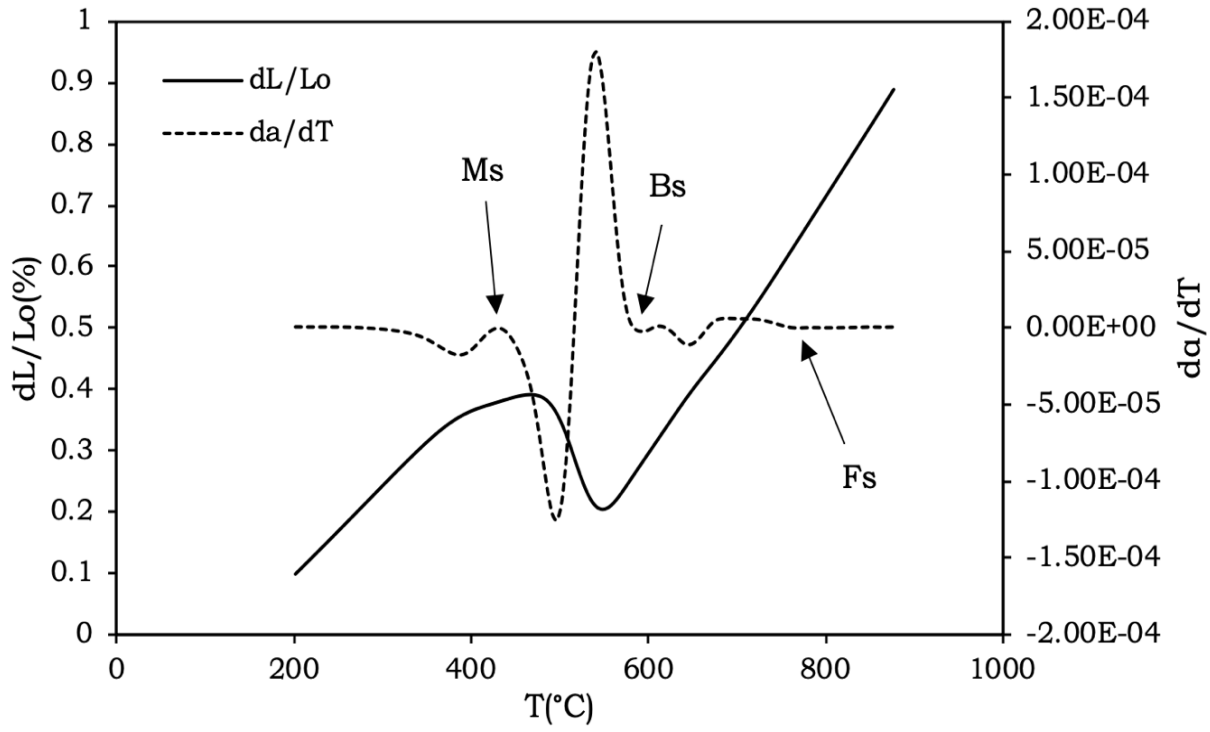

Figure 2-9 The recorded dilatation of a low alloy steel during continuous cooling at 10 °C/min, and its second derivative of dilatation with respect to temperature [61].

2.7 RPV of SA508 G3 Steel

Vast amounts of steel are utilised within a nuclear power plant. However, only a relatively small portion is employed for very heavy section forgings and plates. SA508 Grade No. 3 (SA508 G3) has been used in civil nuclear plants RPVs for more than 40 years because it has a good combination of weldability, toughness and strength [6], [8]. However, with the possibility of increasing wall thickness in next generation civil nuclear reactors there is a concern that we are reaching the limits of SA508 G3's hardenability, i.e., the cooling rates in

the middle of the wall may be slow enough to initiate the formation of ferrite, thus decreasing toughness [22], [58].

The new generation SA508 alloy, SA508 4N, has been developed to increase hardenability by adding 2 wt% Ni [44], [62]. A detailed comparison between the two SA508 grades is given below.

2.7.1 Comparison Between the SA508 Grade 3 and SA508 Grade 4N

The differences in chemical composition specification between the SA508 G3 and SA508 G4N are shown in Table 2-1. SA508 G4N has a higher percentage of Ni and Cr compared to SA508 G3, while it has less Mn and C [6], [11], [13]. Figure 2-10 shows the tensile strength, yield strength and elongation to failure of SA508 G4N and G3 Cl.1 and Cl.2 [6]. SA508 G4N has a higher yield strength and a higher ultimate tensile strength than G3 [6], [13]. There are also reports that the impact toughness and fracture toughness is superior in the new material. However, it is difficult to find distinct differences in the J-resistance (J-R) curves in the reported literature, whilst the fatigue crack growth rates are almost the same for both materials [6].

Both SA508 G4N and SA508 G3 steels have complex microstructures, so it is more practical to use SEM imaging instead of the optical microscopy for detailed analysis of microstructure [27], [34]. In the literature, a regular tempered upper bainite structure that contains a lath structure within the prior austenite grain is the predominant microstructure in G3, while G4N is dominated by a microstructure of tempered martensite and lower bainite, Figure 2-11 [63]. SA508 G4N typically has a finer austenite grain size compared to SA508 G3 for equivalent processing conditions [44]. Cr-rich carbides form most of the precipitates in SA508 G4N, whilst G3 has long rod-type cementite at the bainitic ferrite lath boundaries and cementite and M_2C inside the laths [6], [39], [64].

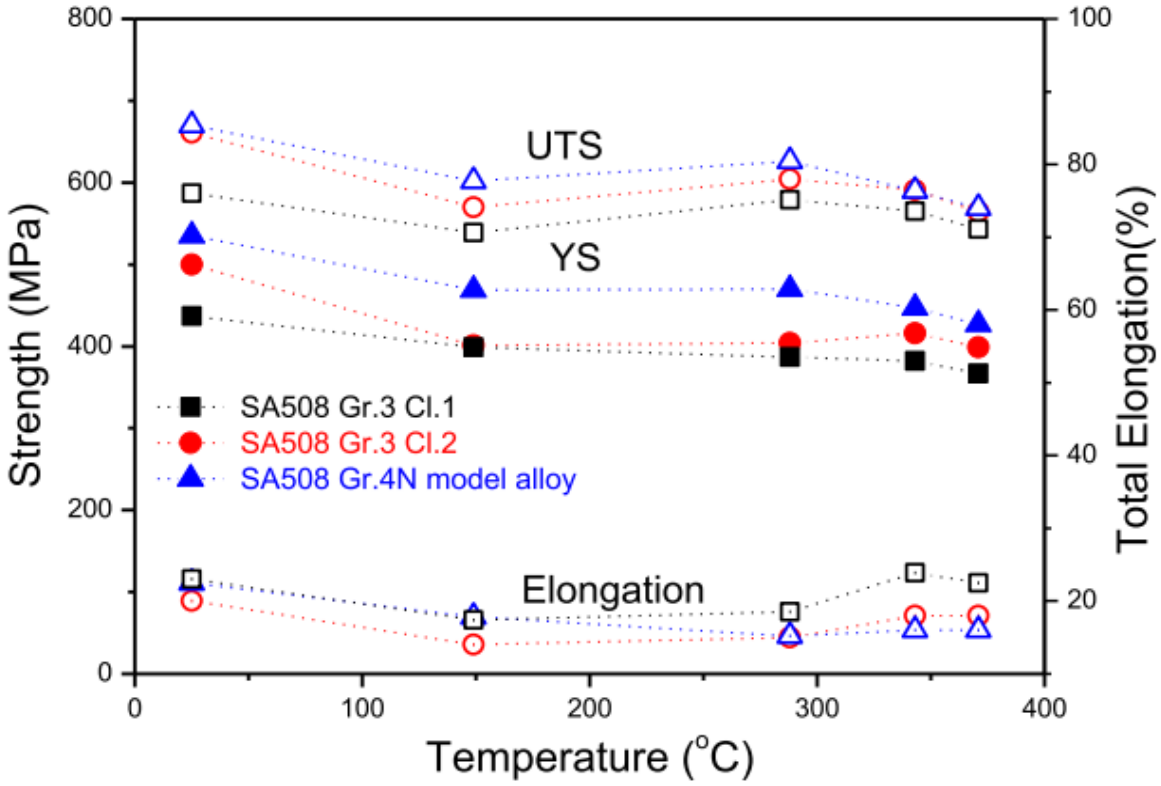

Figure 2-10 Tensile and yield strength and elongation of SA508 G4N and G3 Cl.1 and Cl.2 [6].

2.7.2 The Features of SA508 G4N

Based on the microstructure analysis presented in the literature, two different microstructures are generally observed in as-quenched and tempered SA508 G4N, bainite and martensite. The martensite packets contain a fine lath structure and the bainite packet have internal precipitates, Figure 2-11. The precipitates are Cr-rich carbides ($M_{23}C_6$ and M_7C_3), the volume of which increase linearly with increasing Cr content. However, not all carbides contain just Cr with the M referring to Cr, Mo, V, Mn, and Si [65]. During tempering the composition of the carbides remains relatively stable [39].

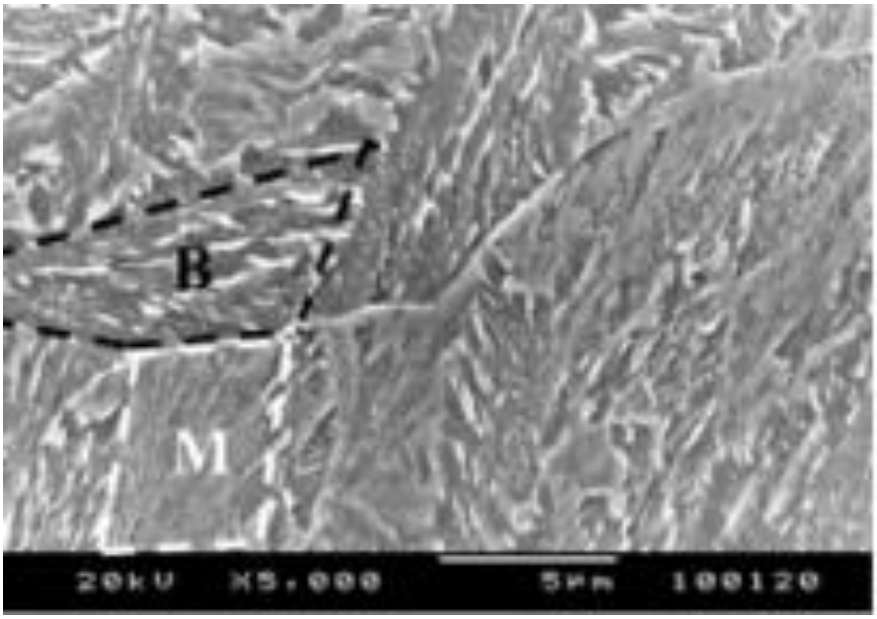

Figure 2-11 Microstructure of SA508 G4N as-quenched SEM, B is bainite, M is martensite [15].

2.7.3 Temper and Irradiation Embrittlement of SA508 G4N

Temper embrittlement, i.e., decrease in toughness when the steel is cooled slowly through the temperature range of 600°C to 400°C, is one of the major issues that can affect the quality of steel and its mechanical proprieties [11], [44], [51]. Moreover, the RPV can be affected by temper embrittlement due to its high running temperature. This results in a segregation of impurities such as P, Sn, As, and Sb to the grain boundaries. The chemistry of SA508 G4N steels can also enhance temper embrittlement; for instance, excessive phosphorus (P), Chromium (Cr) and Manganese (Mn) through the precipitation of intermetallics at grain boundaries. The reduction of temper embrittlement resistance, results from increasing the Transition Temperature Shift (TTS) via reducing the C activity. Figure 2-12 shows the effect of Mn content on the Charpy impact energy transition, with increasing Mn content leading to a decrease in the Charpy impact energy transition [11]. So, it is essential to consider how thermal embrittlement can be impeded in order to decrease the possibility of toughness reduction in the RPV, before employing it in the nuclear industry [11], [44], [64].

There have been a number of studies conducted into the embrittlement of SA508 G4N. For instance, 3.5NiCrMoV low alloy steels have a similar chemistry with the SA508 G4N [11]. Under different operating conditions, internal pressure can build up and exert thermal stresses on the vessels, so it becomes a source of a crack initiation in the wall and may aid crack propagation causing failures to occur. Suzuki et al. stated Cr and Mn co-segregate but there is

not any noticeable change in toughness, but Park [11] suggests a slight co-segregation effect [8], [11], [66].

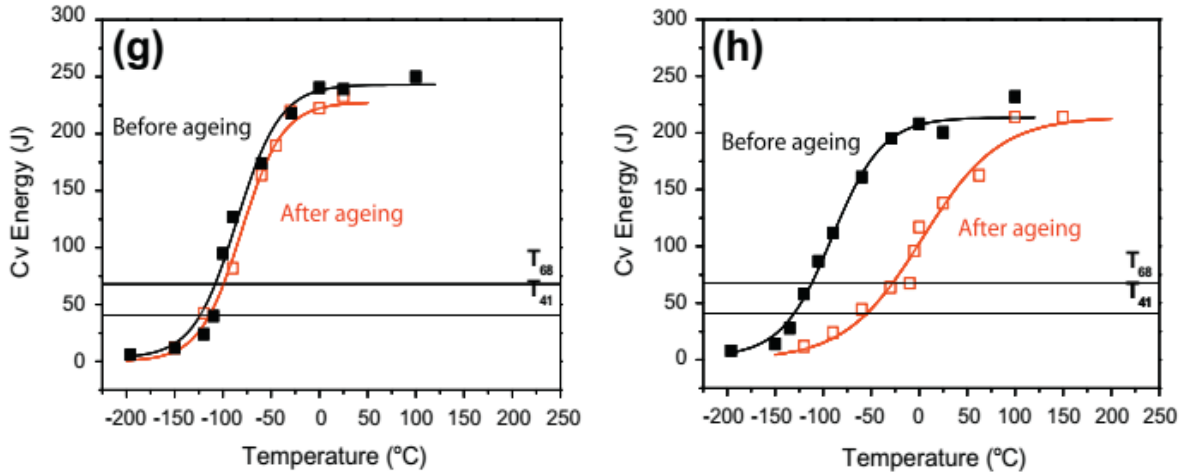

Figure 2-12 Charpy impact energy transition curves of SA508 G4N with variation of Mn content (g) lower Mn, (h) higher Mn [11].

2.7.4 Post Welding Heat Treatment at SA508 G4N

Post Welding Heat Treatment (PWHT) is an essential processing stage to recover the properties of the steel and/or reduce residual stress after welding. In the case of SA508 G3, it is generally tempered at 660 °C but the PWHT is at 610 °C, however for the case of SA508 G4N there are currently no clear temperature definitions for these processes yet [64].

Lee et al. [64] investigated the tempering of SA508 G4N. Figure 2-13 shows tensile strength, yield strength and elongation of SA508 G4N after tempering at 630 °C and 660 °C. As expected, the higher tempering temperature reduces strength but increases ductility. Based on the tensile test, the yield strength and ultimate strength are 630 MPa and 754 MPa when the materials are tempered at 630 °C, respectively. During PWHT, the steel becomes softer in case of tempering at 630 °C as a result of releasing internal stress or reduction in the dislocation density. The elongation values increase around 1.2% after PWHT when it tempered at 660 °C [64].

As-tempered at 630 °C, reference temperature (T_0) declines, as a result of a low amount of coarse carbides over 0.2 µm in size, by contrast T_0 increased when the samples were introduced to PWHT due to increasing the amount of coarse carbides. Figure 2-14 represents the carbide size corresponding to rank percentage arranged by order of size, PWHT coarsen the carbide

size. However, the impact toughness improved due to matrix softening when it only at as-tempered at 660 °C [64].

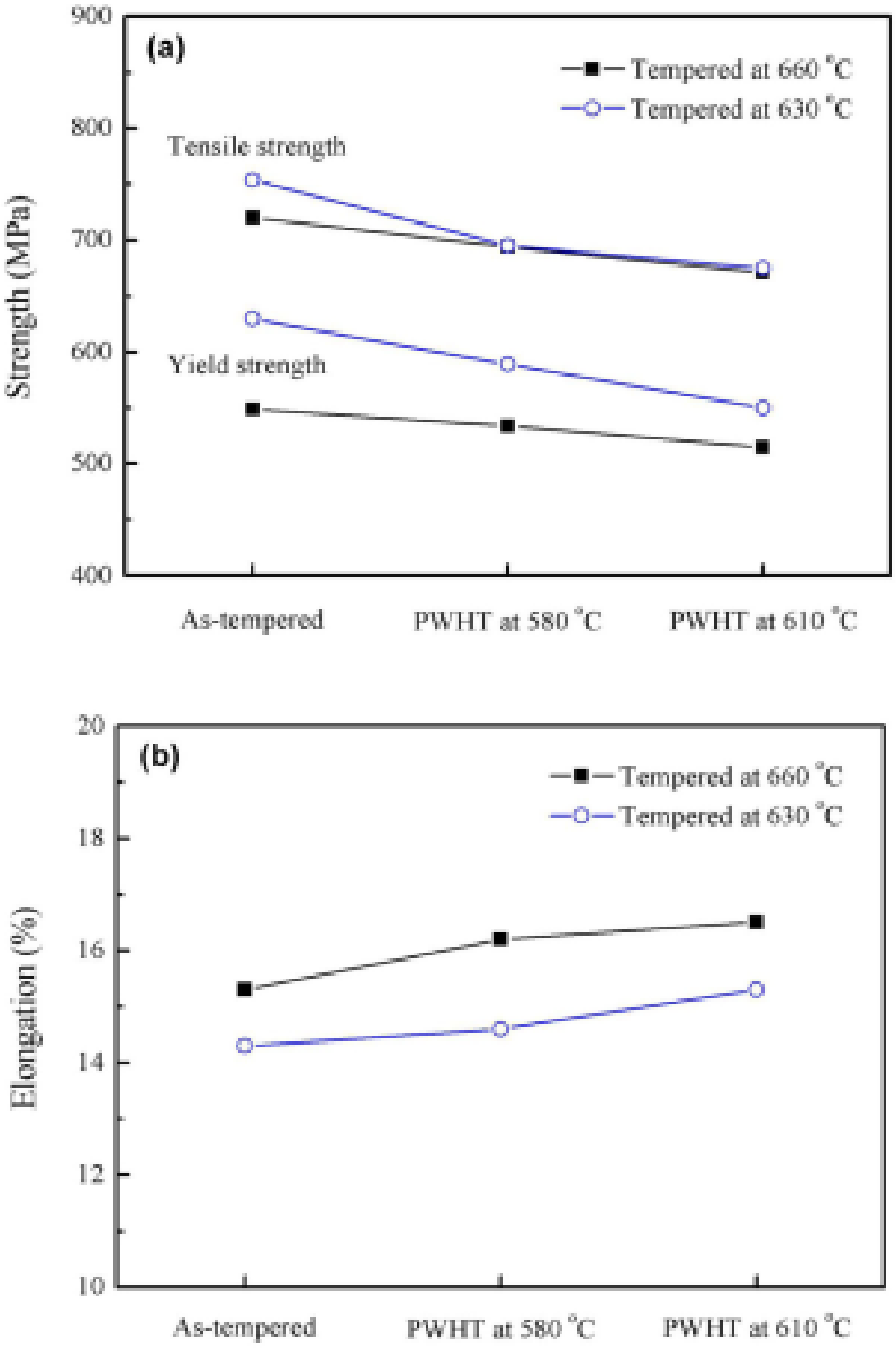

Figure 2-13 Tensile strength, and elongation of SA508 G4N with tempered at 630 °C and 660 °C [64].

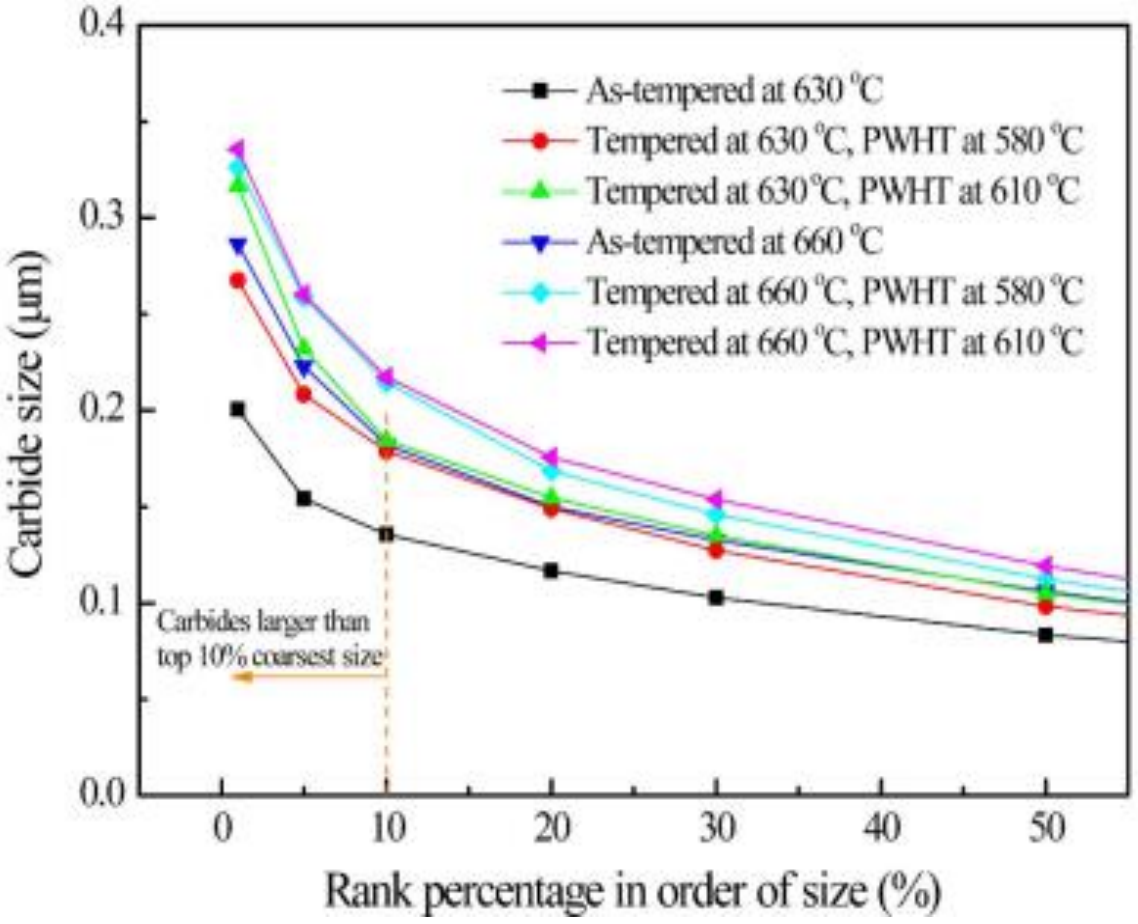

Figure 2-14 Carbide size corresponding to rank percentage arranged by order of size [64].

2.8 Heat Treatment of RPV Future Material

The manufacture of an RPV consists of a number of stages: casting, forging, heat treatment and machining. In this work, we are focused on the quality heat treatment. The quality heat treatment occurs at the point where the forging is at a near-near shape to the final component. This is the final stage of microstructure control and thus key to mechanical properties and performance in service. It typical involves three main stages: austenitisation, quenching, and tempering. A detailed description of quality heat treatment is presented below.

2.8.1 Quality Heat Treatment

2.8.2 Austenitisation

Austenitisation is a procedure of heat and hold the forging to a high enough temperature at sufficient time to convert all the material to austenite and to dissolve carbides back into solution.

Raising austenitisation temperature also leads to an increase in the coefficient of diffusion. As an example, when the austenitisation temperature increases from 1100 ºC to 1180 ºC the diffusion coefficient of carbon in austenite is doubled. Increasing the heating rate and temperature can increase the homogenisation process, but this may cause distortion or cracking. Increasing austenitisation or time temperature also leads to increased austenite grain size, owing to the driving force to reduce the total energy of the system through the reduction in grain boundary area. To avoid significant grain growth, alloying elements are added that form stable nitrides or carbon-nitrides at the austenitisation temperature, which pin the austenite grains from growing. Examples of these nitrides are AlN [67], CrN [28], $MnSiN_2$and VN [26], however, there is a lack of literature on what nitrides are used to control grain growth in SA508 G4N.

2.8.3 Quenching

The quenching stage is the essential technological process employed to optimize the large PRV microstructure in order to achieve the desired final physical properties. Quenching is applied to a forged component after austenitisation and generally this is through immersion in a water tank, which may be stagnate or have some level of flow. Owing to the complexity of the water/hot steel interface the level of heat transferred from the steel to the water is temperature dependent. For example, at high temperatures there is a vapour layer generated which inhibits significant heat transfer. It is only when the temperature drops to a condition where bubbles can nucleate is there significant heat transfer. This, when combined with the fact that when we have thick sections the rate of heat transfer is significantly influenced by thermal conductivity of the material, i.e., it doesn't matter how fast the heat is extracted at the surface near the centre, there may be a slow cooling rate regardless. This means that the cooling rate throughout the thickness is highly non-linear and non-constant [29], [68], [69]

2.8.4 Tempering

Tempering is an important process in RPV fabrication as it rebalances strength and toughness to acceptable levels by reducing residual stress, reducing dislocation density, and precipitating out carbides following quenching. In a conventional sense the quenching stage provides a totally martensitic microstructure, which has high strength and low toughness. Carbon segregation, precipitation of transition carbides, retained austenite decomposition, carbide precipitation and carbide coarsening are the main microstructural changes that take place

during the tempering process [70], [71]. Tempering is a diffusion-controlled, in which tempering temperature, tempering time and the chemical composition of steel are essential parameters to control the degree of tempering, and thus direct impact on the carbides size, carbide precipitation and carbide growth [72], [73]. However, carbides suppress the dislocation movement, so the dislocation demands more energy to pass through fine carbide due to long pass paths [64]. Steel becomes brittle due to the quenching stage which leads to martensite microstructure and supersaturated carbon. In general, SA508 G4N has a mixed structure of martensite and bainite. On the other hand, the RPV has a thickness around 200-300 mm, so it is difficult to monitor the internal heating and cooling stages [39]. Generally, Cr-type carbides, $M_{23}C_6$ and M_7C_3 are the main precipitates in SA508 G4N. At the lower tempering temperature, the microstructure is non-uniform because of under-tempered region compared to uniform and well-mixed microstructure [64].

2.8.5 Effect of Tempering in Martensite Microstructure

In the first stage of tempering, carbon segregates and redistributes to dislocations, defects, PAGBs and lath boundaries to form carbon clusters from the solid solution, which eventually precipitate out as carbides [70], [72]. Alloying elements play a crucial role in restricting carbide growth and coarsening due to thermodynamically stabilising effect the carbide.

2.8.6 Effect of Tempering on Bainite and Granular Bainite

In general, the bainite start temperature is higher than martensite. In the as-quenched condition bainite looks like tempered martensite, consisting of a lath-like ferrite phase and carbides within and between the laths. So, the tempering treatment either has the effect of either dissolving pre-existing carbides or coarsening them, depending on their thermodynamic stability [74]. During the tempering stage, bainite lath size increases, consuming neighbouring laths, and their boundaries begin to bulge and curve out. There is also significant recovery and reduction of dislocation density, with dislocation cells clearly obvious within the laths but there is no evidence of recrystallization [75].

During tempering, Granular bainite decomposes to many different phases depending on the tempering parameters, such as tempering temperature and time and alloying elements present. Granular pearlite, ferrite, bainite, martensite and carbide are phases reported after tempering of granular bainite [76]. Li [75] stated that the higher mobility of granular bainite

during tempering meant it consumed any lath bainite present, suggesting that when the temping time was more than 240 min all lath bainite was consumed by the granular bainite [75].

2.9 Prior Austenite Grain Size (PAGS)

As discussed previously, PAGS is a function of the austenitisation temperature and holding time and the chemical composition and its distribution. Mostly, alloying elements decrease the grain growth by promoting solute drag of the boundaries and/or pinning grain boundaries through nitride or carbo-nitride particles [16]**,** [77].

2.9.1 Models of Predicting PAGS

Many empirical and semi-empirical equations have been developed to predict austenite grain size after austenitisation in HSLA steel. Some models take into account alloying elements, while others only consider the temperature and time of austenitisation. Thermodynamic factors such as grain boundary energy, activation energy for grain boundary diffusion are rarely considered. Moreover, some models have been developed for specific types of steel and have no transferability to other types of steel. The typical expression between austenite grain size and austenitizing conditions is as follows [67]:

$$D^n - D_0^n = A\, exp(\frac{-Q}{RT})t^n \qquad \text{Equation 2-3 [10], [34], [67]}$$

D_0 and D are the initial and final grain sizes (μm) respectively,

t = austenitisation time (s),

T = austenitisation temperature (K), n the time exponent,

Q = the activation energy (J/mol) for boundary motion,

R = the universal gas constant (8.314 J/mol/K) and

A = the materials constant

Where D_0 and D are the initial and final grain sizes, respectively, t is the austenitisation, T the austenitisation temperature, n the grain growth exponent, Q is the activation energy (J/mol) for boundary mobility, R is the universal gas constant (8.314 J/mol/K) and A is a materials

constant [67]. Most of the austenite grain size models have their basis in Equation 2-3. Some values for different steels for *n*, *Q*, and *A* are shown in

Table *2-3*.

Table 2-3 Outlines of experimental method that predict the austenite grain growth, x_i is the concentration in wt.% of alloying elements [67].

Steel type	Model	*n*	*A*	Q / kJ mol^{-1}
Rolling C–Mn	$D^n - D_0^n = A \exp\left(\frac{-Q}{RT}\right)t$	10	3.87×10^{32}	400.0 for $T > 1000$ °C
Rolling C–Mn	"	10	5.02×10^{53}	914.0 for $T < 1000$ °C
Forged Waspaloy disc	"	3	2×10^{26}	595.0
C–Mn	"	7	1.45×10^{27}	400.0
C–Mn–V	"	10	2.60×10^{28}	437.0
C–Mn–Ti	"	4.5	4.10×10^{23}	435.0
Micro-alloyed	"	5	1.60×10^{32}	716.9
Medium C–Nb	"	2.5	1.03×10^{16}	397.7
C–Mn	"	4.1	1.72×10^{21}	$352.2 + 21.8x_C + 19.9x_{Mn} + 7.2x_{Cr} + 7.4x_{Ni}$
Low C–Mn	"	2	4.27×10^{12}	278.8
Low alloy	$D = A \exp\left(\frac{-Q}{RT}\right)t^n$	0.211	76.71×10^3	$89.1 + 3.6x_C + 1.2x_{Ni} + 1.4x_{Cr} + 4.0x_{Mo}$
Ultrahigh-strength 300 M	"	0.17	4.04×10^6	132.0

In the vast majority of cases, the grain size increases with increasing the austenitisation temperature or holding time [11], [67]. At first glance, PAGS has less effect on bainite formation in comparison to pearlite and ferrite. In the case of SA508 steels, the hardenability of steel is highly affected by PAGS, however most of equations for predicting PAGS in low alloy steels compositions are them not applicable for SA508 steels Equation 2-4, 2-5, 2-6, and 2-7 [67]. The main reason is that the alloying elements, such as (Ni, Cr and Mo), act as a solute dragging factor for the austenite grain boundaries [34].

$$d = 1.324 * 10^5 \, exp(\frac{-94000}{RT}) t^{0.194}$$ Equation 2-4 [34]

$$d = 9.1 * 10^6 \, exp(\frac{-126000}{RT}) t^{0.18}$$ Equation 2-5 [34]

$$d = 7.9 * 10^{54}\ exp(\frac{-69000}{RT})t^{0.19},$$ Equation 2-6 [34]

$$d = 4.1 * 10^{7}\ exp(\frac{-141000}{RT})t^{0.12},$$ Equation 2-7 [34]

Pous-Romero [67] argues that D_0 in SA508 G3 is very small by comparison to D in most industrial settings, so it is negligible and can be ignored. He developed an equation taking into consideration the effect of the alloying elements on the activation energy for grain growth and steel chemical composition in the form:

$$D = A\ exp(\frac{-Q}{RT})t^{n}$$ Equation 2-8 [63], [67]

A=76671, Q=89098+3581 x_c+1211x_{Ni}+1443x_{Cr}+4031x_{Mo} Equation 2-9 [67]

Where x_i is the weight percent of the key alloying elements.

Xikou [63] studied and measured PAGS in SA508 G4N and developed Equation 2-10 to describe austenite growth using material heated between 1150 to 1250 °C for different holding times between 0.5 to 4 hours to obtain PAGS between 51 to 135 µm, Figure 2-15 [63] . This model shows an agreement between the model and experimental results for SA508 G4N. On the other hand, this model does not apply for other steels such as SA508 G3. In addition, alloying elements were not considered in this model.

$$d = 1.034 * 10^{3}\ (texp(\frac{-211177}{RT}))^{0.298},$$ Equation 2-10 [63]

Dong al et. [10] studying SA508 G3 steel argued that there is a different growth rate as a result of diverges at different austenitisation temperatures, so he developed two different

equations for various temperatures for instance between 900 to 1050 °C, Equation 2-11 and between 1050 to 1250 °C, Equation 2-12. The requirement for the two equations is a result of that fact that at higher temperatures the second phase nitrides partially dissolve, reducing their pinning impact, leading to much faster grain growth. A comparison between the mathematical models and experimental grain size measurement and the mathematical models for SA508 G3 at holding time of 30 min and holding time of 300 min is shown in Figure 2-16 [10].

T (900-1050) °C $d_t^{2.016} = d_0^{2.016} + 1.733 * 10^7 \, t^{0.691} exp(\frac{-121556}{RT})$, Equation 2-11 [10]

T (1050-1250) °C $d_t^{1.504} = d_0^{1.504} + 1.733 * 10^{10} \, t^{0.982} exp(\frac{-230986}{RT})$, Equation 2-12 [10]

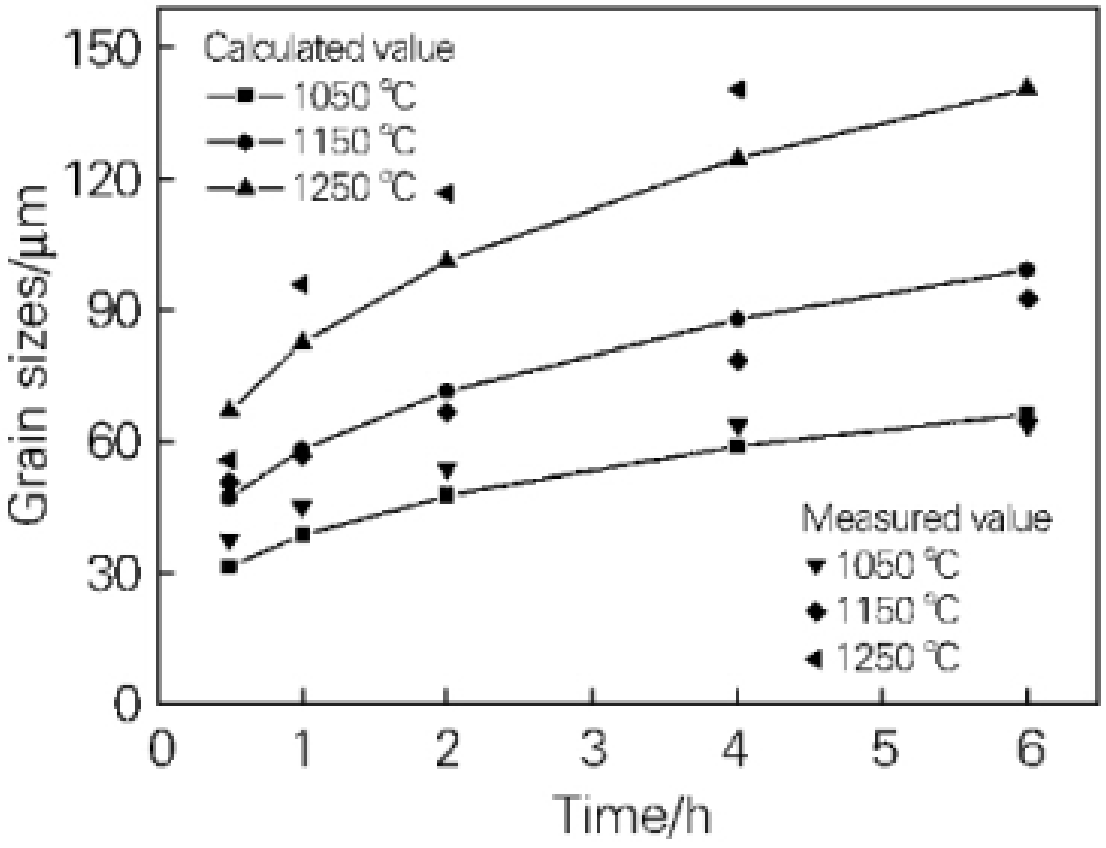

Figure 2-15 Grain size measurement and Comparison between mathematical models and empirical SA508 G4N [63].

2.9.2 Experiential Measurement of Grain Size

There are many different standard ways for measuring PAGS. For instance, ASTM E112 and DIN EN ISO 643, although several factors can make the measurement of grain size problematic, particularly the fact that grains are three dimensional, but we measure on a two-dimensional plane. The size of grains is also not uniform but most of the time the mean value of the grain size is used to define the grain size [78].

In this study the linear intercept method is the technique used to quantify PAGS using the guidelines of ASTM E122-13, Figure 2-17. ASTM E122-13 measures grains by counting the number of grain boundaries that are intercepted on a number of test lines (green or red but not both) drawn on the micrograph. The grain size is then calculated by dividing the total length of the lines by the number of intercepts. A minimum of 4 independent lines (i.e., lines that do not cover the same grains) is recommended [78].

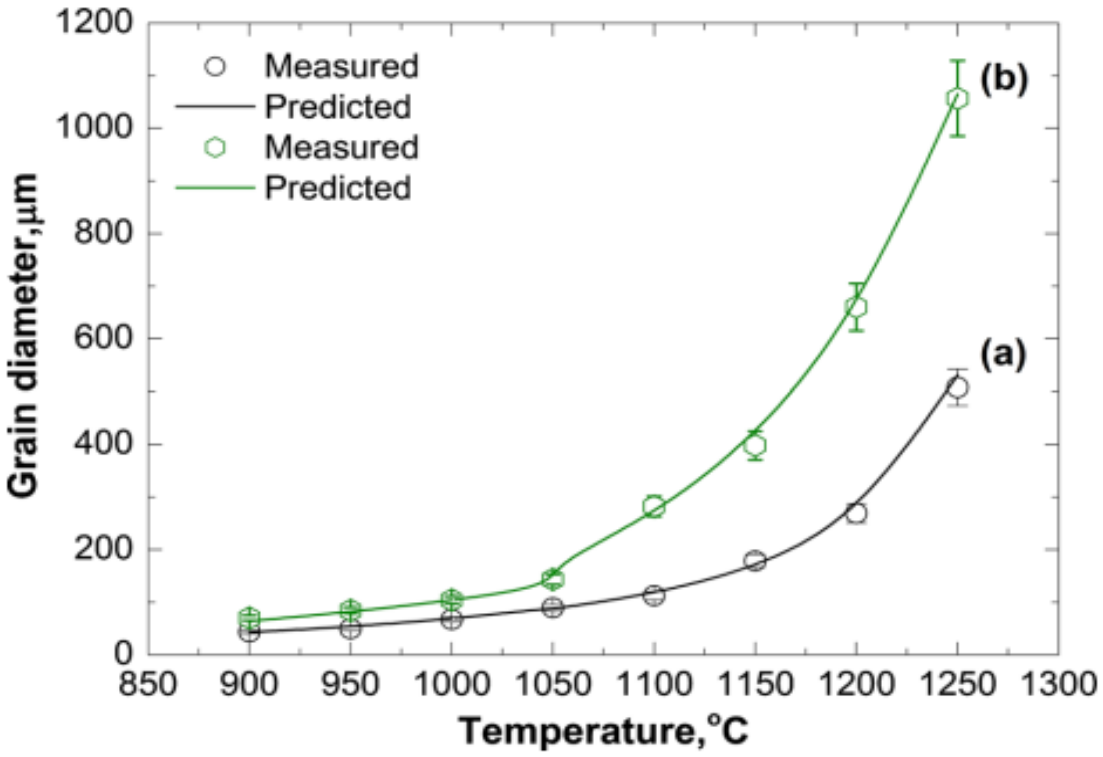

Figure 2-16 Grin size measurement and Comparison between mathematical models and empirical SA508 G3: (a) holding time (30 min), (b) holding time (300 min) [10].

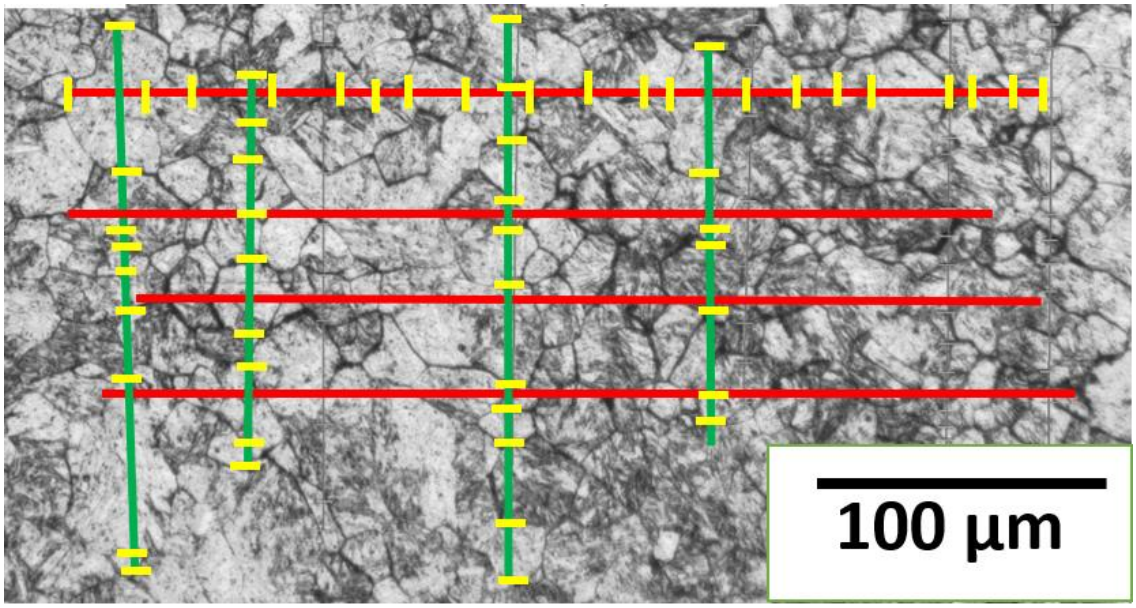

Figure 2-17 Shows a replicated material microstructure, where the(black lines) represent grain boundaries, (green lines) represent vertical line, (red lines) represent horizontal line and (yellow) shows the intercept between the test line and grain boundaries.

It is not easy to measure PAGS, as technically there is no austenite and we have to reveal some chemical aspect that they left behind during the transformation to the low temperature phases. Historically, to reveal prior austenite boundaries the material would have a low temperature treatment to allow elements such as P and S to form clusters in the prior austenite boundaries. This enhanced level of P and S would then be revealed on etching. However, with the improved chemistry control in steelmaking there is very little P and S in modern steels. This has led to numerous etchant methods being developed and presented to reveal the grain boundaries as a result of different chemical composition [78]. Most literature uses a combination of hydrochloric acid (HCL) and aqueous picric acid heated to about 80 °C or 90 °C. In some instances, a wetting agent is also added to improve cohesion with the etchant [78]. The mechanism of etching is suggested to be chemical attack of tramp elements Nb, P, Sn and As that segregate to PAGBs.

2.10 The Transformation of Prior Austenite Grain Size (PAGS) to Bainite

The transformation of austenite to bainite is very complicated and is the least understood of microstructures observed in HSLA steels [34], [79], [80]. Moreover, there is still much debate in the literature about the effect of PAGS on the bainitic transformation [27]. A number of researchers believe that a fine austenite grain size leads to faster growth of bainite, while others believe a small grain size reduces the likelihood of the transformation actually occurring, whilst

others cannot notice any change on the bainite transformation when PAGS decreases [34], [79], [80].

Braford et al. [81] studied the composition of the alloys Mn1011, Mn1014 and Mn1512 and stated that reducing the PAGS can speed up the transformation owing to bainite nucleating at the grain boundaries or near boundaries, thus increasing nucleation density. The steel was highly pure with a small quantity of manganese added. Increasing the temperatures between 1000-1250 ºC for 5 minutes by passage of a direct current in order to provide different grain size. After that, a uniform state was provided by cooling all the specimens to 1000 ºC and holding them at this temperature. Then, the samples were cooled rapidly [81].

Seok et al. showed for Fe-0.39C-0.65Mn-0.24Si-1.60Ni-0.67Cr-0.15Mo that the formation of upper bainite increases with decreasing PAGS, but the transformation to lower bainite is not affected by PAGS [34]. The austenitisation temperatures varied from 950 to 1150 ºC with the average austenite grain size varying from 24 to 162 µm. Around 430 ºC was the inflection point between the upper and lower bainite as a result of continuous cooling at 1.6 ºC /min. The disagreement between the transformation mechanism and kinetics of upper and lower bainite is likely to create the inflection point [34].

On the other hand, Graham and Axon reported that transformation from austenite to baintite is reduced with finer PAGS as a result of reduction of bainite plate growth by the matrix [80]. The experiment was set up by changing the maximum heating temperature to change austenite grain size, then specimens were homogenised at 1200 ºC and cooled very quickly to 800 ºC. After that, they were cooled through an isothermal transformation. The austenite grain size increases as the temperature increases in both steels. It is noteworthy that there were two different samples, A and B with different chemical composition Table 2-4. This experiment came with two different approaches, with respect to the bainite transformation rate. Steel A showed that increasing austenite grain size led to raising the transformation rate, while steel B showed opposite results. Bainite sheaves consist of a group of fine plates. Bainite sheaves start to take shape at the grain boundaries and then continue to form inside the grains. This phenomenon makes the growing of bainite sheaves become distinct in steels A and B. The difference between the growth rate of bainite sheaves and the rate of nucleation is high at the austenite grain surfaces in steel A. Then, the austenite sheaf break throws the grain immediately until impingement occurs. In steel B, the growth rate is too slow compared to that of steel A. So, the impingement happens after the nucleation of the austenite grain boundaries has finished.

Plate and the bainite sheaf play a main role in the nucleation and growth of bainite transformation [80].

Table 2-4 Chemical compositions of steels A and B, all in wt% [80].

Steel	C	Si	Mn	Cr	Fe
A	0.12	2.03	0.96	……	Bal
B	0.96	0.21	0.38	1.26	Bal

The last opinion was reported by Yamamoto et al. [82] that there is not any noticeable PAGS effect on the decomposition of austenite to bainite under continuous cooling conditions. Steels employed in this experiment were low carbon with 3%wt. Mn with the chemical composition in shown in Table 2-5. The temperatures of reheating and deformation conditions meant the samples were different in order to alter the austenite grain size. 1200 ºC and 1160 ºC were the reheating temperatures, reduced to 800 ºC with a fixed cooling rate at 10 ºCº/s and after that the cooling rate was changed. The equiaxed grain diameters were 200 µm, 20 µm and elongated grain with diameter 20 µm. At a cooling rate above 5 ºC/s, fully bainitic ferrite was formed, while quasi-polygonal ferrite was formed. The transformation temperature of bainitic ferrite and hardness were not changed [82].

Table 2-5 Chemistry of steels employed in the experiment, all in wt% [82].

Steel	C	Si	Mn	P	S	Mo	Nb	Ti	Al	B	N
1	0.04	0.2	2.94	0.001	0.0004	-	0.028	0.023	0.017	0.0002	0.0018
2	0.04	0.2	2.95	0.001	0.0004	-	-	0.002	0.017	0.0003	0.0019
3	0.178	0.21	1.72	0.008	0.0020	0.25	0.039	0.011	0.024	0.0003	0.0052

2.11 Other Factors Affect the Transformation to Bainite

The bainite transformation is still probably the least understood of all the austenitic decomposition reactions [34], [79]. Catteau et al. [28] studied the effect of carbon and nitrogen on the rate transformation in low alloy steel at a temperature of 900 ºC and found that both

elements slowed down the phase transformation from austenite to bainite. The project was launched to analyse the phase transformation of a low alloy steel. $23MnCr_{23}Mo_5$, under isothermal conditions and chemistry was in range of 0.03-0.1 wt.% carbon and 0.25 wt. %N. The treatment was at temperature 900 ºC, producing an austenite grain size of 12 µm, followed by quenching in oil to a variety of different temperatures. Nitrogen enrichment stabilises austenite and promotes CrN nitride precipitation at the austenite grain boundaries leading to fine bainitic ferrite microstructure, which contains the CrN nitrides and nucleation sites that have been identified as mainly γ/γ grain boundaries with homogeneous precipitation. Increasing carbon content stabilises austenite to lower temperatures making bainite more difficult to form and enhancing the likelihood of martensite formation [28].

2.12 Microstructure and Mechanical Proprieties

2.12.1 Solid Solution Strengthening

There are two types of solid solution strengthening; one being substitutional solid solution where the solute atoms are of similar size in comparison to solvent atoms in the lattice and occupy equivalent lattice points; the second is interstitial solid solution where the solute atoms are much smaller than the solvent lattice atoms and occupy interstitial lattice positions within the solvent crystal structure. In both cases, however, the solute elements tend to elastically distort the lattice that interacts with the strain field of the dislocations, impeding their motion and increasing the strength of the material.

Depending on the size of the solute atoms the range of the effect of the solid solution strengthening is determined by the difference in the size between the solute and the solvent atoms. The Hume-Rothery's [83] rule states that for substitutional solid solution formation to be favorable, the difference of the atomic radius of the solute element should be no more than 15% of the solvent atomic lattice matrix (Fe, host phase); if the difference between them is greater the 15% the extent of solid solubility is restricted to less than 1% [83]. On the other hand, for interstitial solid solutions, the interstitial elements e.g. carbon, nitrogen, oxygen, hydrogen, and boron should be smaller than the solvent atomic lattice matrix as they would occupy the interstitial positions. In both cases, however, the solute substitutional element tends to elastically distort the lattice

2.12.2 Precipitation Strengthening

Precipitation strengthening is another important strengthening mechanism in HSLA steels. Dislocations will interact with the particles either by cutting through the them or loop around them, both of which require extra work therefore increasing strength. The extent of strengthening resulting from particles depends on their coherency with the matrix, distribution in the matrix, including volume fraction, average particle diameter, and mean interparticle spacing.

2.12.3 Work Hardening or Dislocation Strengthening

Permanent plastic deformation produces an increase in the number of dislocations. As a consequence, the average distance between dislocations decreases. On average, dislocation to dislocation strain interactions are repulsive. The net result is that the motion of a dislocation is hindered by the presence of other dislocations, leading to an increase in strength [84], [85].

2.13 Effect Carbide, Lath, Blocks and Packet size on Mechanical Proprieties

There has been a controversial debate about the impact of the lath, carbide, block and packet size and morphology on steel mechanical behaviour [86]. It is clear that through the Hall-Petch relationship a reduction in the structural unit size, e.g., grain or lath size, the strength and toughness increase. However, the effect of other microstructure features such as carbides, blocks and packet sizes are not as straight forward. Though there are some clear observations such as carbide size effects. Fine carbides, for example, act as a crack deflector increasing toughness, while cracks tend to go through coarse carbides leading to a reduction in toughness [87]. It has been stated that blocks and packets size have an effect on strength and toughness [52], [88]–[90]. Finer blocks or packets sizes increase improve the mechanical properties [52], [88], [90]. Adjacent packets boundaries act as a killing cleavage crack propagation because of the fact that it needs higher energy to cross the packets boundaries. It has been reported that crystallographic misorientations over 20° play that roles [52]. In some cases, it has been suggested that lath boundaries are take into consideration to be low angle grain boundaries, so they do not obtained an effect barriers [90].

It vital to define the lath, block and pocket before start discuss them. A block is a group of laths with near of same orientation and a packet a group of blocks with the same habit plane. Figure 2-18 shows a schematic figure representing the lath, block and packet in a martensite microstructure [87], [88]. For a coarse PAGS, the grain can divide into several packets. while

with finer PAGS only one packet is often detected [91], [92]. Sub-block is a lath stack with the same habit plane and same parallel direction, and it has a lath misorientations around 3° and never more than 5° [87].

2.13.1 Carbide Precipitation

Alloying elements such as Fe, Cr, Ni start to diffuse at around at 650 °C and enhance the carbide growth. On the other hand, other alloy elements play a vital role to hinder the carbide growth by stabilize the carbide coarsening, e.g. Si [93]. Alloying elements have many effects through many different mechanisms. Key amongst these mechanisms is retarding carbide nucleation and growth in martensite leading to finer carbides being formed during tempering. This is because the diffusion rates these elements is slower than the smaller interstitials, e.g., carbon [94]. Alloying elements also retard recovery of dislocations in martensite and bainite through solute drag effects making it more difficult to form low angle boundaries and have recrystallisation. Alloy elements such as Mo, Cr or Mn also reduce the chance of formation of Fe_3C cementite due to formation of complex metal carbides, i.e., complex carbides such as Cr-reach carbide ($M_{23}\,C_6$ or $M_7\,C_3$) form rather than Fe_3C cementite [65].

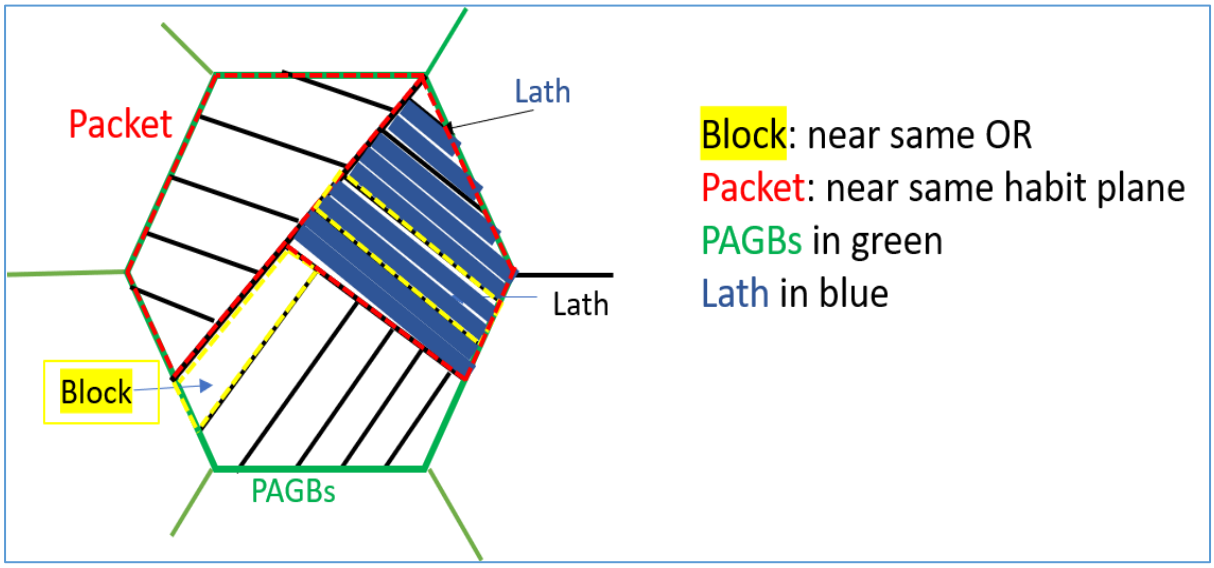

Figure 2-18 Schematic graph of definition of lath, block and pocket (modified) [87].

2.13.2 Tensile Strength

Previous research on HSLA steel has stated that the tensile strength depends on many factors for instance: grain size, carbide size and density, packet size and lath size. It is clear that

reduction of lath and block size increases strength through the Hall-Petch relationship [96]. Some researchers though have noted that changing PAGS does not change the lath width, so there in no PAGS effect on the tensile strength [95]. Another factor that can reduce tensile strength is increasing carbide size. Coarse carbides often crack in the early stages of deformation leading to tensile void formation and early localized necking [96], [99]. Fine carbides, on the other hand, lead to higher tensile strength due to higher rates of work hardening [88]. It has been suggested that tensile strength value is directly proportional to dislocation density [97].

In the case of bainitic microstructure, bainite plate size affects the tensile strength through the Hall-Petch relationship [98]. Elongation to failure, i.e., ductility, is affected by volume fraction of cementite and carbide precipitation, so decreasing the cementite volume fraction leads to an increase in the ductility and increases the elongation, however, this reduces the strength owing to less obstacles to dislocation motion [96], [99].

2.13.3 Toughness

The Charpy V-notch impact testing has been used for a long time in order to estimate the magnitude of energy absorbed by the tested specimen during fracture. The test evaluates the energy absorbed by notched of standard dimensions subjected to an impact loading. A high toughness material will absorb large level of energy and exhibit large levels of ductility, while a brittle/low toughness material will absorb very little energy [100], [101], [102]. As a general rule, reducing PAGS increases toughness, owing to finer packet and laths sizes making crack propagation more difficult. Furthermore, a finer PAGS means there are more high angle boundaries (>15°) per unit volume, which again are effective barriers to crack propagation [103]. This is not, however, a view held by all. He [66] states that many different factors can affect bainitic steel toughness, such as the packet and carbide size, but varying PAGS did not show any difference in toughness [66]. However, in mixed microstructures of bainite and martensite the volume fraction of each phase as well as the morphology and distribution of each phase influences the total resistance to crack propagation. [104].

It has been suggested that decreasing the volume fraction of coarse carbides, which can facilitate cleavage fracture initiation may be a more functional technique to improve the fracture toughness than the decreasing grain size or lath or packet size for both bainite and martensite [6], [105], [109]. Furthermore, it has been stated by Zhang and Knott [106] that a

finer carbide is related to a lower stress due to the ability of the ferritic matrix to deform plastically rather than fracturing..

2.14 Summary

This chapter has reviewed the state art of knowledge and underlining metallurgy of the manufacturer of structure critical PRVs for use in nuclear power plants. It is well known that because of the risk averse nature of nuclear power plant design and operation the alloy used for RPVs (SA508) will not change, and therefore to go to thicker RPV sections for next generation power plants there must be greater understanding of how the microstructure evolves and can be controlled during manufacture. A key element where there is little information in the effect of prior austenite grain size on transformation product and morphology, particularly under the cooling rates the RPV would experience during the quality heat treatment of future RPVs with steel SA508 G4N. Thus, the objective of this work is to understand the effect of PAGS on microstructure evolution to give clear guidance to the nuclear industry about any potential issues that having varying austenite grain size may have in future performance in service.

3. Experimental Methodology and Justification

3.1. Chapter Overview

This chapter provides an overview of the SA508 Grade 4N material investigated, in respect to the material processing, chemical composition, and heat treatment. This is then followed by details of microstructure observation techniques used and method of hardness testing.

3.2. As-received Material

SA508 Gr 4N steel of cubic shape with dimensions of 250x150x200 mm was provided from an unspecified part of an experimental forged RPV from Sheffield Foragemasters, Figure 3-1.

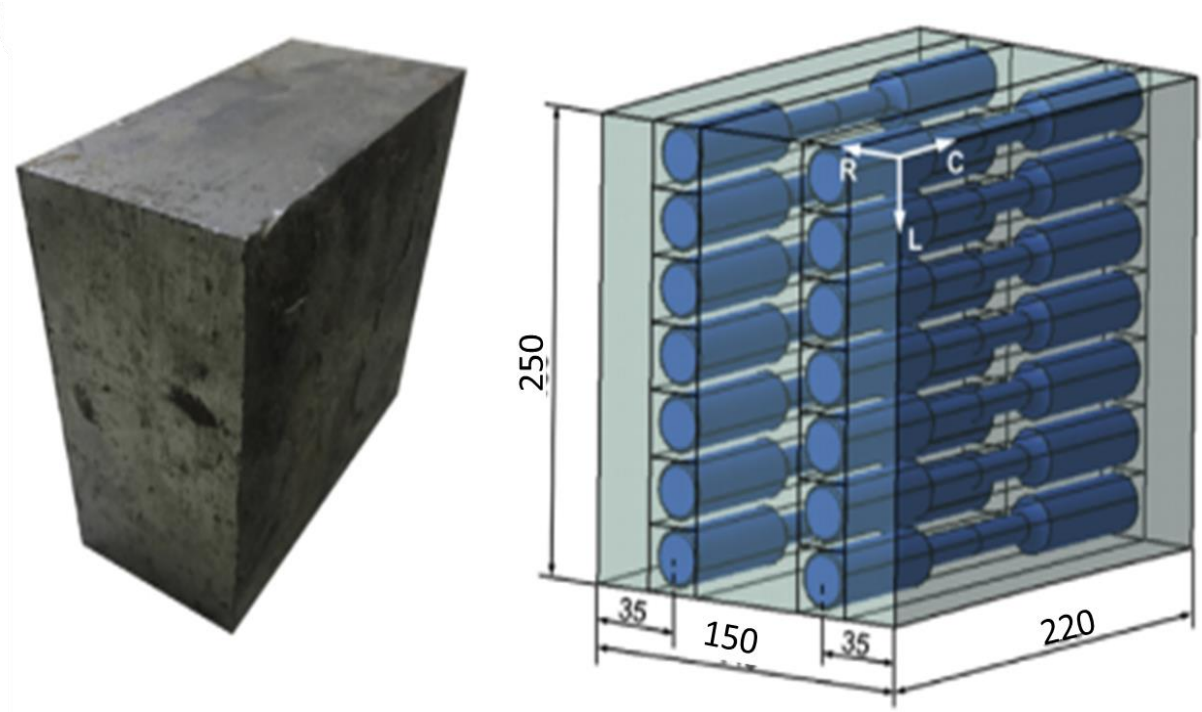

Figure 3-1 Schematic of selected samples from as-received specimen.

3.3. Materiel Chemical Composition

The chemical composition of the SA508 G4N as-received materials and the ASTM standards are given in Table 3-1.

Table 3-1 Chemical composition of the investigated steel and ASTM requirement, all in wt% [17].

Steel	C	Mn	Ni	Si	Cr	Mo
ASTM (G4N)	C<0.23	0.2-0.4	2.8-3.9	< 0.4	1.5-2.0	0.4-0.6
As received (G4N)	0.22	0.3	3.5	0.4	1.6	0.4

3.4. Thermal Simulation

The effect of PAGS and cooling rate on austenite was investigated using a dilatometer technique developed in-house at the University of Sheffield, known as simulator UT2-250, shown in Figure 3-2 and Figure 3-3. The machine heats rod shaped samples 150 mm long and 12 mm diameter at controlled heating rate and cooling rates using a combination of induction heating and water and air cooling. Temperature is controlled using a k-type thermocouple embedded into the centre of the sample, as shown in Figure 3-4. The system also has a laser based non-contact displacement measurement system to measure the dilatation of the test sample, enabling the machine to act as a kind of dilatometer. This enables transformation start and finish temperatures to be correlated to microstructure observations post heat treatment and the building of CCT like diagrams. Experimental noise is the main disadvantage of a dilatometry curve that make the curve is not highly precise. Uncertainty values can be found in the curve due to the noise appears in very small zone and critical part in the curve. The experimental noise was significantly larger at a cooling rate of 0.07 °C/s, between 550 °C and 650 °C. A MATLAB programme was used to reduce experimental signal noise.

Figure 3-2 Thermal conductor simulator machine.

Figure 3-3 Thermal conductor simulator machine.

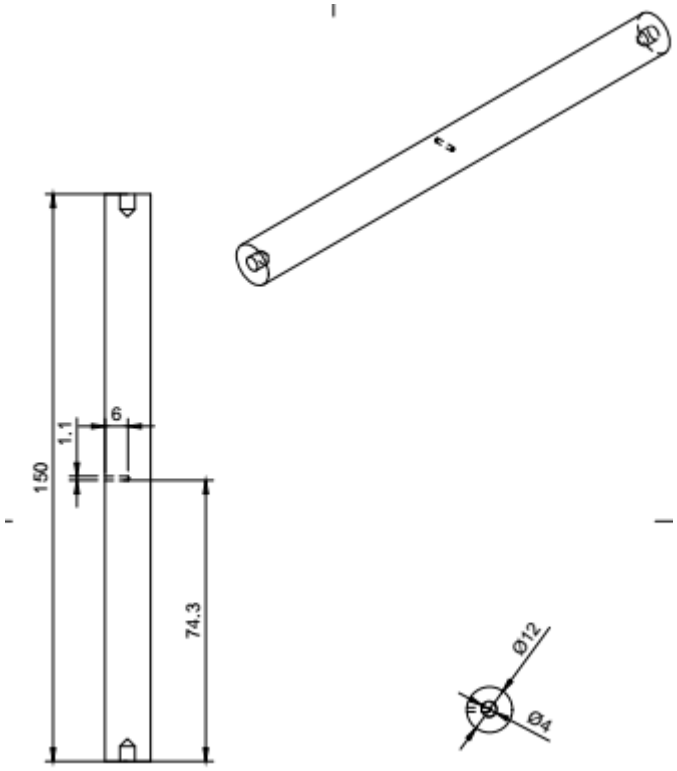

Figure 3-4 Schematic illustration of simulated specimen.

3.5. Experiment for SA508 G4N Steel

Owing to health and safety considerations in the laboratory any single heat treatment was time constrained to be a maximum of 9 hours. This included the heat up time, time for austenitisation and then controlled cooling period. It was decided that the maximum austenite austenitisation time to generate different PAGS could be no longer than 5 hours. Following literature using Equation 2.10, it was decided that to produce a fine, medium and coarse PAGS at 5 hours holding time, the austenitisation temperatures would be 950 ºC, 1100 ºC and 1175 ºC, respectively.

In order to investigate the effect of PAGS on microstructure and mechanical properties as a function of different cooling rates, all were specimens heated up at 10 ºC/s up to 950 ºC, 1100 ºC or 1175 ºC for 5 h. Then, all specimens were cooled to 850 ºC at 5 ºC/s, held for 5 min to stabilise the temperature and make all specimens start from same temperature after austenitisation and then cooled at different cooling rates of 0.07 ºC/s, 0.3 ºC/s and 3.0 ºC/s to room temperature. Moreover, it has been stated in ASTM that is austenitisation temperature

between 840 ºC and 895 ºC [17]. A sample of material heated to the different austenitisation temperatures was also directly water quenched to accurately determine the PAGS for each austenitisation condition. Figure 3-5 shows these cooling rates overlayed on a published CCT diagram covering expected microstructures from martensite to bainite. The slowest cooling rate is similar to the cooling rate of a water quenched PRV at ¼ a wall thickness of diameter 700mm [39]. While, the faster cooling rate of 3.0 ºC/s has been chosen to produce a martensitic microstructure at greater than the ¼ wall thickness. Some sections of all test samples were then tempered in a standard furnace at 550 ºC for both 6 and 24 h to investigate microstructure evolution during tempering. A detailed schematic of the thermal history that the materials went under is shown in Figure 3-6 and an overview of the experimental flow is shown in Figure 3-8.

3.5.1 Dilatometry

Dilatometry measures the reduction or expansion of specimen's length during heat treatment and is one of the most powerful techniques for the study and analysis of transformations in steels, as it permits measurement of the reaction in terms of dimensional changes due to phase transformations. In this method, the linear expansion of a relatively small standard cylindrical specimen is measured as a function of temperature cycle, which is then plotted in the form of a dilatation curve. If there are no phase transformations present within the temperature range measured, then the slope of the curve is the coefficient of thermal expansion (CTE) of the material. However, if there is a phase change process undertaken within that temperature range there will be a deviation from the CTE slope because the change in volume associated with the rearrangement of atoms into a different crystal. More importantly, when the transformation begins, the dilation curve deviates from linearity and a clear transformation start temperature can be defined, and once the transformation ends it again returns to linear behaviour, representing the transformation end temperature because of the change of crystal structure of the transforming phase has a different specific volume. Once a transformation is completed, the dilatation returns to a linear relationship with temperature. An example of this is shown in Figure 2-8. Note, since the phases will be different prior and post transformation the CTEs will be different leading to different linear slopes.

As, outlined above, the transformation temperatures are defined as the beginning of the deviation from linearity of the dilatation plot. The small volumes of the transforming material, however, does not cause large deviations of linearity, making it non-trivial to accurately identify the transformation temperatures. An example of this methodology is shown in Figure

2-9 , showing three clear deviations from linearity for ferrite (Fs), bainite (Bs), and martensite (Ms) [61].

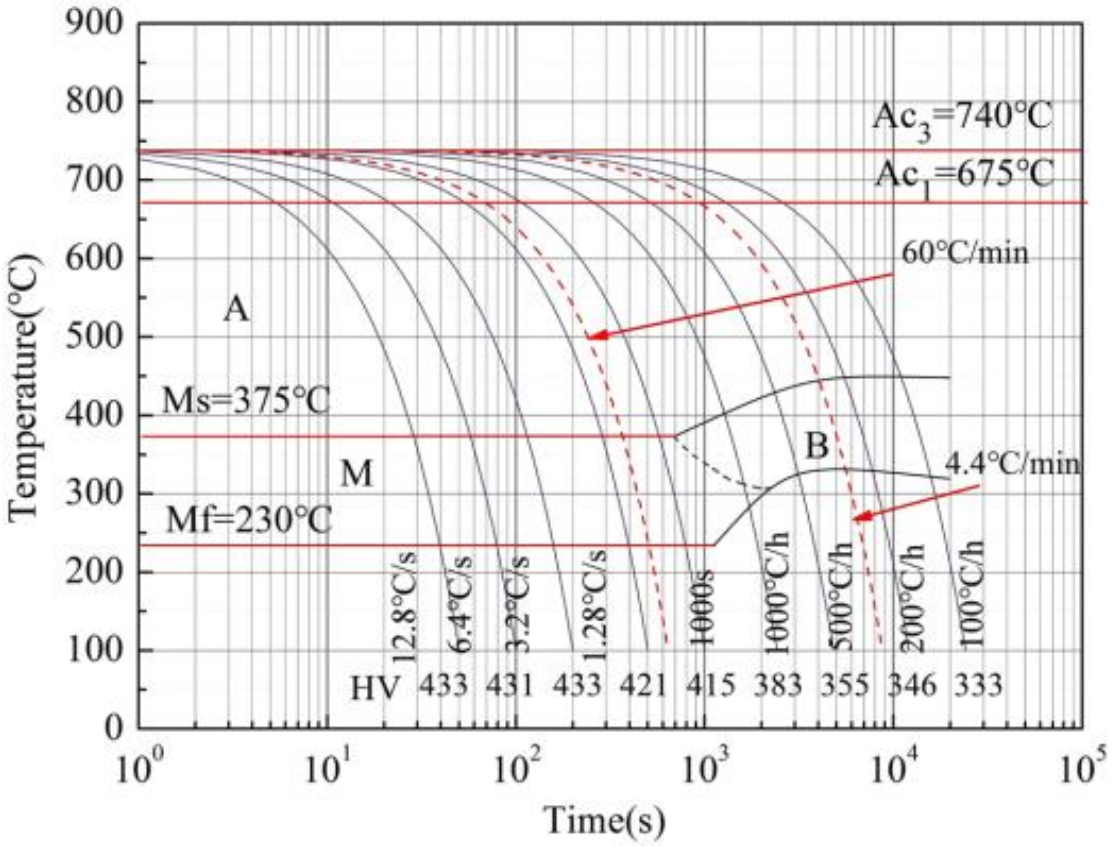

Figure 3-5 CCT Diagram of SA508 G4N [39].

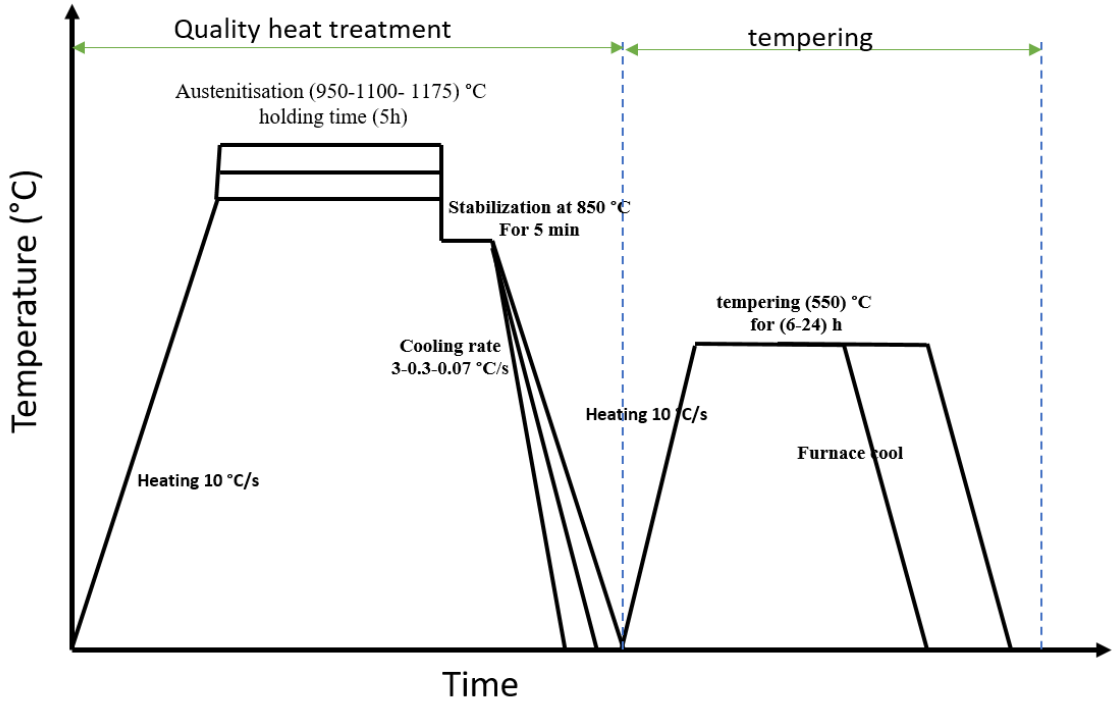

Figure 3-6 Schematic diagram of heat treatment process SA508 G4N experiment.

3.6. Microscopy

3.6.1. Optical Microscopy (OM)

Samples for both Optical Microscopy (OM) and Scanning Electron Microscopy (SEM) were prepared using the same procedure, in addition all tested specimens were selected from the middle. Firstly, all samples were mounted in conductive Bakelite and then ground with 240-grit silicon carbide paper then with successively finer papers up to 1200-grit. This was followed by polishing with diamond pastes of 3, 1 and 0.5 µm. In order to remove any residue at the surface, five minutes of ultrasonic cleaning in ethanol and air-drying at room temperature were implemented between each stage. The specimens were then etched by immersing in 2% Nital solution for 20-50s followed by cleaning in an ultrasonic bath.

To investigate the microstructures and measure PAGS, the low magnification features of each specimen's microstructure were investigated using a Nikon Optical Microscope (OM). Nikon Microscope has a magnification range of 50 to 1000X.

3.6.2 Scanning Electron Microscopy (SEM)

To gain more detailed analysis of the microstructure at higher magnifications SEM was employed. All microstructure analysis was undertaken at an operating voltage of 15-20 kV,

spot size 3.5 µm, and a working distance of 10 mm in the secondary imagining modes. Investigation of the SA508 G4N microstructure is a very challenging task due to the complex morphology. Figure 3-7 are references since (a) specimen is cooled with very slow cooling rate of 0.04 ºC/s (lower bainite), and (b) specimen quench with water (martensite).

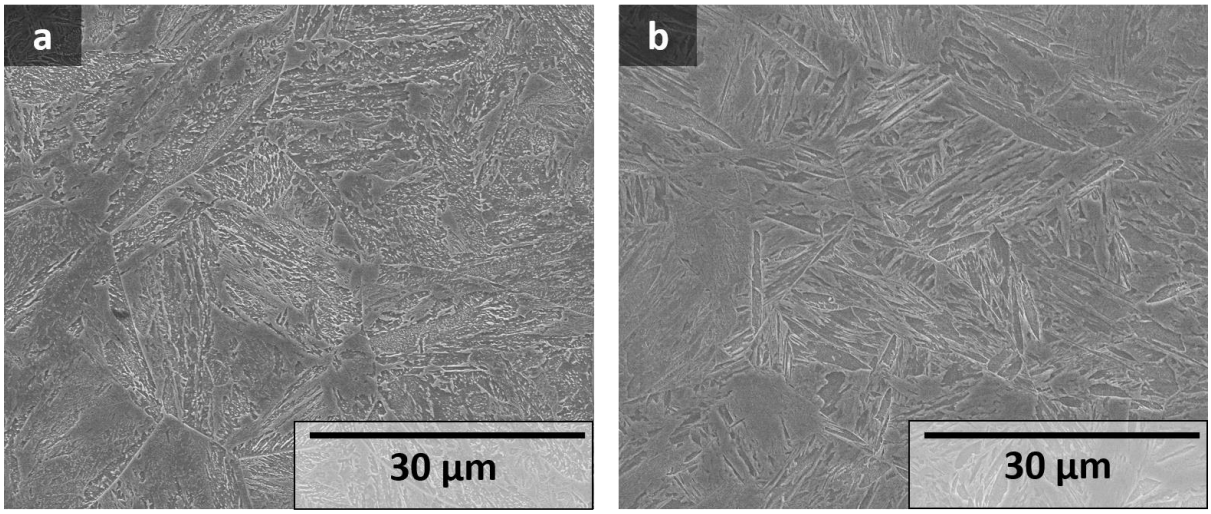

Figure 3-7 SEM images: (a) bainite with cooling rate of 0.04 ºC/s, (b) martensite with water quench.

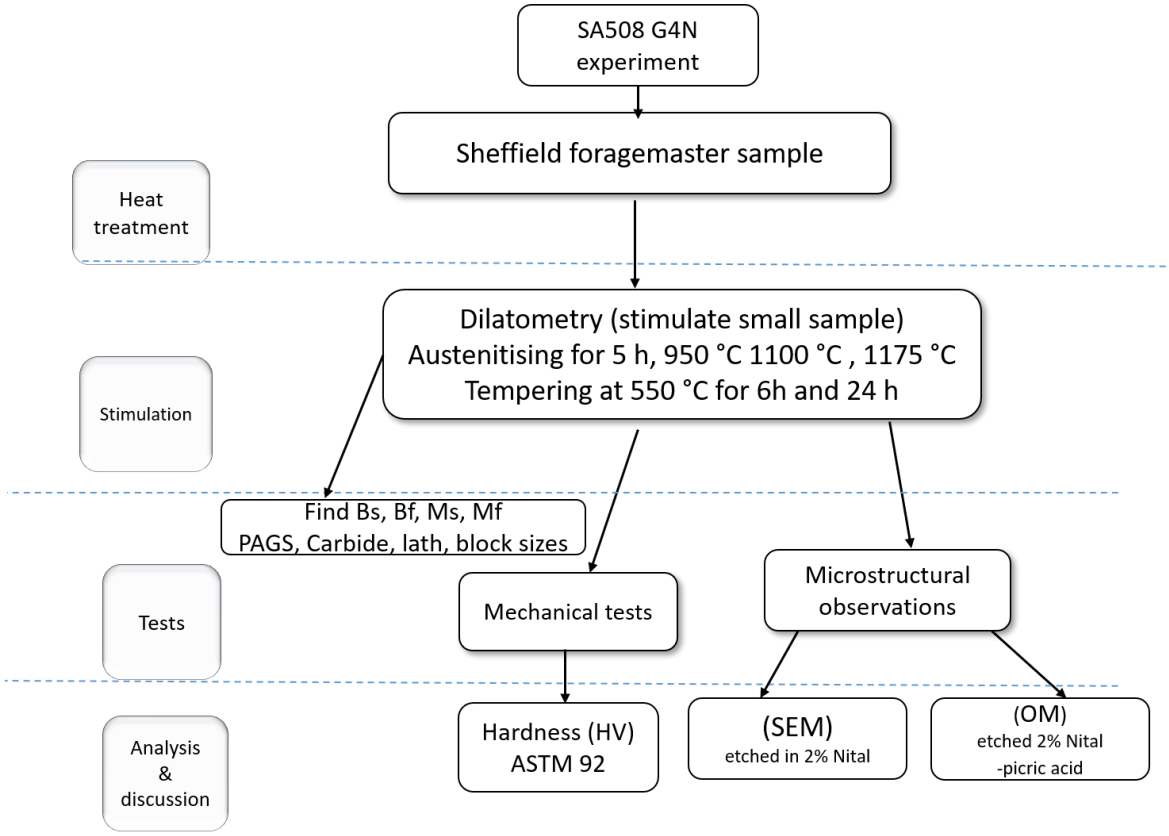

Figure 3-8 Summary of tests of solid solution of SA508 G4N.

3.7. Microstructure Quantification

To reveal the prior austenite boundaries for study using optical microscopy the as-quenched samples a special etching technique was developed. 100 ml picric acid with 100 ml of distilled water was heated up at 80 °C in order to acquire a completely saturated solution of picric acid. 2.5-3.0 ml of HCL was then added and heated to 85 ºC. A dummy sample was then immersed in the solution for 10 min. The real specimen was then immersed into the heated solution for 50 s and then cleaned with water and soup and then again immersed in the solution to around 60s. In some cases, the specimen required a light back polish for about 20s in order to reveal the prior austenite boundaries and make them clearer to see.

PAGS was measured by applying the ASTM E112-13 standard with the linear intercept procedure. Three different micrographs and at least four lines in each micrograph, e.g., Figure 3-9, were used to measure the PAGS for each condition [107]. 95% confidence interval method is used to estimate the uncertainty.

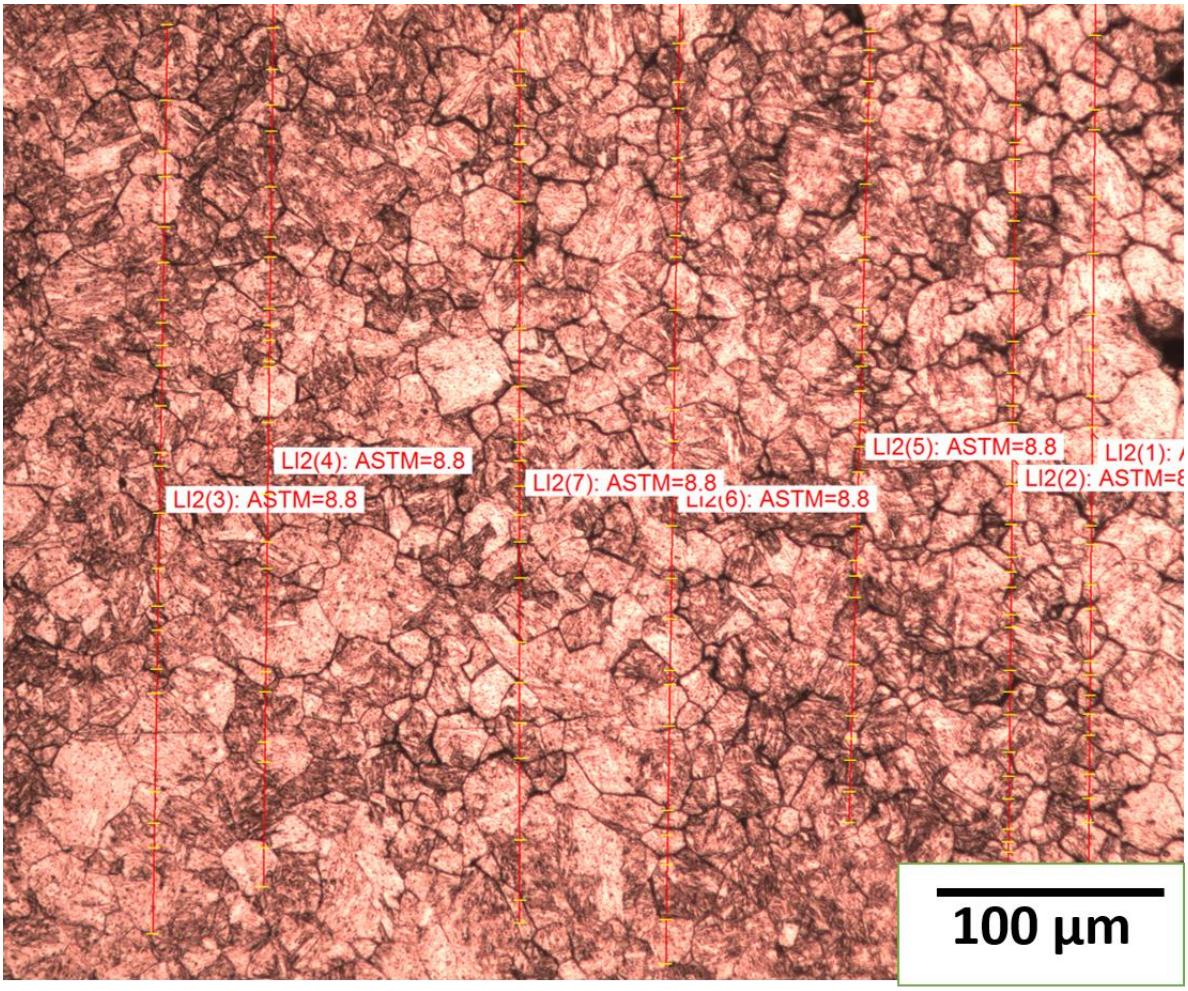

Figure 3-9 Intercept line method of measuring average grain size.

3.8. Carbide, Lath, and Block Measurement

Detailed analysis of the sizes of carbides, laths, and blocks were undertaken using SEM (carbide, lath and block). Evaluation carbides and lath sizes distribution in steel is not straightforward task, moreover it is complex and time consuming. The Image j software was employed for measurement for those microstructure features block, lath and carbide Figure 3-10. It involves preparing a metallographic sample and taking micrographs by SEM at 5000x or higher magnification. Then, calibrating the software with the scale bar on the SEM micrograph is the second step, and the images were selected from random areas. On average 100 readings per test condition were used to evaluate carbide and lath size, whilst around 20 readings were evaluated for estimating the block size. Samples were imaged by SEM at 5000x. Then, the image scale bar can be used to calibrate the software. Images were taken at random micrographs. 100 readings per test condition were used to evaluate carbide and lath size, around

20 readings were taken for estimating block size. Estimated sizes are 2 dimensional due to SEM images and a 95% confidence interval method is used to estimate the uncertainty.

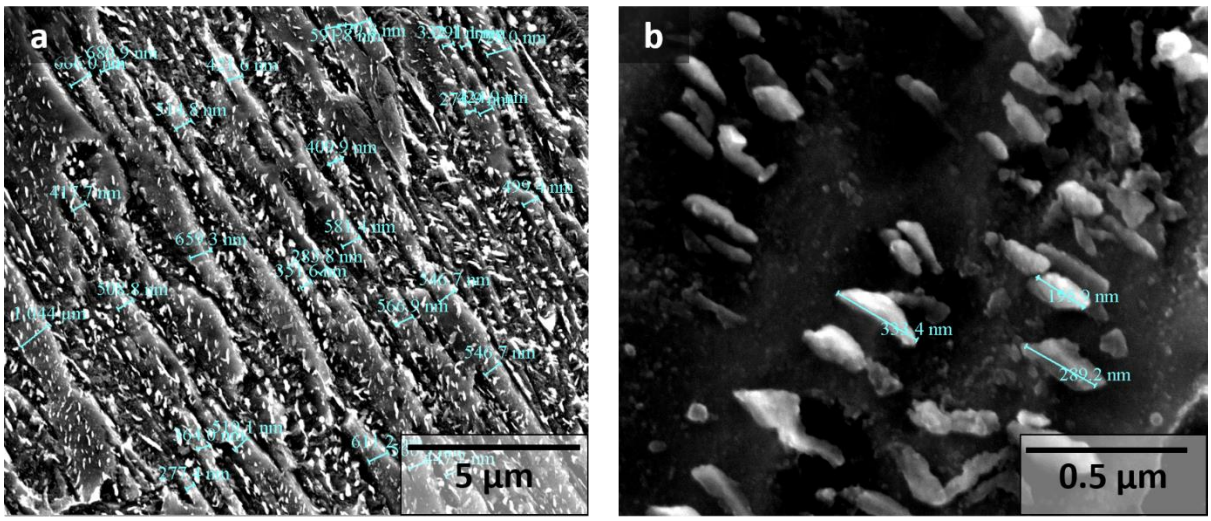

Figure 3-10 Methods of measuring specimen of PAGS 23 µm and cooling rate of 0.07 °C/s average (a) lath width and (b) carbide length.

3.9. Mechanical Test

Vickers Hardness (HV) testing, ASTM A92-16, was used to examine the hardness of each test specimen. The load range used was 10 kgf for 15 seconds. Ten readings were recorded for each specimen and the average value was taken as the HV. The indentions were conducted 1 mm from the specimen surface in order to avoid the decarbonised area.

4 Result and Discussion

4.1 Chapter Overview

This chapter characterizes the effect of PAGS on the transformation microstructure as a function of cooling rate on SA508 G4N. Also, a detailed statistical analysis of the evolution of carbide size as a function of cooling rate is given.

4.2 As-received Specimen

Figure 4-2 shows the microstructure of the as-received material using OM and SEM. The dark region represents tempered martensite (red circle), while the lighter phase is tempered lower bainite (yellow circle). Coarse equiaxed carbides (red arrows) have precipitated at the austenite grain boundaries and bainite lath boundaries, while finer equiaxed carbides (yellow arrows) form inside the laths, Figure 4-2b. There is no evidence of needle shape carbides within the as-received material's microstructure. There is, however, very clear Prior Austenite Grain Boundaries (PAGBs) (red lines) and triple junctions (yellow lines) in the as-received material's microstructure, Figure 4-2c.

4.3 Experiential Measurement of PAGS

Revealing PAGBs is a difficult process as a result of a number of factors, for instance steel phases present, chemical composition and manufacturing stages [78]. However, PAGBs can be revealed by several chemical etching procedures and many of these techniques were explored in this research before reaching the optimum solution that was described in Chapter 3. Achieving the perfect environment for revealing the boundaries needs several trial and error experiments and variation of several important factors, for example etching temperature, etching time, wetting agent, HCl acid percentage and cleaning sample surface methods. Furthermore, revealing PAGBs in SA508 G4N is a complex procedure due to mixed microstructures, i.e., bainite and martensite; moreover, it is difficult to distinguish between the austenite grain boundaries and packet boundaries. In addition, the etching method is a challenging technique for revealing PAGBs of low carbon steel with very low phosphorus levels as we have in SA508 G4N [108].

The grain boundaries are grooved by etching the samples with the aqueous picric acid, however, martensite lath and martensitic packet boundaries generate some level of uncertainty to what is a PAGB and what is a packet boundary. Figure 4-1 shows the optical micrographs of PAGS following quenching for three different austenitisation temperatures of 950 °C, 1100 °C and 1175 °C using the techniques developed as outlined in the experimental procedure.

It successfully revealed fully equiaxed austenite for all the heat treatments used in this research, though some level of interpretation is required to ensure no packet boundaries are defined as austenite boundaries.

Table 4-1 Comparison between the predicted Equation 2-10 and measured PAGS at austenitisation temperatures of 950, 1100 and 1175 °C for 5 h, ***95% confidence interval between bracket.***.

Austenitisation Temperature (°C)	**Measured (µm) (95% confidence interval)**	**Predicted (µm)**
(950 °C)	23 (±3.2)	43
(1100 °C)	83 (±5)	77
(1175 °C)	412 (±33)	102

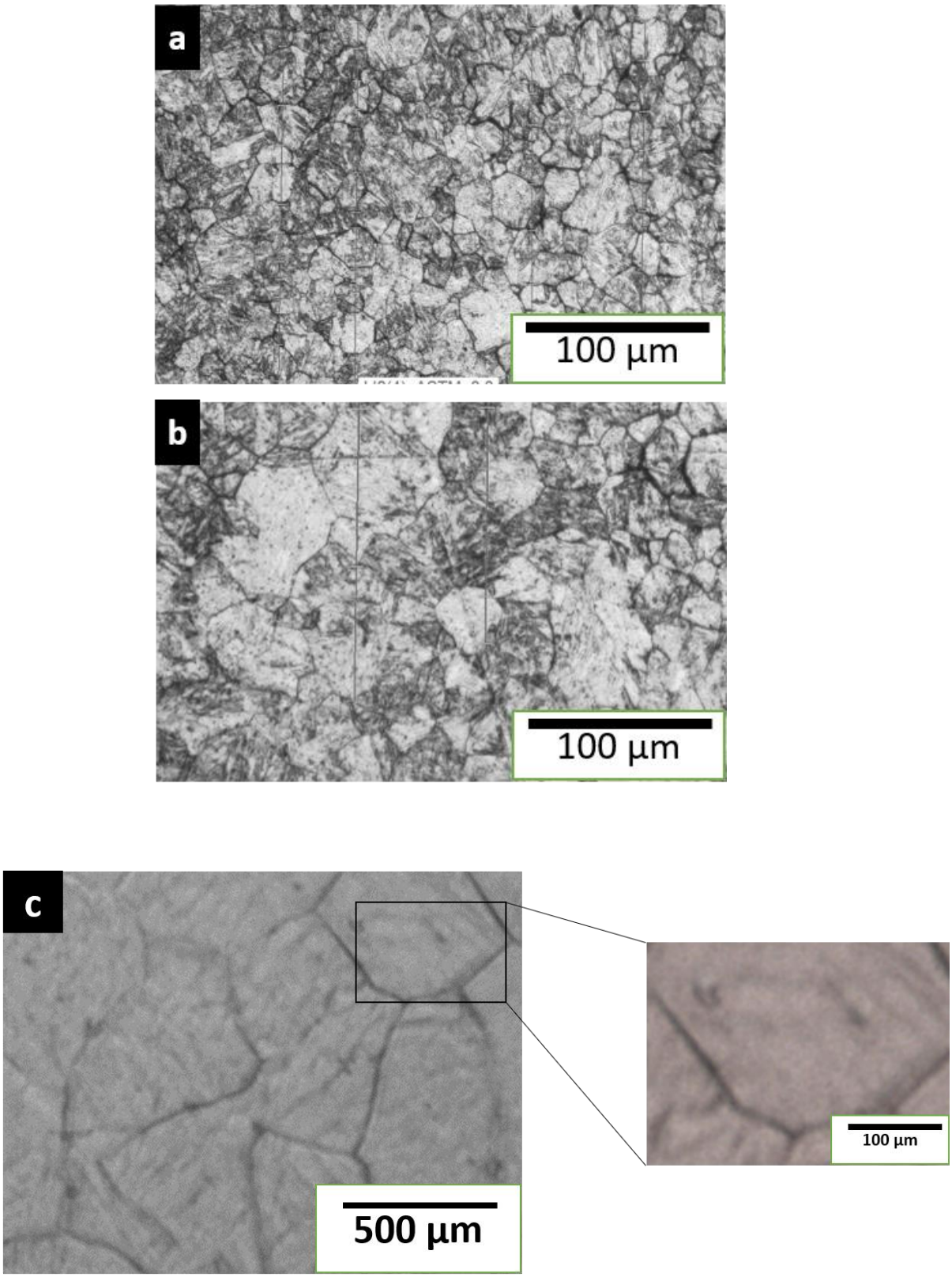

Figure 4-1 Optical microscope measurement of experimental PAGS at 5 h and austenitisation temperature at (a) 950 °C, (b)1100 °C and (c)1175 °C.

4.3.1 Predicted PAGS

Table 4-1 shows the measured PAGS, which are 23 μm, 83 μm and more than 412 μm, using the ASTM E112-13 linear intercept method, at the austenitisation temperatures of 950 °C, 1100 °C and 1175 °C, when held for 5 h. Figure 4-3 shows the predicted PAGS 83 μm, 150 μm, and 300 μm using Equation 2-8 at austenitisation temperatures of 950 °C, 1100 °C and 1175 °C for 5 h, respectively. Comparing between the predicted and measured PAGS when austenitisation temperatures are at 950 °C and 1100 °C there is around 100% difference with the predicted results, while when the austenitisation temperature is 1175 °C the predicted PAGS is less than the measured results by around 40 %. A similar result was also found using Equation 2-9. This large divergence between the predicated and measured PAGS indicates that Equation 2-8 and Equation 2-9 are not applicable for SA508 G4N.

Figure 4-4 shows the predicted PAGS using Equation 2-10. Table 4-1 compares the predicted and measured PAGS at the different austenitisation temperatures of 950 °C, 1100 °C and 1175 °C for 5 h. In this case there is only a 10% difference for 950 °C, and 1100 °C but a very large difference for 1175°C. This would suggest Equation 2-10 is much better for SA508 G4N but possibly not robust enough to be used for general use for SA508 G4N, particularly at very high temperatures.

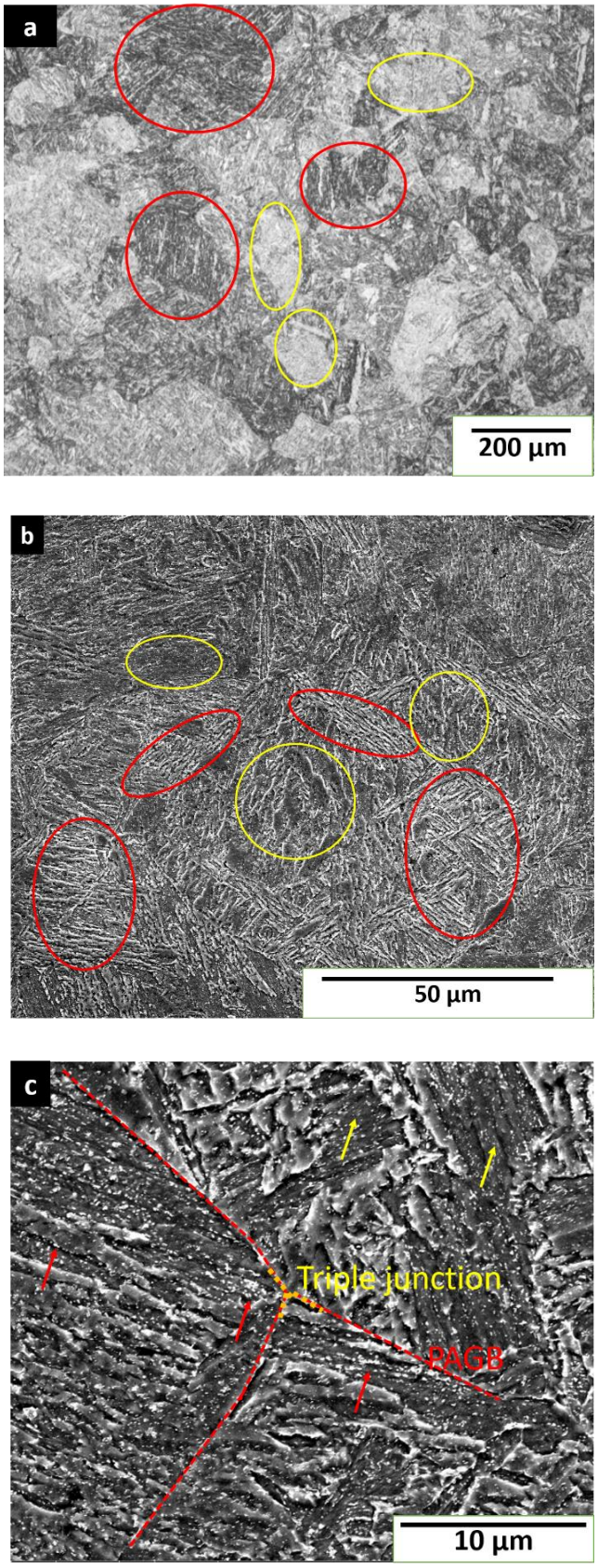

Figure 4-2 As-received material SA508 G4N (a) Optical microscope (b, c) SEM, red circle is tempered martensite, yellow is tempered lower bainite. Red arrows are coarse intra lath carbide, yellow arrows are inter lath carbide.

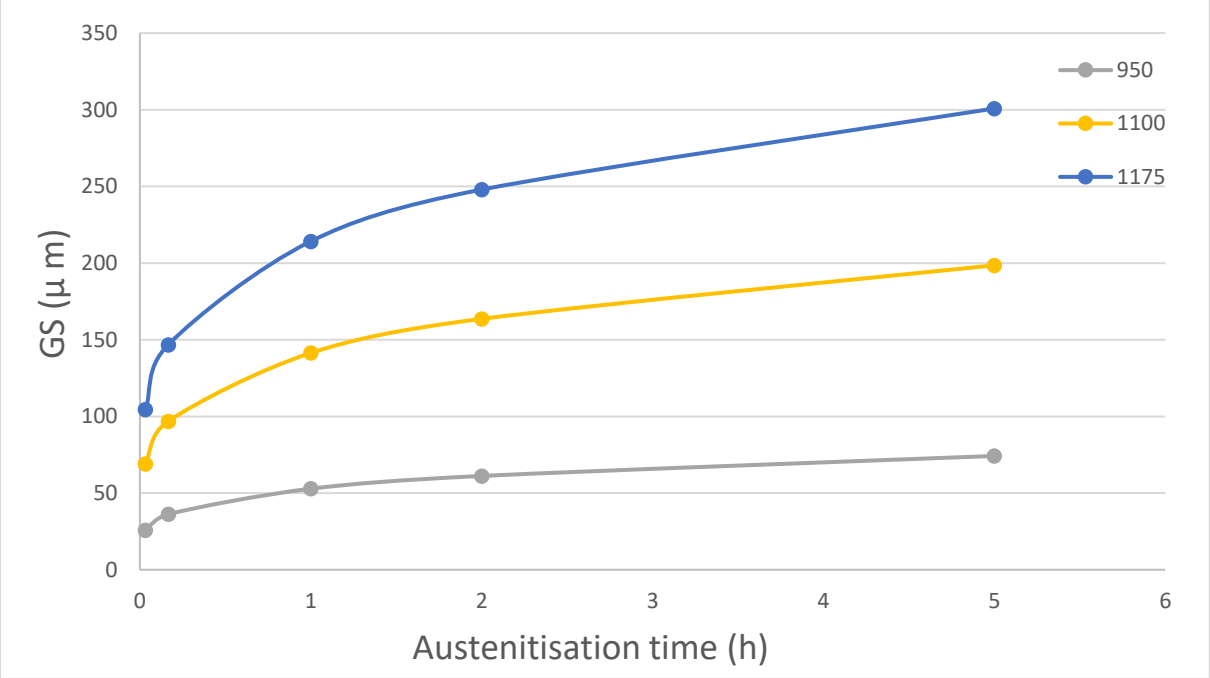

Figure 4-3 Predicting of PAGS at temperature of 950, 1100 and 1175 °C (83, 150, 300) µm receptivity Equation 2-8 and Equation 2-9.

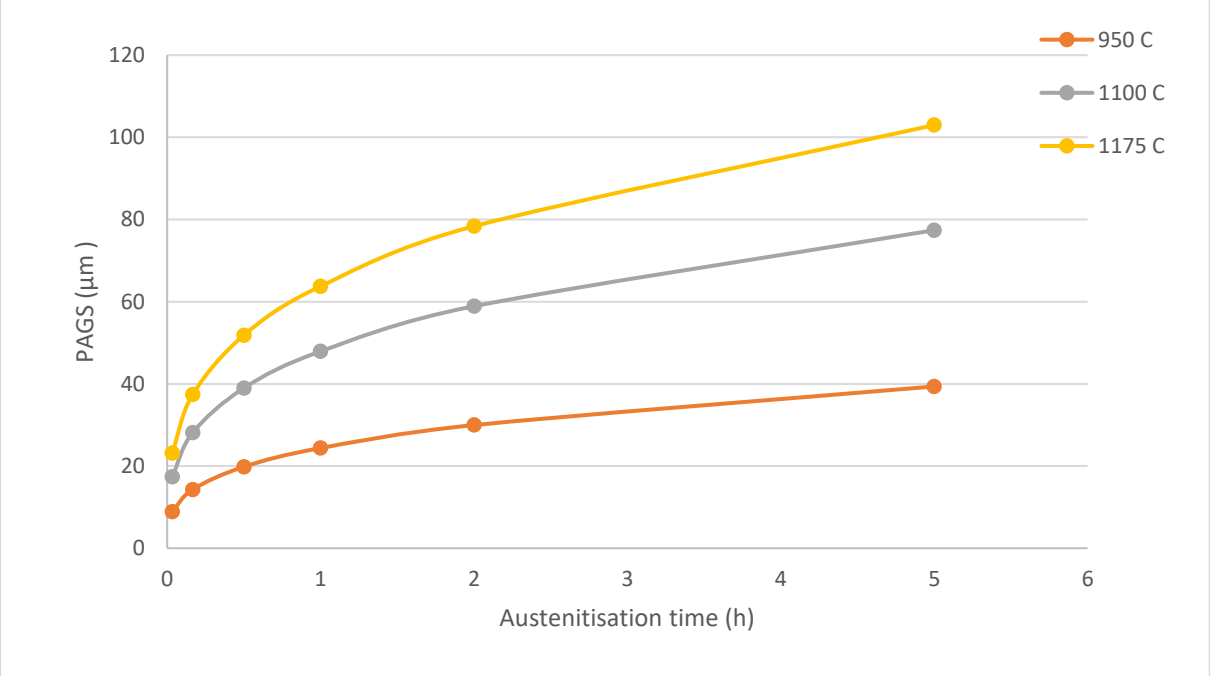

Figure 4-4 Predicting of PAGS at temperature of 950, 1100 and 1175 °C (43, 77, 102) µm receptivity Equation 2-10.

As can be seen from Figure 4-4, increasing the austenitisation temperature leads to an increase in the grain size at the same austenitisation time of 5 h, Table 4-1 [80]. In general, during the austenitisation stages, grains coarsen with larger grains consuming the finer ones [93]. It is, therefore, interesting to note that the difference between the predicted and measured PAGS for 1100 °C is less than 10%, while when the austenitisation temperature is 1175 °C there is a huge divergence between the predicated and measured PAGS using Equation 2-10. Thus, it might be that Equation 2-10 is not applicable at higher austenitisation temperatures or larger grain size or when slight differences in chemistry may play a significant role in determining the exact grain growth behaviour. For example, Xikou's [63] SA508 G4N material used to qualify Equation 2.10 and the material used here is slightly different. The most obvious difference in the chemical composition is that Xikou's material has lower C and Si contents, while it has higher Cr and Mo contents, Table 4-2. In addition, Xikou's did not provide any detail about Nb, V, Ti and Al content. The second phase particles, as an example, nitrides, carbides or complex carbonitrides have an obvious effect in the production process of HSLA steel. Moreover, physical properties such as impact toughness can be developed by microalloying element such as Nb, V, Ti and Al. On the other hand, embrittlement can be enhanced with precipitation of AlN. AlN, MnS and TiNbCN [109] also have a recognised effect on steel grain size growth. In the first glance, it can be recognised a steady state grain growth performance at temperature of 950 °C and 1100 °C, by contrast a significant grain size increase is observed when the austenitisation temperature around at 1175 °C. The deviation of grain size between austenitisation temperatures of 1100 °C and 1175 °C is probably associated with heterogeneous grain growth due to the partial dissolution of AlN precipitates at austenite grain boundaries [110], [111]. So, AlN particles acts as a pinning force that stabilises the grain growth when AlN is present. When austenitisation temperature is above 1135 °C, AlN partially starts to dissolve leading to a higher grain growth rate [109], [112]. This theory needs to analysis the AlN content of finer and coarse PAGS.

Table 4-2 Compares between as-received material and Xikou's material, all in wt%.

Steel	C	Mn	Ni	Si	Cr	Mo
As received (G4N)	0.22	0.3	3.5	0.4	1.6	0.4
Xikou's material	0.17	0.36	3.55	0.3	1.75	0.55

4.4 Dilatation

Because the RPV is a very thick component, the final microstructure during quenching from austenite will vary between the wall surface and the centre of the wall due to a large variation in cooling rate. Figure 4-5 shows the cooling curve at an intermediate point within a 320 mm thick section of SA508 G3 when water quenched. The cooling rate is approximately 0.2 °C/s in the region of the phase transformation, which is clearly much slower than water quenching. Thus, it is critical to understand how this variation in cooling rate will influence microstructure evolution.

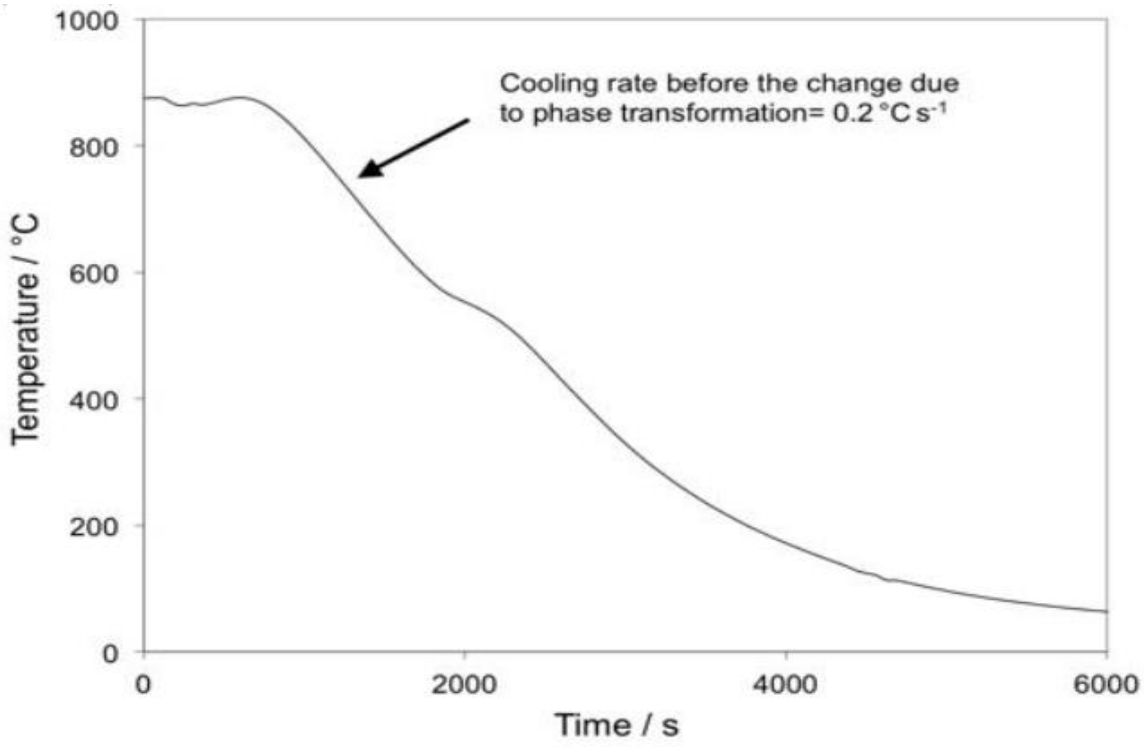

Figure 4-5 Measured cooling curve in the intermediate wall position of a 320 mm thick SA508 G3 component. Data courtesy of Rolls Royce Plc.

Dilatometric curves of continuous cooling rates at 0.07 °C/s, 0.3 °C/s and 3.0 °C/s with different PAGS can be seen in Figure 4-6, Figure 4-7 and Figure 4-8, respectively. The key point to note is there is no formation of ferrite or pearlite before the start of formation of bainite or martensite with the different cooling rates or variation of PAGS. This confirms that the addition of nickel for SA508 G4N has significantly increase hardenability and retarded the formation of ferrite in comparison to SA508 G3.

4.4.1 Martensite Start Temperature (Ms) and Bainite Start Temperature (Bs)

Table 4-3 shows the summary of the bainite start and finish temperatures (Bs, Bf) and the martensite start and finish temperatures (Ms, Mf), respectively. In general, increasing PAGS leads to an increase in the start temperature of both bainite and martensite. On the other hand, increasing cooling rate leads to an increase in lower bainite and martensite at a cooling rate of 0.3 °C/s and a fully martensitic structure with a cooling rate of 3.0 °C/s Figure 4-15k, while a lower cooling rate promotes a more lower bainite microstructure Figure 4-15c. In addition, starting with the largest grain size with cooling rate at 0.07 °C/s promotes granular bainite with a start temperature around 504 °C, while the intermediate PAGS decreases this temperature to around 483 °C. This is similar to previous observations that granular bainite tends to forms with coarse PAGS [100]. The martensite start temperature increases as a result of increasing PAGS, along with the martensite packet, block size, and lath width, as previously reported in similar studies [92], [113], [114]. Rising the austenitisation temperature drives the blocks to arrange in a more uniform order due to a reduction in the lath nucleation resistance. So, the block size increases rapidly [113]. On the other hand, increasing PAGS on bainitic morphology decreases the lath width.

4.4.2 The Effect of Variation of PAGS on Transformation Start Temperature

Figure 4-6 represents the variation of start and finish transformation temperatures of finer, intermediate and coarse PAGS with Cooling rate of 0.07 °C/s. There is no indication of transformation before the bainite start temperature, i.e., the cooling curve was relatively non-liner because of the dilatometer curve noise down until the bainite start, indicating no ferrite formation at higher temperatures. Increasing PAGS at cooling rate of 0.07 °C/s increases the bainite start formation temperature with it being 445 °C at the finest PAGS, 483 °C at the intermediate PAGS, and 504 °C for the coarse PAGS.

Figure 4-7 demonstrates the variation of start and finish transformation temperature of fine, intermediate and coarse PAGS with cooling rate of 0.3 °C/s. In the first stage of cooling, the cooling line is non-linear, again because of the dilatometer curve noise confirming no ferrite formation. In comparison to the 0.07 °C/s cooling rate, the bainite start temperatures are lower for the comparative grain sizes but it is interesting to note that the start temperatures are similar for the fine and intermediate PAGS, being 405 °C and 403 °C, respectively. At the coarse PAGS the transformation temperature is 473 °C.

Figure 4-8 shows the variation of start and finish transformation temperature of fine, intermediate and coarse PAGS with cooling rate of 3 °C/s. In the first stage of cooling, the cooling line is linear that indicates there is no transformation before the new phase starts formation. Thus, cooling line are liner without any deviation. At this cooling rate, based on a published CCT diagram, Figure 3-5, the transformation microstructure should be dominated by martensite. At finer PAGS, the transformation starts at 376 °C, while it increases to 405 °C with intermediate PAGS and it continues to increase by around 40 degree for the coarse PAGS. Table 4-3 summaries the measurement of bainite start and finish temperatures (Bs, Bf) and martensite start and finish temperatures (Ms, Mf) for the different austenitisation temperatures and different cooling rates.

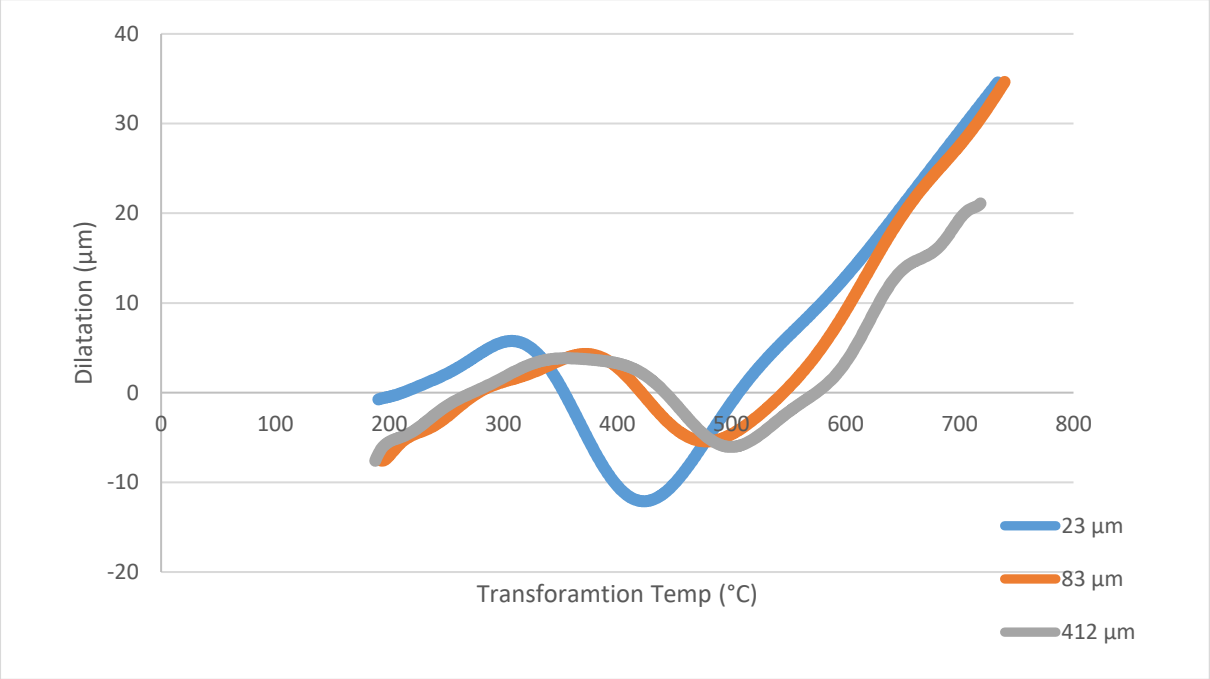

Figure 4-6 Represents the variation of start and finish transformation temperature of finer, intermediate and coarse PAGS with Cooling rate of 0.07 °C/s.

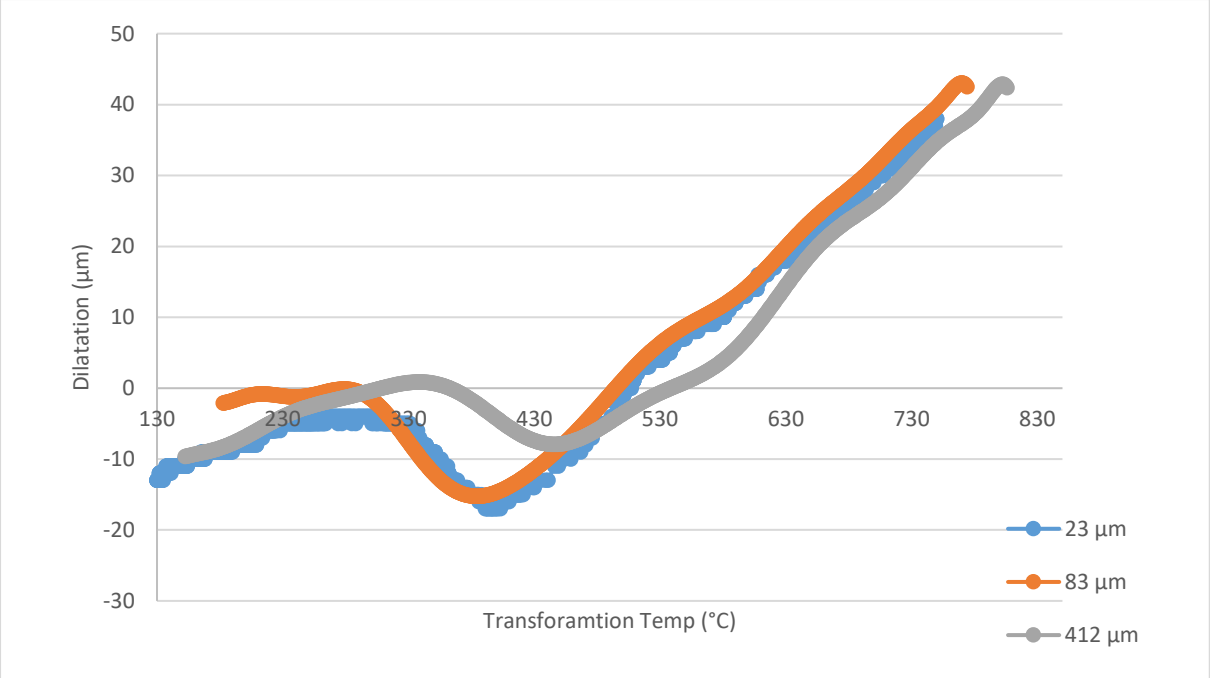

Figure 4-7 Shows the dilatation of finer, Intermediate and coarse PAGS with Cooling rate at 0.3 °C/s.

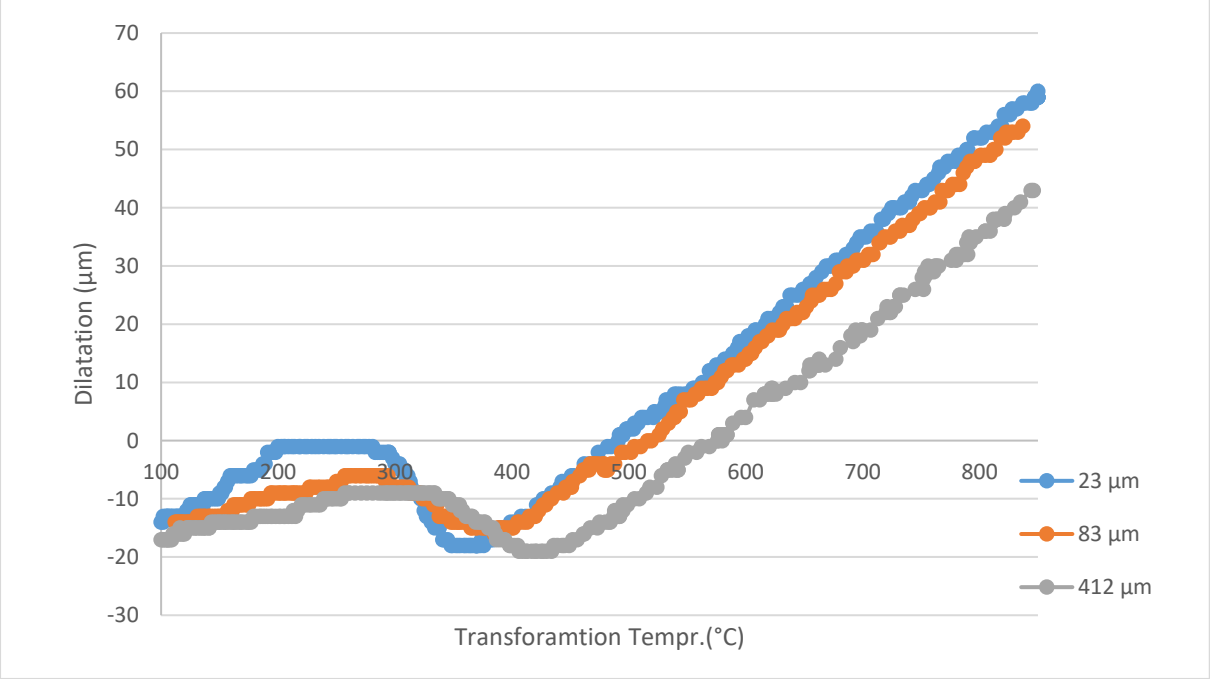

Figure 4-8 Shows the dilatation of finer, Intermediate and coarse PAGS with Cooling rate of 3.0 °C/s.

Figure 4-9 shows the second derivatives of finer, intermediate, and coarse PAGS with a cooling rate at 0.07 °C/s. In addition, Figure 4-10 illustrates the variation of start and finish

transformation temperatures of finer, intermediate, and coarse PAGS with cooling a rate of 0.3 °C/s. Due to limited data, the second derivative at a cooling rate of 3 °C/s was not obtained.

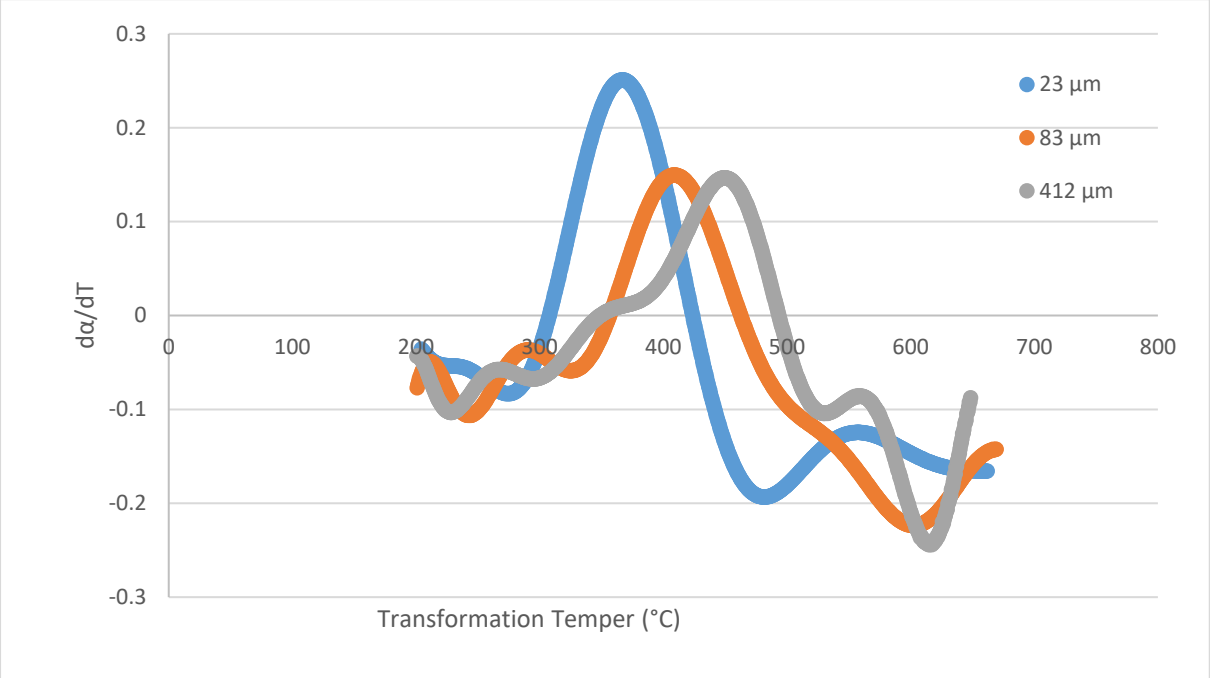

Figure 4-9 Shows the second derivative of finer, Intermediate and coarse PAGS with Cooling rate at 0.07 °C/s.

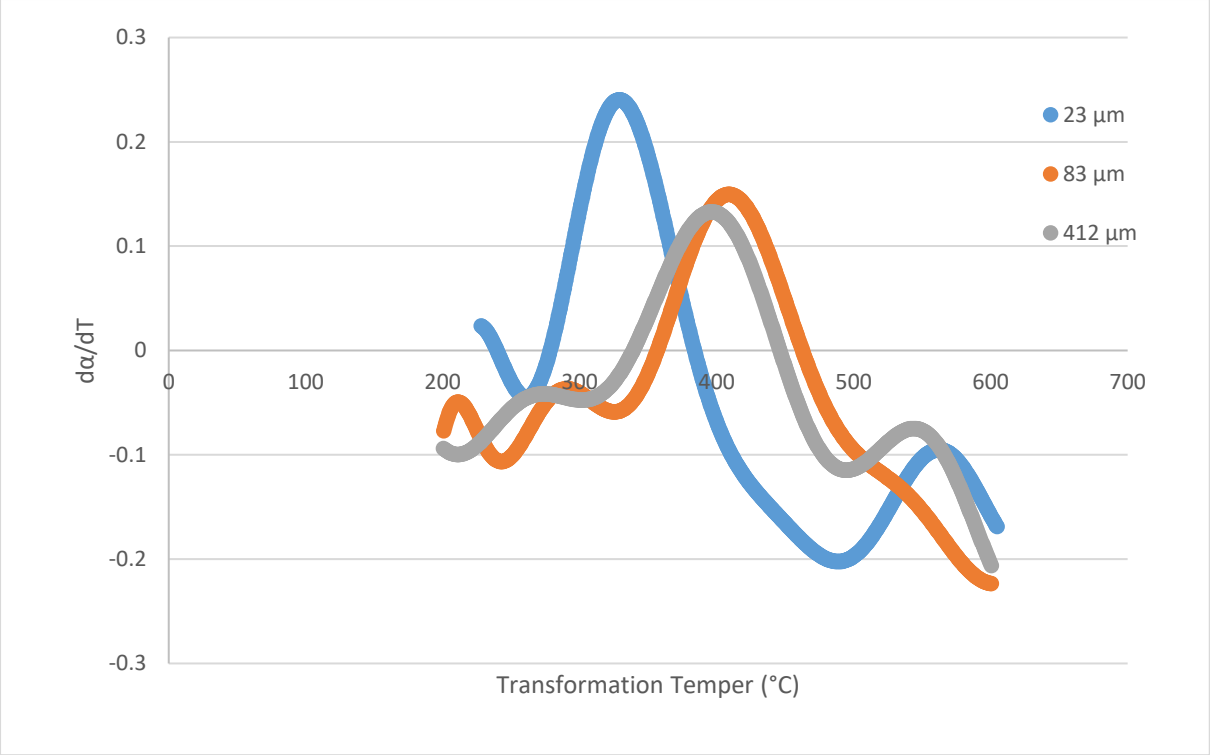

Figure 4-10 Shows the second derivative finer, Intermediate and coarse PAGS with Cooling rate at 0.3 °C/s.

Figure 4-11 overlays the results presented in Table 4-3 on a published CCT Diagram of the tested SA508 G4N. Figure 4-12 shows bar charts of the variation of transformation start temperatures and the different cooling rates of 0.07 °C/s, 0.3 °C/s, and 3 °C/s for fine, intermediate and coarse PAGS.

4.5 Carbide, Lath, and Block Size

It is vital to define what is a lath, a block and a packet before starting to discuss them. Figure 2-17 summaries the definition of lath, block and packet. The packet is crystallographic that has a group of blocks with the same habit plane, while a block is a group of laths of similar orientation. A sub-block is a lath stack with the same habit plane and same parallel direction [88], [115]. PAGS plays a role in determining the number of packets in the grain, with finer PAGS having mostly just one packet, while coarser grains are generally observed to contain more than one packet, Figure 4-13. In addition, bainitic lath width is highly temperature dependent, while lath length is less temperature dependent [116].

Table 4-3 Measurement of bainite start and finish temperature (Bs, Bf) and martensite start and finish temperature (Ms, Mf) with different austenitisation temperature and different cooling rate.

Austenitisation temp(°C)/ **Cooling rate (°C/s)**	Formation start (°C)	Formation finish (°C)
950/**0.07**	445	302
950/**0.3**	405	278
950/**3.0**	376	271
1100/**0.07**	483	353
1100/**0.3**	403	289
1100/**3.0**	405	277
1175/**0.07**	504	322
1175/**0.3**	473	332
1175/**3.0**	449	325

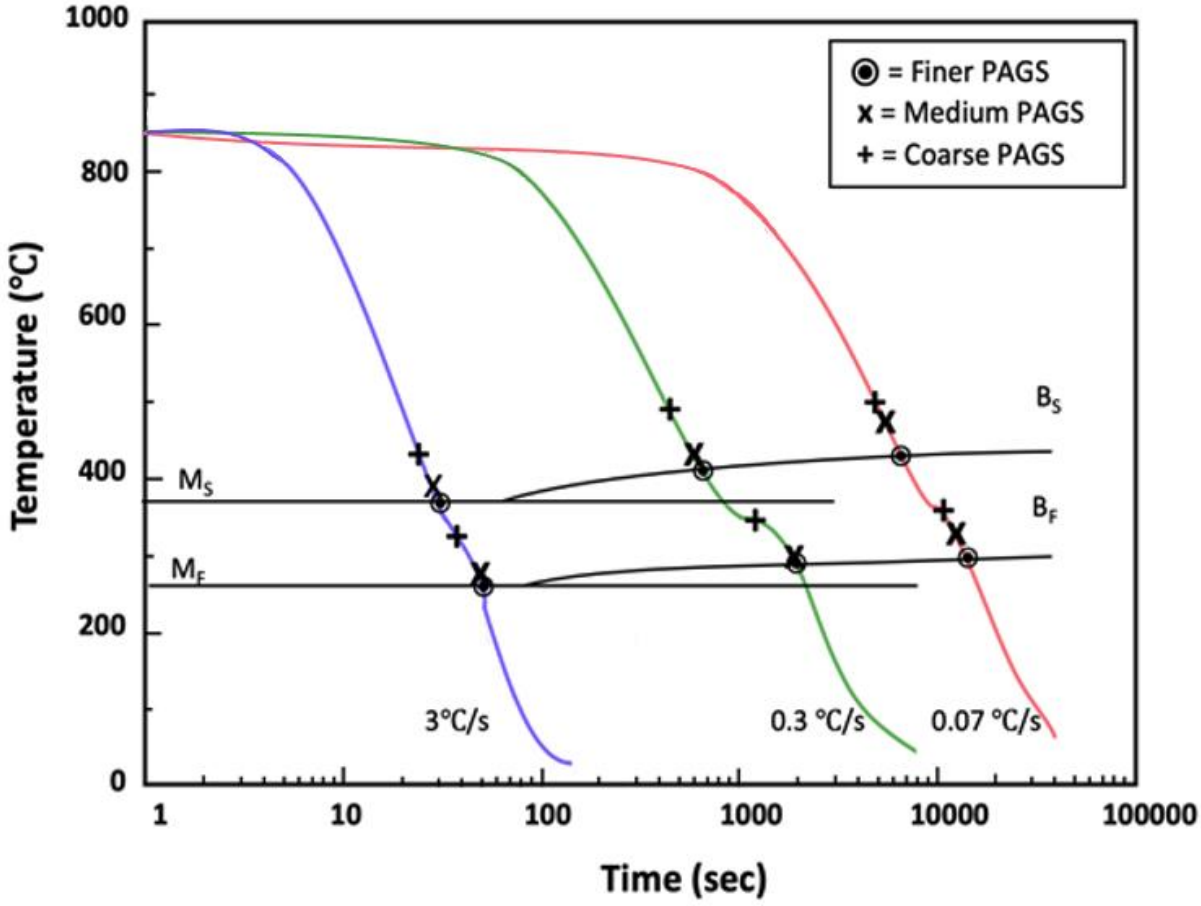

Figure 4-11 CCT Diagram of the tested SA508 G4N samples and selected cooling rates.

SEM analysis was used to characterise and measure the carbide, lath, block and packet size. The procedure for defining the carbide, lath, and block size and morphology for the as-cooled specimens is discussed in the experimental chapter. Table 4-4 shows the carbide length (nm), lath width (nm), and block (μm) size for the different PAGS and the different cooling rates. Generally, increasing the cooling rates from 0.07 °C/s to 3 °C/s leads to a decrease in the carbide, lath, and block sizes due to the transforming product changing from predominantly bainite to fully martensite. Formation of the new phase at lower start temperature leads to a decrease in carbide size because of less time for carbon to diffuse, meaning growth is limited. Also, as PAGS becomes coarser there is more chance for carbide, lath, block and packet to be coarse. However, lath width does not change a lot in comparison to the changes in block sizes. In addition, as the blocks or packets grow and become larger, the lath length has more chance to grow longer.

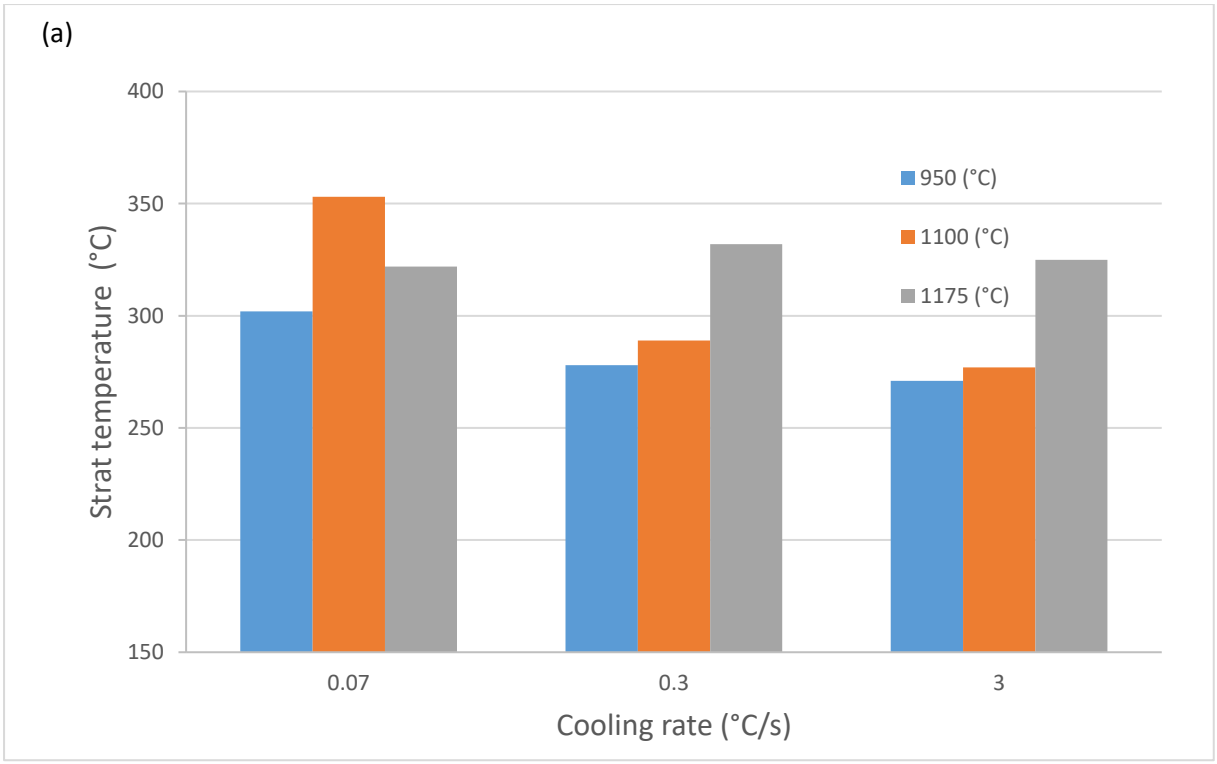

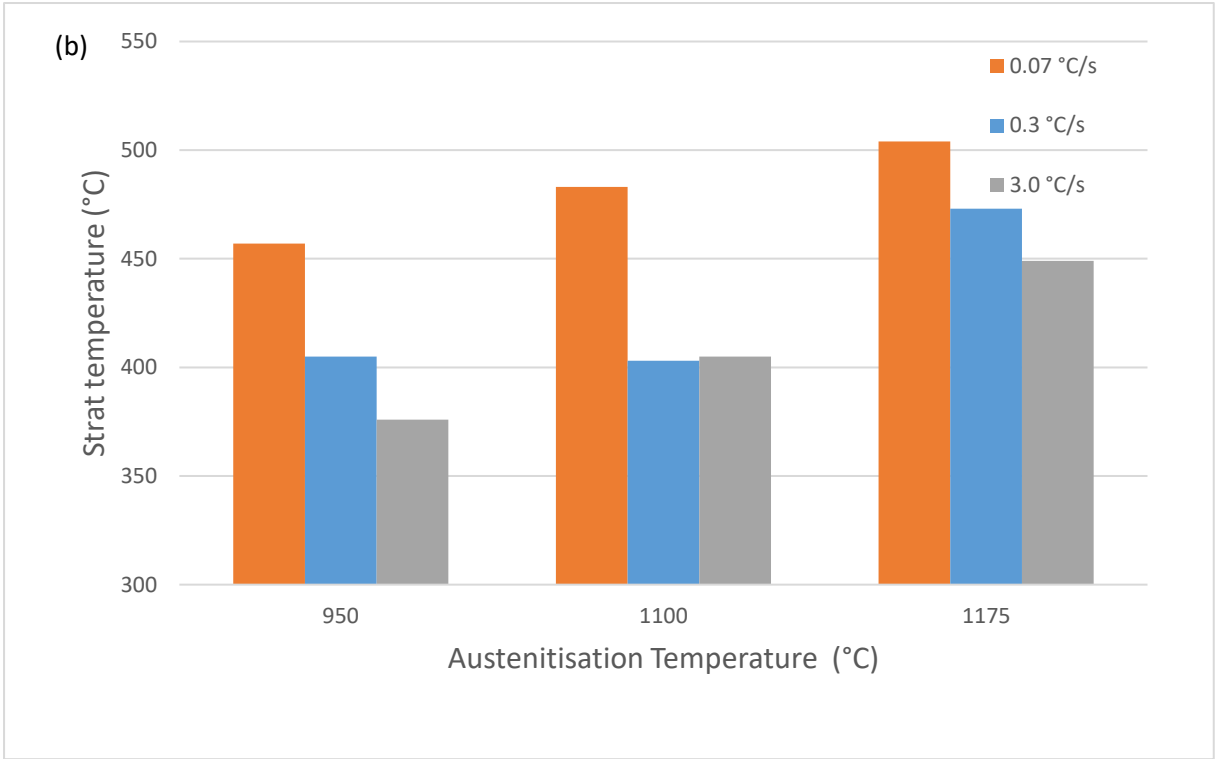

Figure 4-12 Variation of transformation temperatures Vs. (a) cooling rate at 0.07 °C/s, 0.3 °C/s and 3 °C/s, (b)austenitisation temperature of 950°C, 1100 °C and 1175 °C.

Table 4-4 Carbide length, lath width and block size against different PAGS and cooling rates, 95% confidence interval between the bracket.

Austenitisation temp (°C/s)/ **cooling rate (°C/s)**	Carbide (nm)	Lath (nm)	Block (μm)
950/**(0.07)**	280 **(±13)**	478 **(±23)**	9 **(±1.1)**
950/**(0.3)**	147 **(±9)**	343 **(±22)**	6 **(±1)**
950/**(3.0)**	122 **(±7)**	297 **(±23)**	5 **(±0.6)**
1100/**(0.07)**	187 **(±15)**	426 **(±29)**	19 **(±1.2)**
1100/**(0.3)**	182 **(±6)**	548 **(±22)**	25 **(±2)**
1100/**(3.0)**	98 **(±30)**	331 **(±138)**	14 **(±8)**
1175/**(0.07)**	282 **(±29)**	366 **(±32)**	20 **(±4)**
1175/**(0.3)**	197 **(±12)**	568 **(±26)**	31**(±6.9)**
1175/**(3.0)**	162 **(±11)**	480 **(±26)**	23 **(±4.6)**

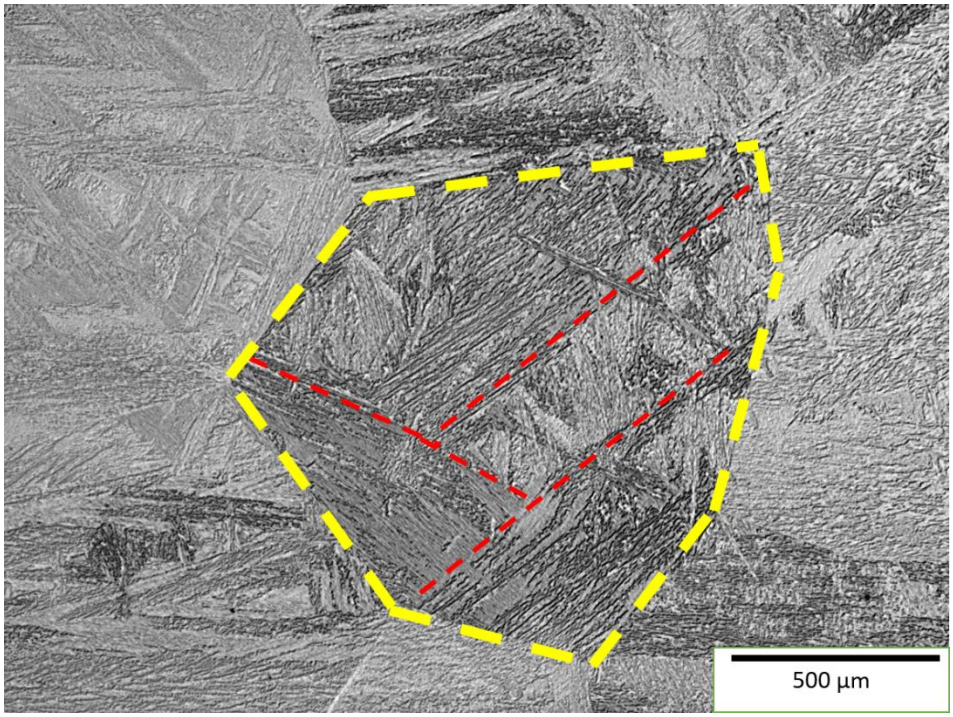

Figure 4-13 Coarse PAGS has more than one block (yellow) is PAGBs and (red) is block boundaries.

4.6 Variation of Microstructure Evolution with Finer PAGS (23 µm) Different Cooling Rates

It can be seen that in Figure 4-14 the finer lath has just one line of long rod shape carbides within the lath all lying in same direction at an angle of around 53-62° [117]. On the other hand, the coarse laths have more than one line of carbides, again that are rode like-shape, but they appear to have a thicker width in comparison to the finer lath carbides, Figure 4-14.

The reason for the observation above is that the coarse lath forms early in the transformation, while the finer lath nucleate at a lower temperature, so the coarse laths enable longer time for carbides to nucleate and coarsen. Moreover, coarse laths have a lower dislocation density and a higher chance of auto tempering because of longer transformation time, leading to a reduction in strength but an increase in toughness [87]. This microstructure could be interpreted as either lower bainite or tempered martensite, however, it is most probably lower bainite. In the case of lower bainite, carbides are aligned in the same direction within the lath, while tempered martensite carbides tend to precipitate within the lath with multiple orientations and a previous studied reported similar observation [56].

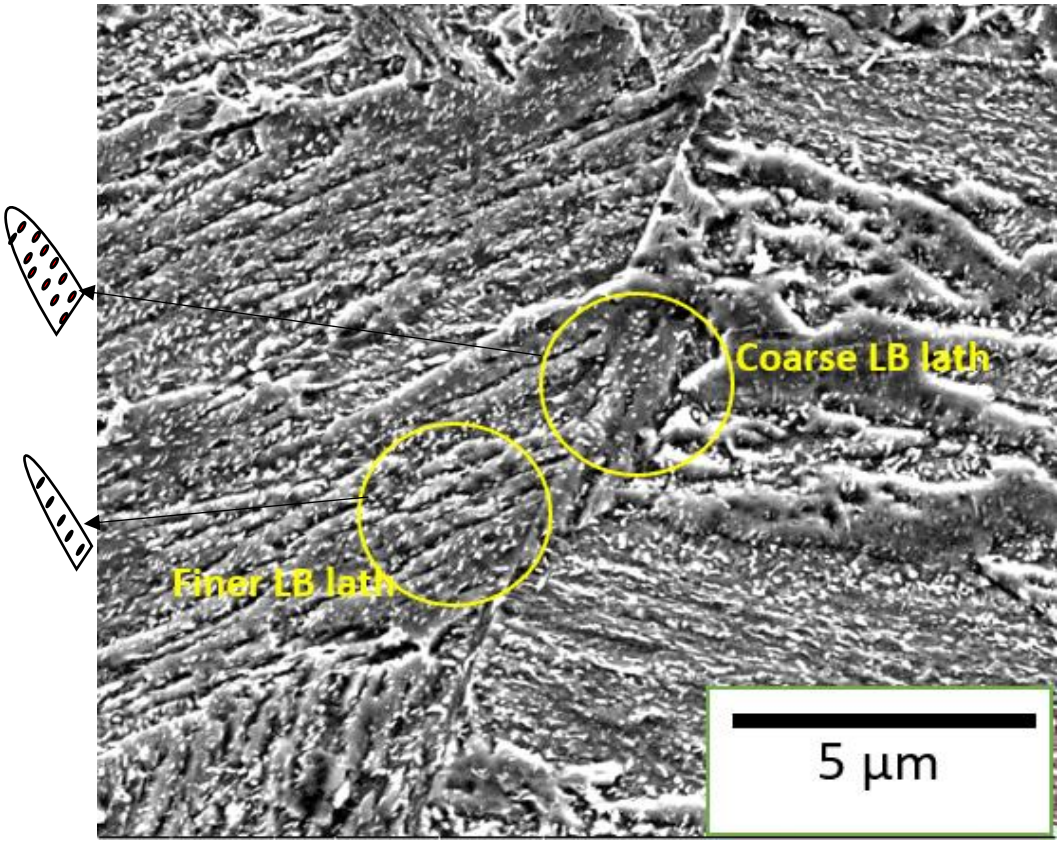

Figure 4-14 Finer lath with one line of carbide and coarse lath with more than one line.

4.6.1 Microstructure Evolution with Finer PAGS 23 µm with Variation Cooling Rates of 0.07, 0.3 and 3 °C/s

Figure 4-15 shows the micrograph of SA508 G4N steels at a cooling rate of 0.07 °C/s and 0.3 °C/s and 3 °C/s with finer PAGS (23µm). Lower bainite (LB) (yellow) with the bainitic laths containing intra lath needle-like carbides is the predominant microstructure at the lower cooling rate of 0.07 °C/s, tempered martensite (green) can also be clearly observed but with lower volume fraction. A combination of lower bainite and martensite (red) dominates at 0.3 °C/s and at cooling rate of 3.0 °C/s, martensite with a lath morphology is dominate. On the other hand, the dominate microstructure with cooling rate of 0.07 °C/s is lower bainite.

4.6.2 Optical Microscope

The dominate morphology of specimens when austenitisation temperature at 950 °C for 5 hours and then cooled at a rate of 0.07 °C/s is lower bainite. OM microstructure of the as-cooled specimen at 0.07 °C/s with a PAGS around 23 µm is shown in Figure 4-15a. However, etching the specimen with a Nital solution makes some areas light, whereas other areas are dark. The dark area could indicate tempered martensite (green) microstructure, which has more carbon content, while the light areas are most likely a bainitic phase (yellow). Martensitic morphology

is highly sensitive to Nital etching [26]. On the other hand, Figure 4-15g is mostly dark as a result of martensite dominating at the fastest cooling rate of 3 °C/s. Martensite morphology is recognized because it has a rough appearance in optical microscope and a previous studied have reported similar observation [26].

4.6.3 SEM

Distinguishing between lower bainite, tempered martensite or martensite is not easy when employing the optical microscope since bainitic lath width is about the 0.02 µm since OM has limited feature to detect the finer lath. Also, there is a carbide precipitation within lower bainite lath (coarse needle with uniform distribution direction) and tempered martensite (fine needle with non-uniform direction) [100]. SEM micrographs of the as-cooled specimens at 0.07 °C/s at a PAGS around 23 µm is shown in Figure 4-15b, c. The predominant microstructure is lower bainite (yellow) and it has lath bainite containing intra lath needle carbides of uniform direction (carbide perception angle around °55). There are also a few equiaxed inter lath carbides, Figure 4-15b, c. In addition, there is some tempered martensite (green) detected with finer laths and needle-like carbides with non-uniform direction at the cooling rate of 0.07 °C/s. However, it is not easy to recognise a martensite microstructure with this slower cooling rate. During the formation of martensite most of the carbon is supersaturated to residual austenite. On the other hand, in case of the lower bainite that has lower carbon partitioned in the residual austenite, so the rest of carbon precipitate as a carbide inside lath with uniform orientation [118]. As can be seen in Figure 4-15b, bainitic lath is formed with some curvature, while the matristic lath is typically straight, Figure 4-15e, h [87]. This estimation is in good harmonization with previous research investigation on SA508 G4N microstructure [39]. Carbides in both martensite and bainite were identified as Cr-rich carbide such as M_7C_3 or $M_{23}MC_6$ carbides [52]. However, Yang [39] found that the carbide in SA508 G4N is just $M_{23}MC_6$ and proposed that the carbide morphology varied, but the carbide types did not changed with changing the cooling rates [39].

On the other hand, SEM micrograph of as-cooled specimen at 0.3 °C/s at a PAGS around 23 µm is represented at Figure 4-15e, f. The predominant microstructure is lath martensite plus a smaller amount of lower bainite. Lower bainite has sheaves with lath bainite, again containing intra lath needle shape carbides with uniform direction and a few equiaxed inter lath carbides Figure 4-15c [42]. The martensite microstructure is dominated due to an increase in the cooling rate that enhances the formation of martensite instead of lower bainite.

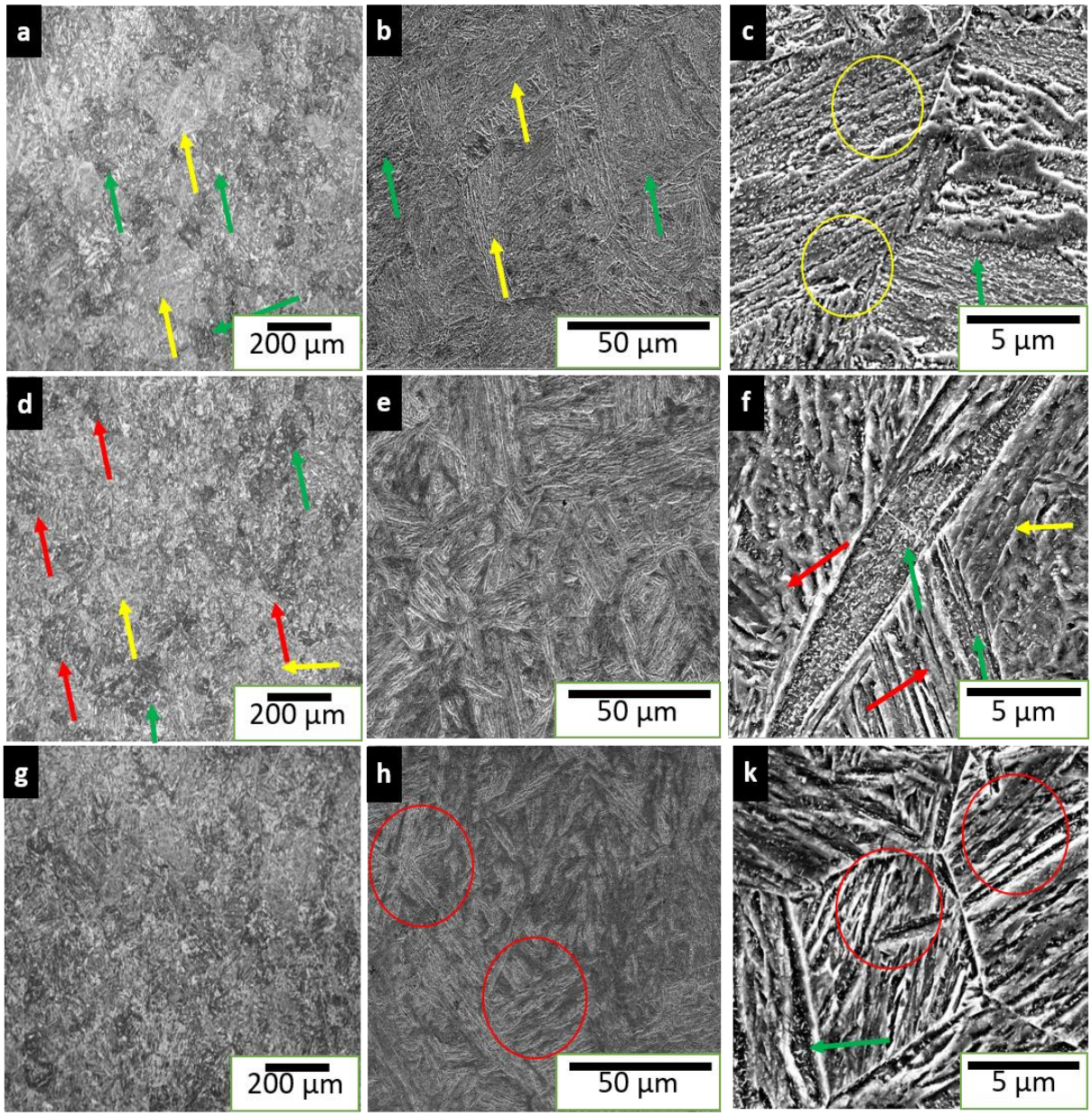

Figure 4-15 (a,d,g) Optical microscope(b, c, e, f, h, k) SEM, (a, b, c) lower bainite at cooling rate of 0.07 °C/s, (d,e,f) mixture bainite and tempered martensite at cooling rate of 0.3 °C/s and (g, h, k) martensite at cooling rate 3.0°C/s. Rad arrow and circle are martensite, green arrow and circle is tempered martensite and yellow is lower bainite.

Typical micrographs of as-cooled specimens at 3 °C/s at PAGS around 23 µm are shown in Figure 4-15h, k. The predominant microstructure is martensite with both packet lath martensite and tempered martensite with intra carbide with random direction visible, while lower bainite cannot be observed with this cooling rate. The martensite laths are finer in comparison to the lower cooling rates of 0.07 °C/s and 0.3 °C/s being 478.1 nm, 343 nm and 279 nm, respectively, Table 4-4. In addition, the martensite laths have finer average carbide size at finer PAGS at

cooling rates 0.07 °C/s, 0.3 °C/s and 3.0 °C/s that are 280 nm, 147 nm and 122 nm, respectively. It can be seen that carbide precipitates at the lath boundaries for fresh martensite, while tempered martensite has intra lath carbides orientated in multiple directions and a previous studied have reported similar observation [100], [119].

Most of the tempered martensite carbides are located at lath boundaries, as a result of the difficulty for carbides to precipitate inside the lath since there is not enough time for precipitation. In general, martensite laths have a low-energy dislocation structure, thus normally the carbide forms first at the lath boundaries, which have higher energy [57]. However, it is worth pointing out that Pallaspuro [100] found weakly visible carbides in a martensitic microstructure of an as-quench HSLA steel. This is similar to the current observations where there is clear needle-like intra lath carbides in the tempered martensitic morphology, which are significantly finer that the carbides at the lath boundaries., i.e., most of inter lath carbides are equiaxed and relatively coarse in comparison to intra lath carbides. However, fewer rod-like carbides are found at the PAGBs or sub-structure boundaries.

4.7 Effect of Variation of PAGS Against One Cooling Rate at as-cooled Sample

4.7.1 Variation of PAGS vs. Slower Cooling Rate of 0.07 °C/s

At finer PAGS at cooling rate of 0.07 °C/s, lower bainite is the dominate microstructure with carbides precipitated intra lath that have a needle-like shape and uniform direction. There are also few equiaxed carbides inter lath. However, granular bainite is the predominate microstructure at intermediate and coarse PAGS at cooling rate of 0.07 °C/s, Figure 4-17.

Bainite formation exists at a finer PAGS with cooling rate of 0.07 °C/s when laths of bainite nucleate by the same mechanism as martensite, however at a relatively higher transformation temperature. In addition, bainite can occur when austenite is weak and cannot elastically support large deformations. Moreover, the enriched austenite with carbon partitions into the residual austenite and carbon precipitates from the austenite. Bainite sheaves grow to a limited size as a result of incomplete transformation that limits its size and becomes smaller than the PAGS [33].

At intermediate PAGS (84 µm), the predominant microstructure is Granular Bainite (GB), with some lower bainite and tempered martensite, which is comparable to the results of Yang Figure 2-7 [39] but with an austenitisation temperature at 860 °C for 5 hours. Moreover, microstructure that typically consists of MA islands surrounded by a bainitic ferrite matrix Figure 4-17c, e. Micro hardness has conducted to MA island and bainitic ferrite matrix and it

concludes that MA island has higher hardness more than twice by comparison to the bainitic ferrite matrix. This result is comparable with Huda assumption [9]. In addition, increasing PAGS facilitates the formation of granular bainite instead of lower bainite as a result of increasing the transformation temperature allowing more time for granular bainite to form. Moreover, it is more probable to find the granular bainite with coarse PAGS at higher temperature because some alloy elements stabilize the austenite owing to the rapid redistribution of alloying elements [37]. Moreover, carbon enhances the formation of MA islands at higher transformation temperature by decreasing the driving force for the transformation of austenite to martensite. It has been suggested that untransformed austenite, as a result of increased alloying element content, retards carbon diffusion and it becomes enriched with carbon. This leads to a decrease in the transformation driving force, leading to incomplete bainite transformation, enhancing MA formation at higher transformation temperature [37]. Moreover, Huda [9] proposed that when the austenitising temperature is higher than Ac3, austenite forms at PAGBs due to higher carbon content. However, the bainitic ferrite grows in lower carbon volume fraction area, while the MA nucleates at high carbon austenite region which is dependent on the carbon diffusion time [9].

The formation of Martensite Austenite Island (MA) depends on the formation of carbide free bainite and MA island volume fraction increases as the micro allaying elements increase. Incomplete bainite formation can be achieved as a result of alloying elements and this hinders the bainite transformation and it was suggested that this observation helps MA formation [37]. Coarse PAGS have coarser laths of bainite and it promotes MA nucleation due to higher alloying elements that delays the untransformed austenite between the bainitic ferrite. This observation induces the coarse bainite to form at a higher bainite transformation temperature leading to untransformed austenite between the coarse lathed bainite packets. On the other hand, the untransformed austenite within PAGS transforms at lower temperature than the global martensite start transformation temperature [37]. MA islands can thus be observed in the bainitic morphology rather than in martensitic microstructure due to most of the carbon being consumed by MA island. Thus, carbon partitions to MA island, while martensite needs high carbon contents [33].

Fine carbide precipitated within lath tempered martensite with non-uniform direction, but carbide cannot be found within MA because most of carbon is in solution to form MA [39]. So, there is not any chance for carbide to precipitate when MA island forms. MA islands in granular bainite are generally recognized to have two types of morphology: blocky and rod shape [37].

The blocky MA island is more obvious near PAGBs and mostly at triple junction boundaries due to their higher energy, Figure 4-17c. Whereas, the needle like shaped MA normally exists between bainite packets [36]. In addition, the blocky MA form at the onset of transformation and its shape depends on the bainitic ferrite surrounded MA, so the bainitic ferrite around the MA play a role to determine the MA shape is blocky or needle [37], [39]. The blocky MA island nucleates due to carbon partitioning during the bainitic transformation and, then it segregates along PAGBs and more often with triple junction [36]. Thus, PAGS has an impact in determining the type of MA formed, as increased PAGS increases the opportunity for blocky MA to form. Figure 4-16 shows the blocky and needle-like shapes MA island with high magnification. Also, increasing PAGS leads to a rise in the transformation temperature and this enhances the likelihood of Granular bainite and tempered martensite formation, so the volume fraction of granular bainite increases, while the volume fraction of lower bainite and martensite decreases. Table 4-3 shows the transformation start temperature and it indicates that the formation temperatures are 445 °C, 483 °C and 504 °C for finer, intermediate and coarse PAGS, respectively. Moreover, higher transformation temperature assists the tempered martensite nucleation, thus leading to an increase in the volume fraction of tempered martensite when the transformation temperature increases [120]. In addition, volume fraction of tempered martensite is increased with coarse PAGS in contrast to finer and intermediate PAGS, thus increasing PAGS leads to an increase in the tempered martensite volume fraction [120].

Table 4-4 shows bainite lath sizes of 478 µm, 426 µm and 366 µm for PAGS of 23 µm, 84 µm and 412 µm, respectively, for the 0.07 °C/s, and the most interesting feature is that coarse PAGS leads to a decrease in lath size. It is also noteworthy that the smallest PAGS generated the coarsest bainite laths. This is most likely attributably to the higher transformation start temperature enhancing the rate of carbon diffusion ahead of the transformation front. This then leads to greater portioning of carbon into the austenite, eventually leading to stabilised austenite and subsequent transformation to MA.

Increasing PAGS leads to a decrease in grain boundary area and it makes C-curves of CCT diagram moves to the right and difficult to start ferrite formation and martensite could form at lower cooling rate. So, it is more possibility for bainite to nucleate and grow. Decrease PAGS leads to increase the PAGBs and this increases the nucleation density and can decreases bainite formation when it nucleates at the grain boundaries as a result of decreasing the diving force [50].

Very slow cooling rate and high self-tempering temperature enhances granular bainite formation. Granular bainite reduces the steel toughness as a result of strain incompatibility between the MA and the surrounding matrix during the transformation [121]. In addition, inhomogeneity between the MA and surrounded bainitic ferrite matrix leads to large difference in plastic deformation and this leads to initiation cracks in the MA [9]. In most cases, MA is enriched with carbon at the edges of MA [36].

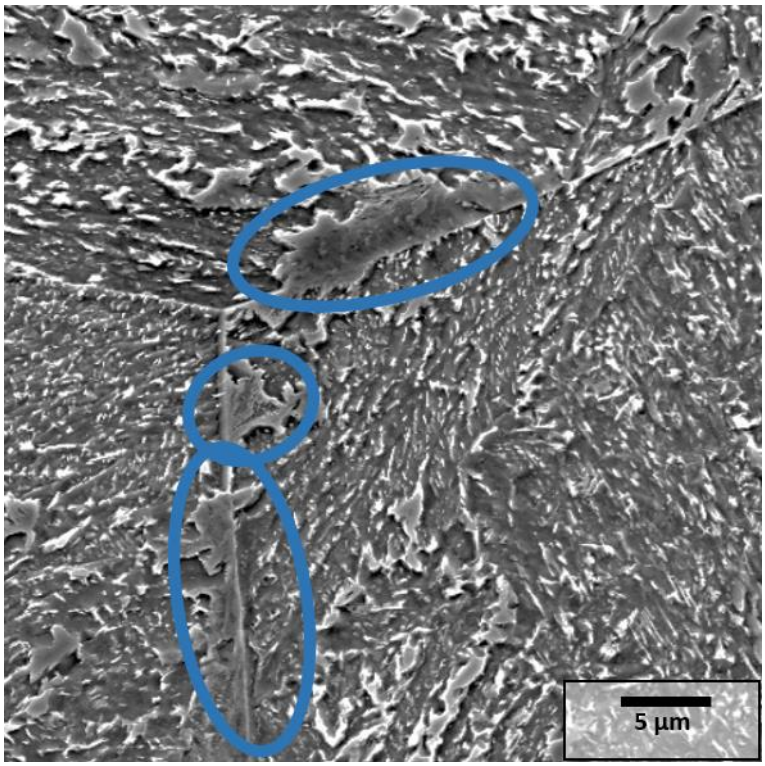

Figure 4-16 SEM micrograph shows granular bainite and martensite austenite island.

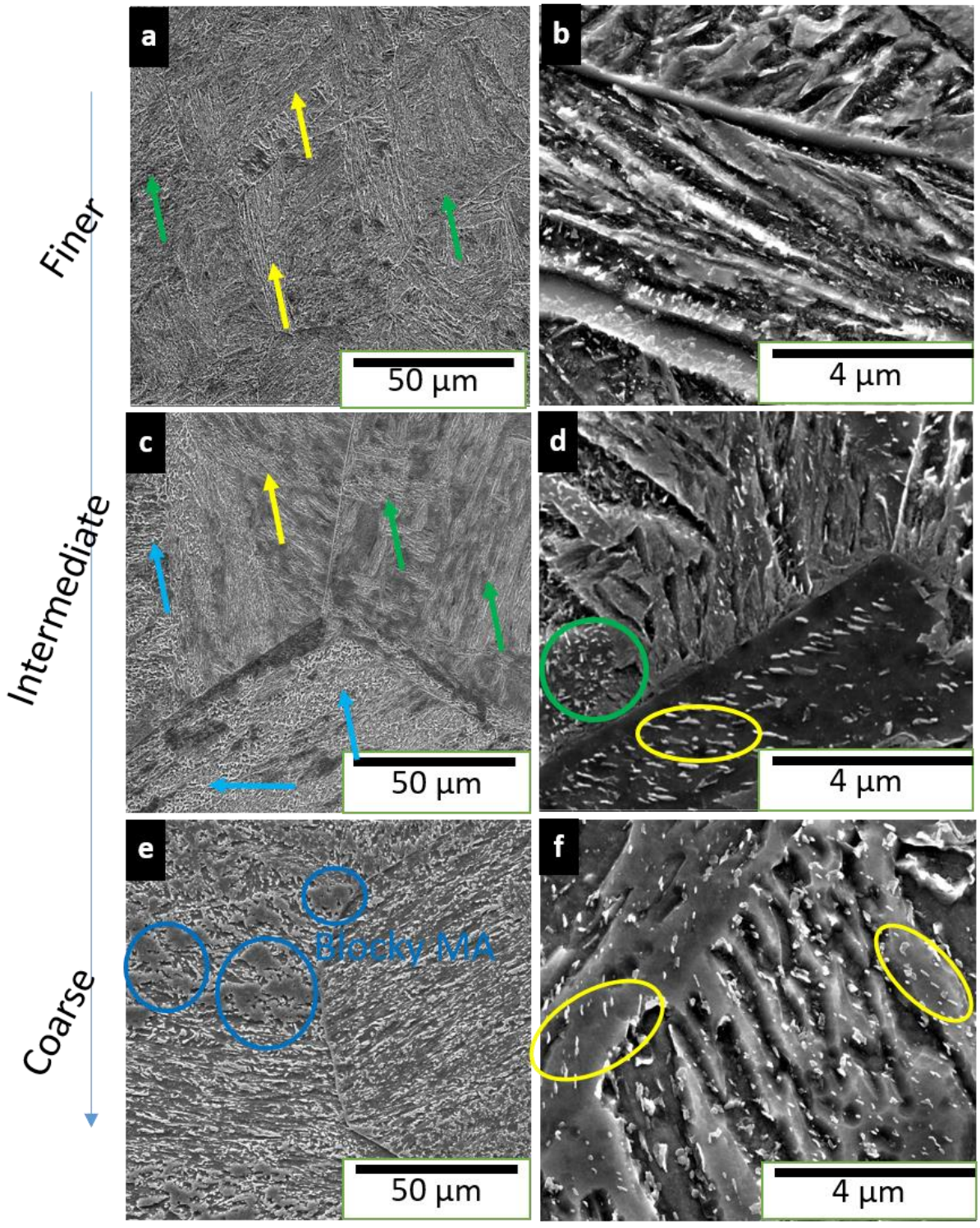

Figure 4-17 Micrograph of cooling rate at 0.07 °C/s with different PAGS, (a,b) is finer, (c,d) is intermediate and coarse is (e,f), yellow circle and arrow is lower bainite, green is tempered martensite, blue circle is blocky MA, and blue arrow is granular bainite.

4.7.2 Variation of PAGS with cooling rate of 0.3 °C/s

The most predominant microstructure of as-cooled SA508 G4N at cooling rate of 0.3 °C/s is martensite and lower bainite, whilst there is no indication of granular bainite. Figure 4-18 represents the microstructure of SA508 G4N as cooled steel at cooling rate 0.3 °C/s with different PAGS. Figure 4-18a, b shows the steel at cooling rate of 0.3 °C/s and with finer PAGS, Figure 4-18c, d represents intermediate PAGS and coarse PAGS is represented by Figure 4-18e, f. Increasing PAGS leads to a decrease in martensite volume fraction, and subsequent increase in lower bainite and tempered martensite. The resulting micrographs and hardness data support this observation. Increasing transformation temperature leads to an increase in the tempered martensite density as a result of increasing the auto tempering time of martensite [100]. Also, the transformation temperature increases 405, 403 and 473 °C as PAGS increase 23, 84 and over 412 µm. However, a slight decrease in the transformation temperature between the finer and intermediate PAGS and a rapid increase in transformation temperature with a coarse PAGS when cooling rate is 0.3 °C/s is observed.

Equiaxed like-shape carbide is detected in the lower bainite with different PAGS. While, it is hard to find carbide precipitation within the martensitic microstructure since carbon first precipitates in the lower bainite instead of martensite. Table 4-4 provides the average carbide, lath and block sizes as a function of PAGS. It is obvious the average carbide, and block increases as PAGS coarsen, for instance block size is about 6 µm with a finer PAGS and rapidly increases with intermediate PAGS to about 25 µm and then a slightly increases to around 31.0 µm at the largest PAGS, similar to the behaviour observed for the carbides.

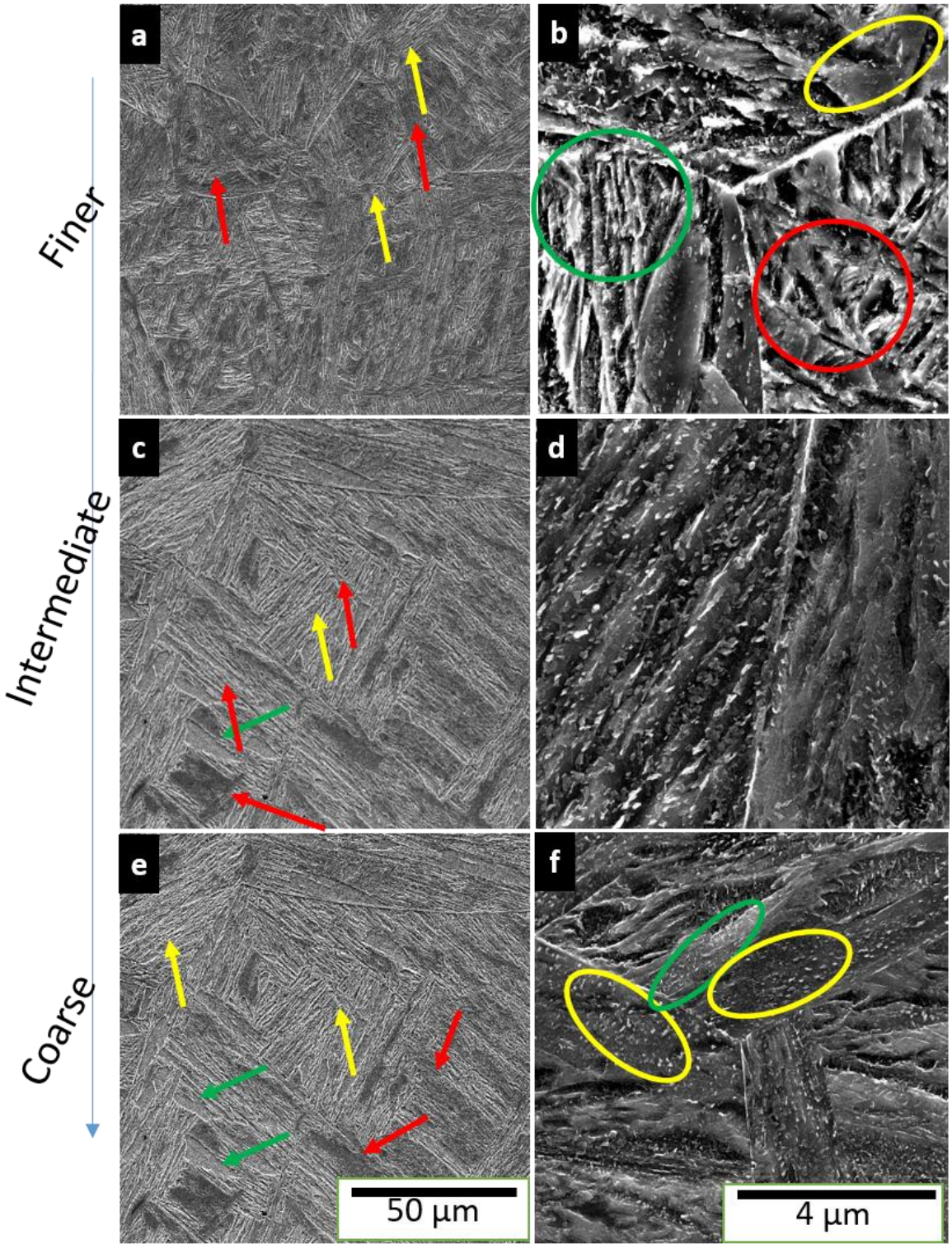

Figure 4-18 Micrograph of cooling rate at 0.3 °C/s with different PAGS, (a,b) is finer, (c,d) is intermediate and coarse is (e,f), yellow arrow is bainite, red is martensite, green is coarse carbide white is fine carbide.

4.7.3 Variation of PAGS vs. Fastest Cooling Rate at 3 °C/s

SEM micrographs of as-cooled specimens at 3 °C/s with variation of PAGS finer, intermediate and coarse 23 µm, 80 µm and 412 µm are presented in Figure 4-19. The predominant

microstructure is martensite with packet lath martensite and tempered martensite with inter carbide precipitated in random directions. Martensite lath size is the finest in comparison to other cooling rates of 0.07, and 0.3 °C/s and the lath thickness are 478 nm, 343 nm, 279 nm, respectively, Table 4-4. Furthermore, lath thickness of bainite is almost double in comparison to the martensite laths. In addition, the tempered martensite laths have the finest carbide sizes that are 122 nm, 147 nm and 280 nm, respectively, in comparison to other cooling rates. At the highest cooling rate, carbide size is finer due to the short time for carbon diffusion or redistribution [100]. In addition, lath length does not change a lot since lath favour to increase width instead of lath length as lath width is very sensitive to temperature and this is not a case with lath length [116]. Also, coarse lath starts to form in the first stage of martensite formation while finer laths form near the end of transformation, thus coarse carbide continue to grow from the outset of transformation, while finer carbide just form near the end of transformation and thus have no time to grow [72], [87]. It can be seen that carbide precipitates at the lath boundary for fresh martensite [100], [119], while tempered martensite has a different direction carbide precipitation within the lath [100]. Under normal conditions during quenching, lath martensite occurs after quenching stage and it can follow by auto-tempering as a result of low carbon and alloy elements contents with higher martensite start temperature [65].

In general, with different PAGS, martensite is the dominate microstructure. While, tempered martensite with random direction carbides precipitated intra lath with needle-like shape is also present in low volume fraction in addition to a few equiaxed carbides between laths and this consistent with Yang [39] observation. Volume fraction of tempered martensite increases as the PAGS rises as a result of increasing Ms, which provides longer time for auto martensite tempering [100]. Also, carbide and block sizes increase as PAGS increases Table 4-4 [100]. The dislocation density in martensite phase decreases due to enough time for recovery of dislocations as a result of the extended period of transformation as PAGS increases [100]. By contrast, finer PAGS decreases Ms and this reduced time for lath growth suppresses the reduction of dislocation density as there is not enough time to recover, making a higher dislocation density. Finer martensite lath form at lower transformation temperature (later stage) [72]. Finer PAGS leads to decrease Ms temperature and this consequently decreases the tempered martensite volume fraction because of the time for auto martensite tempering is not adequate [100].

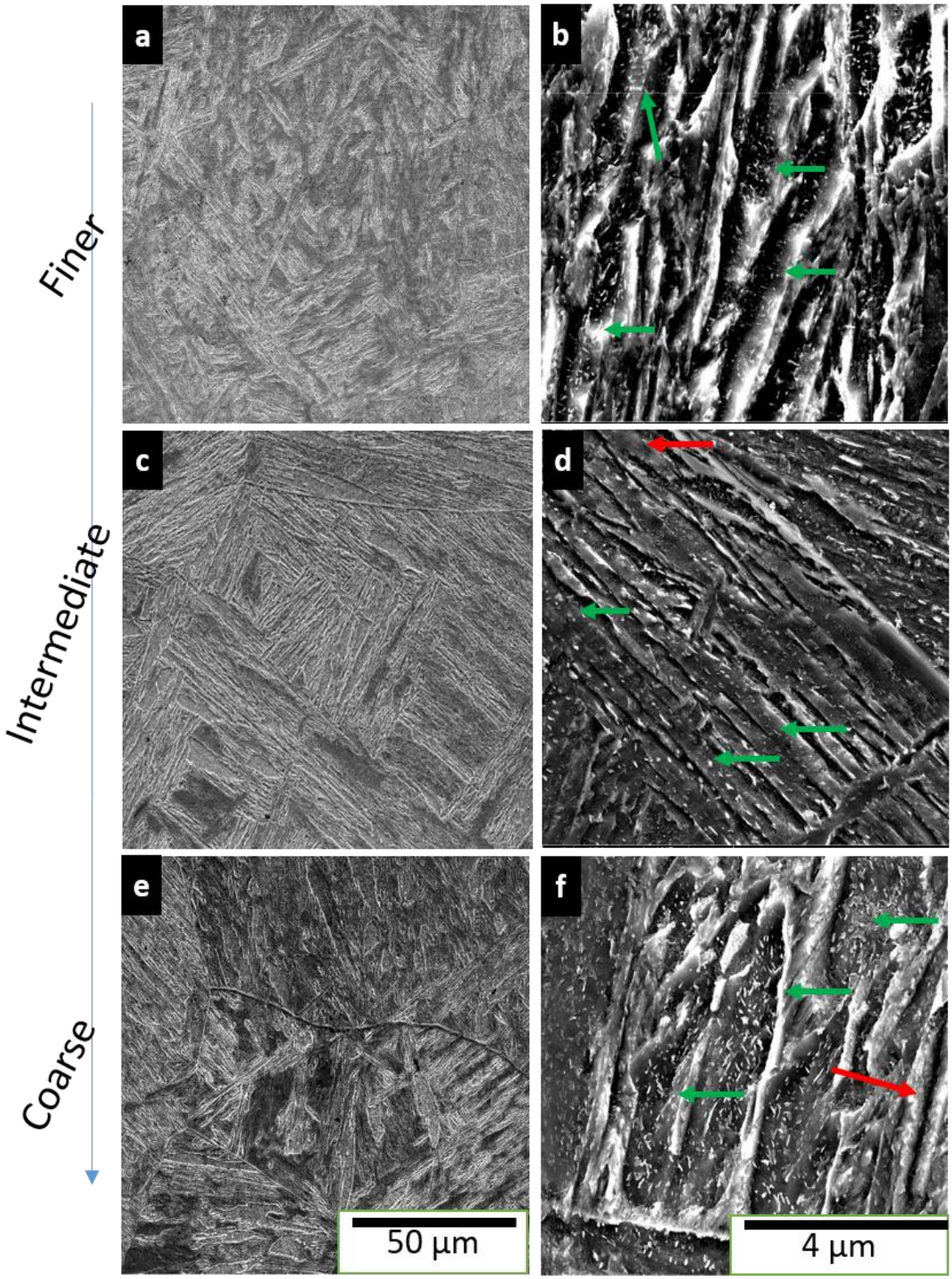

Figure 4-19 Micrograph of cooling rate at 3.0 °C/s with different PAGS, (a,b) is finer, (c,d) is intermediate and coarse is (e,f), green arrow is tempered martensite, red is martensite.

4.8 Summary

This chapter described the impact of PAGS on transformation start temperature, microstructure, and carbide and lath size in SA508 G4N as a function of cooling rate. Increasing PAGS rises the transformation start temperature, which then directly impacts carbide growth, and bainite and martensite lath coarsening. At a cooling rate of 0.07 °C/s, lower bainite is the most dominate morphology at finer PAGS. However, at large PAGS, granular bainite forms instead of lower bainite, with increasing PAGS leading to a decrease in the average bainite lath width. At a cooling rate of 3.0 °C/s, increasing PAGS leads to increase in martensite lath width and tempered martensite volume fraction due to having a higher transformation temperature.

5 Result and Discussion

5.1 Chapter Overview

This chapter describes the results and analysis of the effects of PAGS on the microstructure evolution as a function of tempering conditions. Also, a detailed analysis of the evolution of carbide size and carbide growth as a function of tempering conditions and variation of PAGS is given. This is then followed by a small section on the effect of these microstructures on hardness.

5.2 Effect of Tempering at 550 °C for 6 h and 24 h on SA508 G4N Microstructure

Tempering is the last stage conducted before final machining. In this research two different tempering stages were applied by fixing the tempering temperature at 550 °C and varying the tempering time by 6 hours and 24 hours. There is a shortage of literature studies that consider and discuss the microstructure of SA508 G4N after tempering in either the fully bainitic, fully martensitic or mixture of martensite and bainite conditions. In tempering of martensite the supersaturated carbon atoms diffuse to lower energy conditions, firstly gathering in clusters and eventually precipitating out as carbides [117], [119]. Tempering, in general textbook terms, improves the ductility of the material by decreasing the carbon supersaturation in the martensite. However, tempering is much more complicated in steels like SA508 G4N, influencing microstructure features such as carbon segregation, precipitation of transition carbides, retained austenite decomposition, coarsening of bainite, carbide precipitation and carbide coarsening [70]. Table 5-1 shows the carbide and lath sizes after tempering for 6 H and 24 H. In general trend after tempering, the average lath and carbide sizes increase as tempering time raises.

5.2.1 Microstructure Variation of SA508 G4N at Finer PAGS at Cooling of Rate 0.07 °C/s with Tempering 550 °C for 6 h and 24 h

Evolution of microstructure during the different tempering stages appears to have three different facets: carbide precipitation, carbide growth for both inter and intra lath carbides and lath growth. Figure 5-1 characterises the microstructure of SA508 G4N steel at the finer PAGS and cooling rate of 0.07 °C/s, tempered at 550 °C for 6 h and 24 h.

Table 5-1 Carbide and lath sizes against different PAGS and cooling rates after tempering at 550 °C for 6 H and 24 H, (95% confidence interval between the bracket).

Austenitisation temp (°C/s)/ **cooling rate (°C/s)**	Tempering for 6 H		Tempering for 24 H	
	Carbide (nm)	Lath (nm)	Carbide (nm)	Lath (nm)
950/**(0.07)**	351 (±14)	612 (±30)	396 (±11)	741(±83)
950/**(0.3)**	217 (±9)	435 (±11)	269 (±13)	509 (±39)
950/**(3.0)**	151 (±4)	369 (±16)	192 (±8)	451(±35)
1100/**(0.07)**	230 (±15)	521 (±44)	291 (±23)	610 (±51)
1100/**(0.3)**	239 (±17)	646 (±46)	280 (±8)	701 (±39)
1100/**(3.0)**	130 (±4)	429 (±17)	162 (±6)	596 (±21)
1175/**(0.07)**	345 (±22)	432 (±19)	331 (±29)	526 (±17)
1175/**(0.3)**	249 (±9)	659 (±37)	291 (±11)	728 (±55)
1175/**(3.0)**	203 (±9)	612 (±27)	254 (±34)	764 (±75)

Figure 5-1a, b shows a noticeable needle-like shape intra bainite lath carbide and a coarse equiaxed inter bainite lath carbide with an average carbide size of 280 nm. Lath width increases around 28 % as a result of tempering for 6 h, with some laths having merged together to become coarser laths, consistent with observations by Lan [120]. Moreover, some of the lath boundaries have become curved as reported by Li [75] in bainite morphology.

The carbides within the coarse bainitic laths have also coarsened at a much faster rate than the carbides within the finer laths, Figure 5-1b. On the other hand, after 6 h tempering at 550 °C many of the inter lath carbides have increased slightly in size about 25 % and have become more equiaxed and the size increases around 9%, Table 5-1. The volume fraction of the carbides does change but the number density has decreased, suggesting that the finer carbide is consumed by the coarse carbide, which continues to grow, Figure 5-1c, d. A similar story also exists for the intra lath carbides, where there is coarsening of the larger particles, which

become equiaxed and the number density decreases. Again, the main reason being, the fine intra lath carbides decompose and diffuse to enhance growth of the coarser carbides. The fact that both the intra and inter lath carbides have similar volume fractions before and after tempering suggests that there is limited carbon diffusion between the two forms of carbide, suggesting distinct chemistries of the two types of carbides Table 5-1.

For 24 h tempering, the vast majority of carbides have become equiaxed with a larger size (396 nm). However, there are some needle-like carbides that remain, suggesting they are chemically or mechanically stabilised [122]. Furthermore, there are clusters of carbides at triple junction boundaries suggesting segregation of supersaturated carbon atoms at these locations [121]. The clusters of carbides that can be observed at triple junction boundaries suggests there was significant levels of supersaturated carbon atoms in triple junctions [121]. It is well known that the coarsening rate of $M_{23}\,C_6$ type carbides increases with increasing content of Chromium (Cr), which is further enhanced by having Fe or Ni in the carbide [93]. On the other hand, Si stabilizes carbide growth due to low solubility within the carbide [33], suggesting that Si stay in the matrix.

The bainite lath width increases around 55% by comparison to as-cooled sample as the tempering time increases for 24 h as a result of dissolution of the fine carbides at the lath boundaries allowing for enhanced mobility of those boundaries [120]. In addition, the bainitic lath boundaries have increased in curvature, further confirming a higher boundary mobility [75]. Table 5-2 summaries lath growth and carbide precipitation and growth during tempering time for 6 h and 24 h for the sample cooled at 0.07 °C /s with the fine PAGS. Increasing tempering time is clearly promoting bainitic lath growth, making the average lath size coarser. This is most likely because of that fact the tempering stage reduces the pinning force on the lath boundaries, owing to a reduction in carbide density.

In general, as discussed in the previous chapter, coarse laths form at an early stage of the transformation stage and have a lower dislocation density in comparison to the finer laths that nucleate in the later stages of transformation [87]. It is thus interesting to note that there appears to be a higher density of new carbides formed in the finer laths, which most likely is due to the increased level of dislocations in those laths acting as a driving force and nucleation sites for new carbide formation.

Table 5-2 Summaries lath growth, carbide precipitation and growth during the as-cooled tempering time for 6 h and 24 h at sample cooled of 0.07 °C /s with finer PAGS.

0.07 °C /s	As-cooled	Tempering 6 h	Tempering 24 h
Carbide precipitation	Needle-like intra lath, coarse equiaxed inter lath	Finer intra equiaxed and the carbide density declined, coarse inter equiaxed carbide	Equiaxed carbide and cluster
Carbide growth		Inter and intra carbide grow separately about 23%	Carbide size rises more about 12 %
Lath width		Increase by 25 %	Increases more by about 21 %

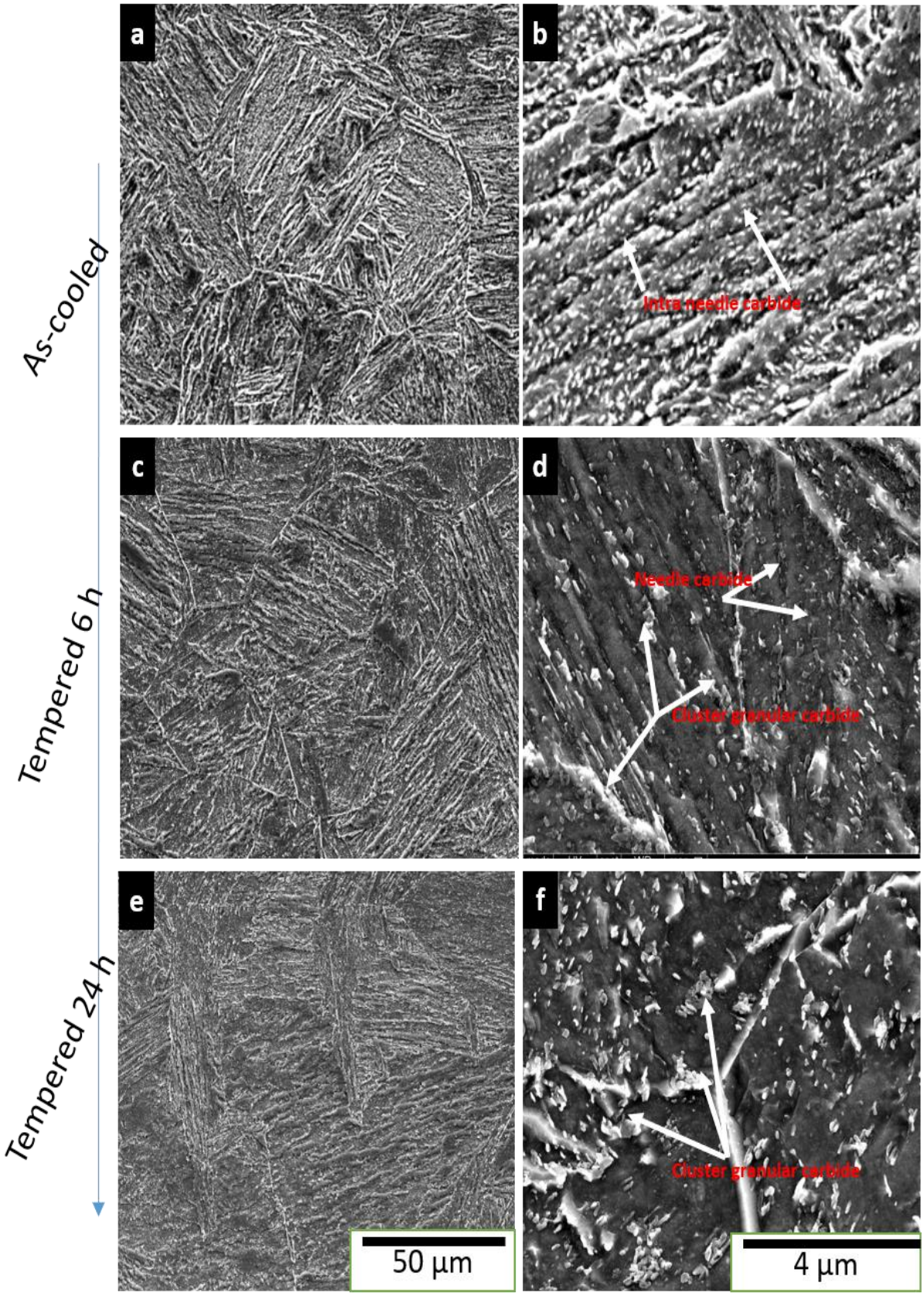

Figure 5-1 Finer PAGS with cooling rate 0.07 °C/s and different tempering time (a, b) as-cooled (c, d) 6h tempering (e, f) 24 h tempering.

5.2.2 Microstructure Variation of SA508 G4N at Intermediate PAGS at Cooling Rate of 0.07 °C/s with Tempering 550 °C for 6 h and 24h

Figure 5-2 shows the microstructure of SA508 G4N steel at intermediate PAGS and cooling rate of 0.07 °C/s, tempered at 550 °C for 6 h and 24 h. Evaluation of this microstructure, which after cooling was predominantly Granular bainite with MA island and lower bainite, following tempering had four motivations: decomposition of Martensite Austenite island (MA), carbide precipitation, carbide growth for inter and intra lath and finally lower bainite lath growth. In general, after tempering, the bainitic lath width increases and there was some level of lath coalescence to form much larger laths. Some of the MA decomposed with tempering time to new form new bainite and fresh carbides, increasing the bainite volume fraction, while other untransformed MA increased in size, Figure 5-2e.

After 6 h tempering, some of the MA decomposed to lower bainite that has a tempered appearance containing coarse equiaxed carbides inside the laths, Figure 5-2c. On the other hand, some MA islands have not decomposed after 6 h tempering and they appear to have increased in size and this result is in harmony with Li result [75]. This may have its origins in the dissolution of carbides enabling further growth of stabilised austenite at the tempering temperature, some of which on cooling transforms to martensite [75]. For the lower bainite, the fine needle like carbides that formed on quenching have now become more equiaxed and larger around 45 % but with reduced number density. However, it should be noted that there is no significant evidence of new carbides in the lower bainite, which could be attributed to the bainite having much lower dislocation density than martensite, thus there is less driving force for nucleation of new carbides.

After tempering for 24 h, carbides within the lower bainite have grown larger about 2 % and have taken on a plate-like morphology, which also appear to gather in clusters, with a significant fraction being at lath boundaries or PAGBs, Figure 5-2f. Also, the lower bainite laths have continued to grow by about 17 %. In terms of the MA, the vast majority has now decomposed to bainite and coarse carbides, on the other hand some of MA island steady and previous studied reported similar observation Figure 5-3 [120], [121]. Table 5-3 summaries lath growth and carbide precipitation and growth during as-cooled tempering time for 6 h and 24 h when sample cooled at 0.07 °C /s with intermediate PAGS.

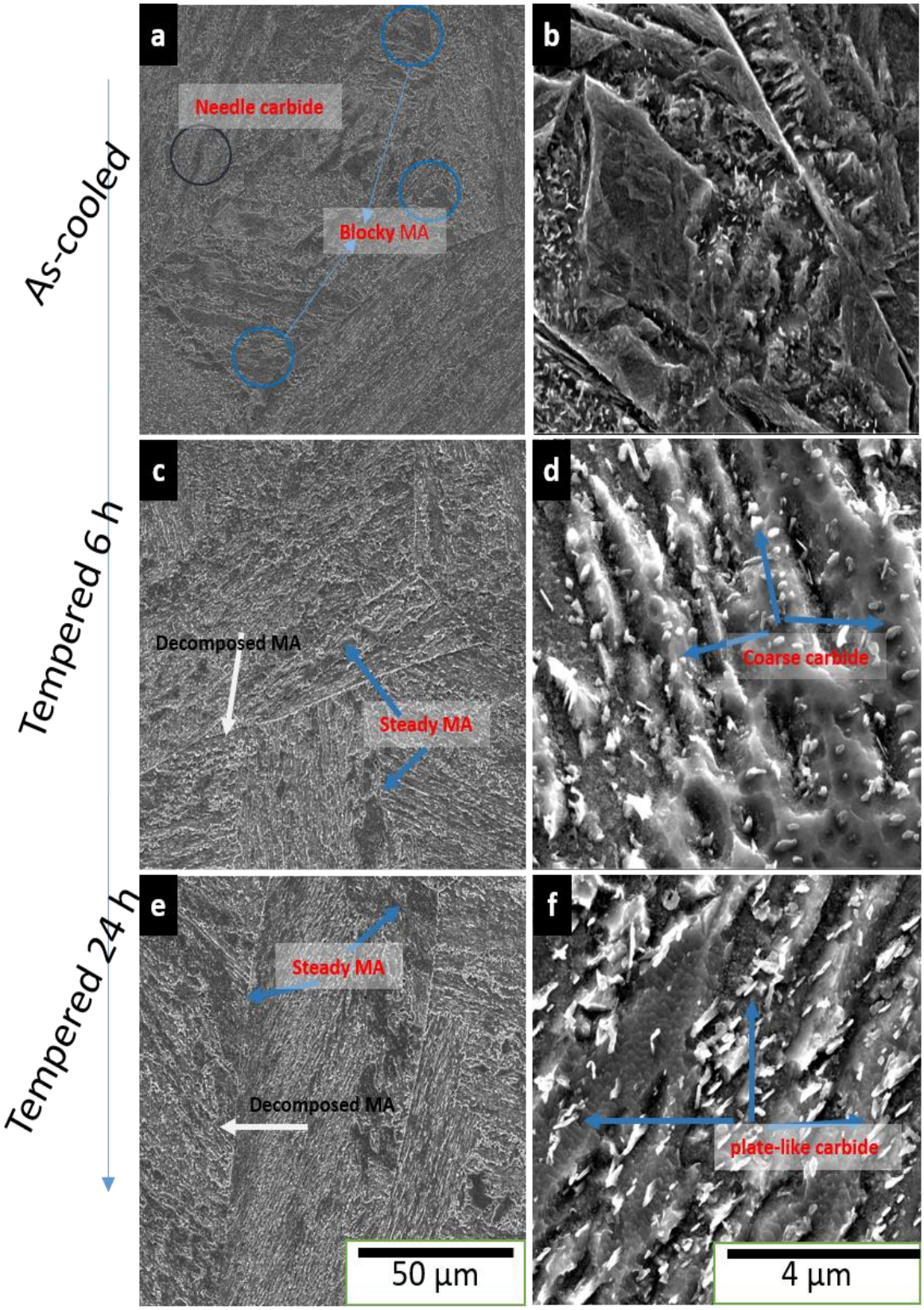

Figure 5-2 Intermediate PAGS with cooling rate of 0.07 °C/s and different tempering at 550 °C for (a) as-cooled (c) 6 h tempering (e)24 h tempering.

Table 5-3 Summaries lath growth, carbide precipitation and growth during the as-cooled tempering time for 6 h and 24 h when sample cooled at 0.07 °C /s with intermediate PAGS.

0.07 °C /s - intermediate	**As-cool**	**Tempering 6 h**	**Tempering 24 h**
Carbide precipitation	needle-like intra lath coarse equiaxed inter	Coarse inter equiaxed carbide by about 47% and volume fraction increases. Intra equiaxed and the carbide density declined.	Inter plate-like carbide but large Carbide size rises by 2%
MA decomposition		MA decomposed to lower bainite and fresh carbide Most of needle-like MA decomposed	More MA decomposed
Lath width		Increase by 22 %	Increases more by 17%

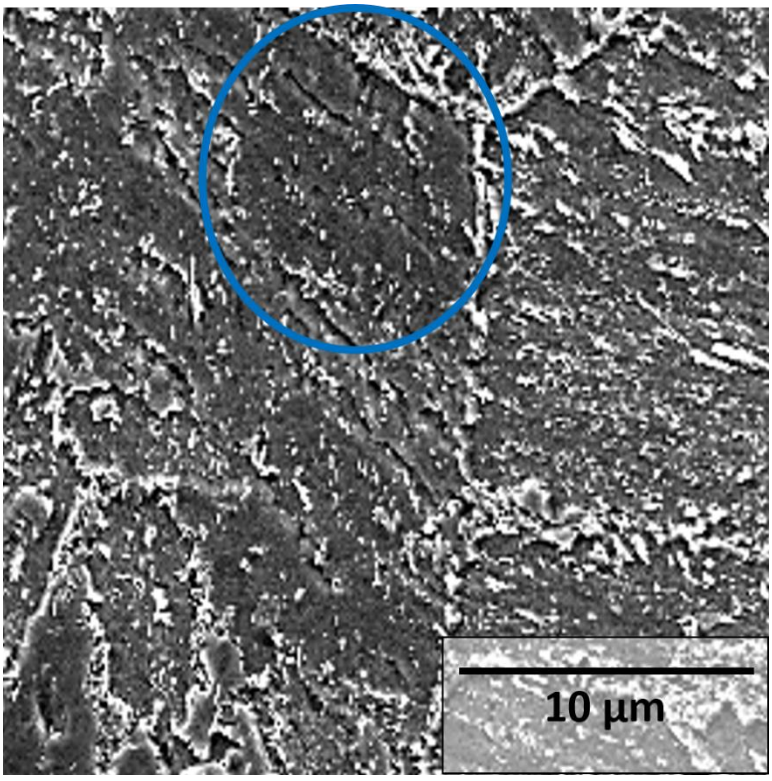

Figure 5-3 Steady MA island with high magnification.

5.2.3 Microstructure Variation of SA508 G4N at Coarse PAGS at Cooling Rate of 0.07 °C/s with Tempering 550 °C for 6 h and 24 h

Figure 5-4 shows the microstructure of SA508 G4N steel at coarse PAGS and cooling rate of 0.07 °C/s, tempered at 550 °C for 6 h and 24 h. The predominant microstructure is tempered granular bainite with MA island and a lower volume fraction of lower bainite. MA island form with two different morphologies blocky and needle-like shape. In spite of the higher transformation temperature that enhance the martensite auto-tempering, it is difficult to identify tempered martensite due to formation and growth of MA islands during the tempering stage [100]. During the tempering stage, the MA islands have decomposed to bainite and precipitation of fresh carbides, increasing the bainite volume fraction, while other untransformed MA size increases as a result of tempering temperature time by consuming the excess redissolved carbon [75]. Clusters of carbides can again be observed at austenite triple junction boundaries, confirming segregation of supersaturated carbon atoms at these locations [121].

Generally speaking, tempering increases lath and remnant MA island sizes, while some of the MA islands decompose to lower bainite and carbide, Figure 5-4e. The stability of the MA appears linked to its morphology, i.e., blocky-like shape is more stable than needle-like MA islands. Understanding and studying the factors that affect the stability of the MA is challenging since different factors have a role such as chemistry and mechanical stabilisation [123]. It is well known that blocky MA islands have higher carbon concentration than needle-like shape, so they are likely to remain stable longer during the tempering stages due to higher carbon content increasing thermodynamic stability. Table 5-4 summaries lath growth and carbide precipitation and growth during as-cooled tempering time for 6 h and 24 h when sample cooled at 0.07 °C/s with coarse PAGS.

After 6 h tempering at 550 °C, the as-quenched intra bainite lath needle-like carbides have grown by about 22% and taken on a more plate-like morphology, however after tempering for 24 h, there appears to be some amount of new fine needle-like carbides, which form in clusters. Moreover, some of the plate-like intra carbide seen at 24 h appear to be reduced in size, Figure 5-4f. It should also be noted that the carbide size is the coarsest in comparison to the faster cooling rates due to an increase the martensite volume fraction that have finer carbides [86].

Table 5-4 Summaries lath growth, carbide precipitation and growth during the as-cooled tempering time for 6 h and 24 h when sample cooled at 0.07 °C /s with coarse PAGS.

0.07 °C /s- coarse PAGS	As-cool 3°C /s	Tempering 6 h	Tempering 24 h
Carbide precipitation	Few inter equiaxed with a fine intra carbide needle uniform direction	Intra plate-like carbide Carbide size increase by 22%	needle-like carbide gathers in cluster, size increase by 13 %
MA decomposition	More blocky and needle fewer than 0.3 °C /s	MA blocky partial decomposed to lower bainite and fresh carbide Needle-like MA not noticeable	More decomposed
Lath width		Increase by about 18 %	Increases more by 13 %

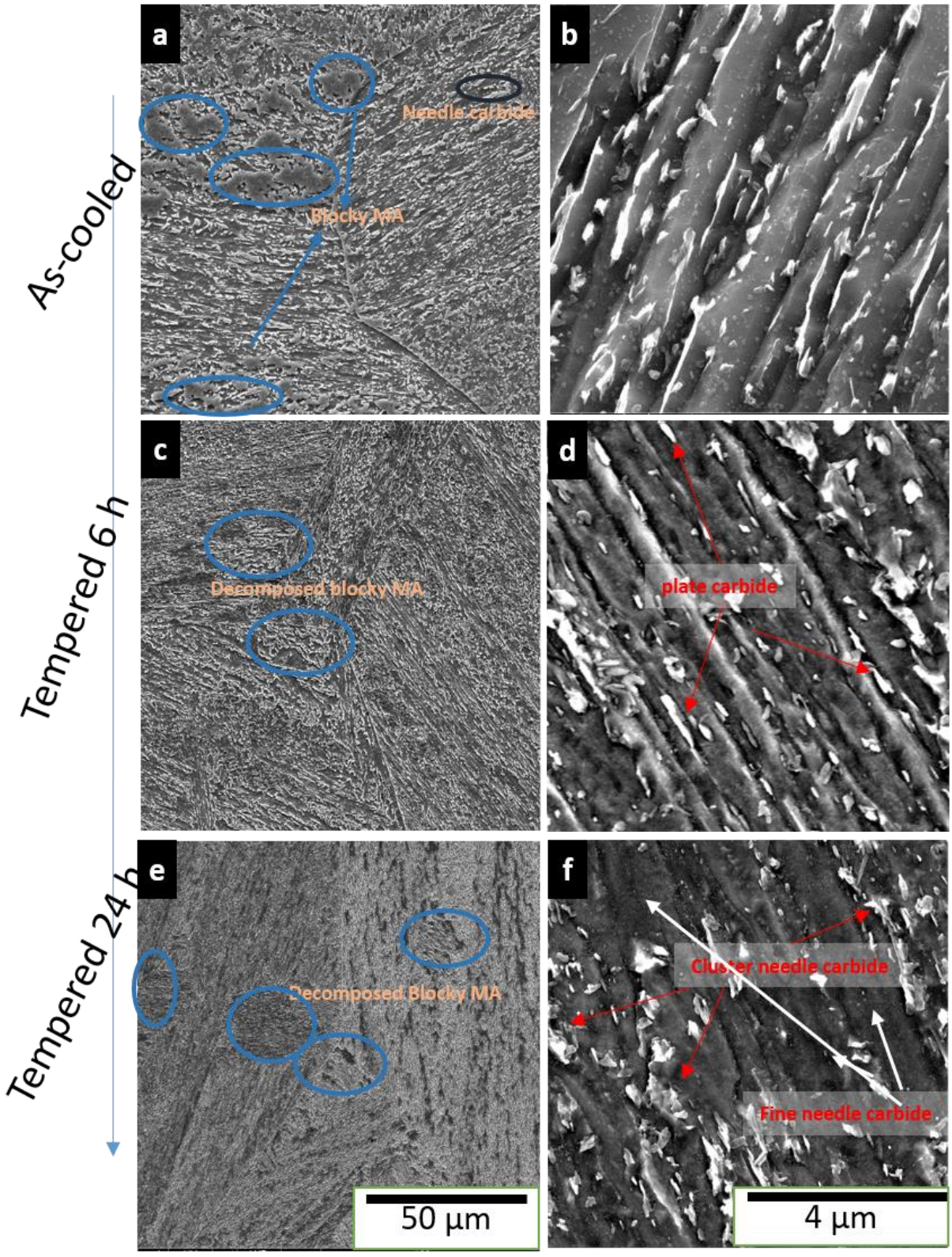

Figure 5-4 Coarse PAGS with cooling rate of 0.07°C/s and different tempering time (a,b) as received (c,d) 6h tempering (e, f)24 h tempering.

5.2.4 Microstructure Variation of SA508 G4N with Finer PAGS at Cooling Rate 0.3 °C/s with Tempering 550 °C for 6h and 24h

Figure 5-5 shows the microstructure of SA508 G4N steel with finer PAGS at cooling rate 0.3 °C/s and tempered at 550 °C for 6 h and 24 h. The predominant microstructure after tempering is tempered lower bainite and tempered martensite, moreover, the lath size increases as the tempering time increases. Table 5-5 summaries lath growth and carbide precipitation and growth during as-cooled tempering time for 6 h and 24 h when sample cooled at 0.3 °C /s as finer PAGS.

At tempering for 6 h, most of carbides have become equiaxed located at either sub-grain boundaries or lath boundaries, with little evidence of carbides within the martensite or bainite laths. Carbide size further increases by approximately 23 % as the tempering time increases from 6 h to 24 h, Figure 5-5f. Table 5-1 provides the carbide and lath sizes after tempering for 6 h and 24 h.

Table 5-5 Summaries lath growth, carbide precipitation and growth during the as-cooled tempering time for 6 h and 24 h when sample cooled at 0.3 °C /s with finer PAGS.

0.3 °C /s – finer PAGS	As-cooled	Tempering 6 h	Tempering 24 h
Carbide precipitation	Inter equiaxed- Intra fine needle carbide	Inter coarse equiaxed (less)- Intra coarse equiaxed	Inter equiaxed cluster Intra finer equiaxed
Carbide growth		Increases around 47 %	Increases around 23 %
Lath width		Increase about 26 %	Increase around 17 % and damage more

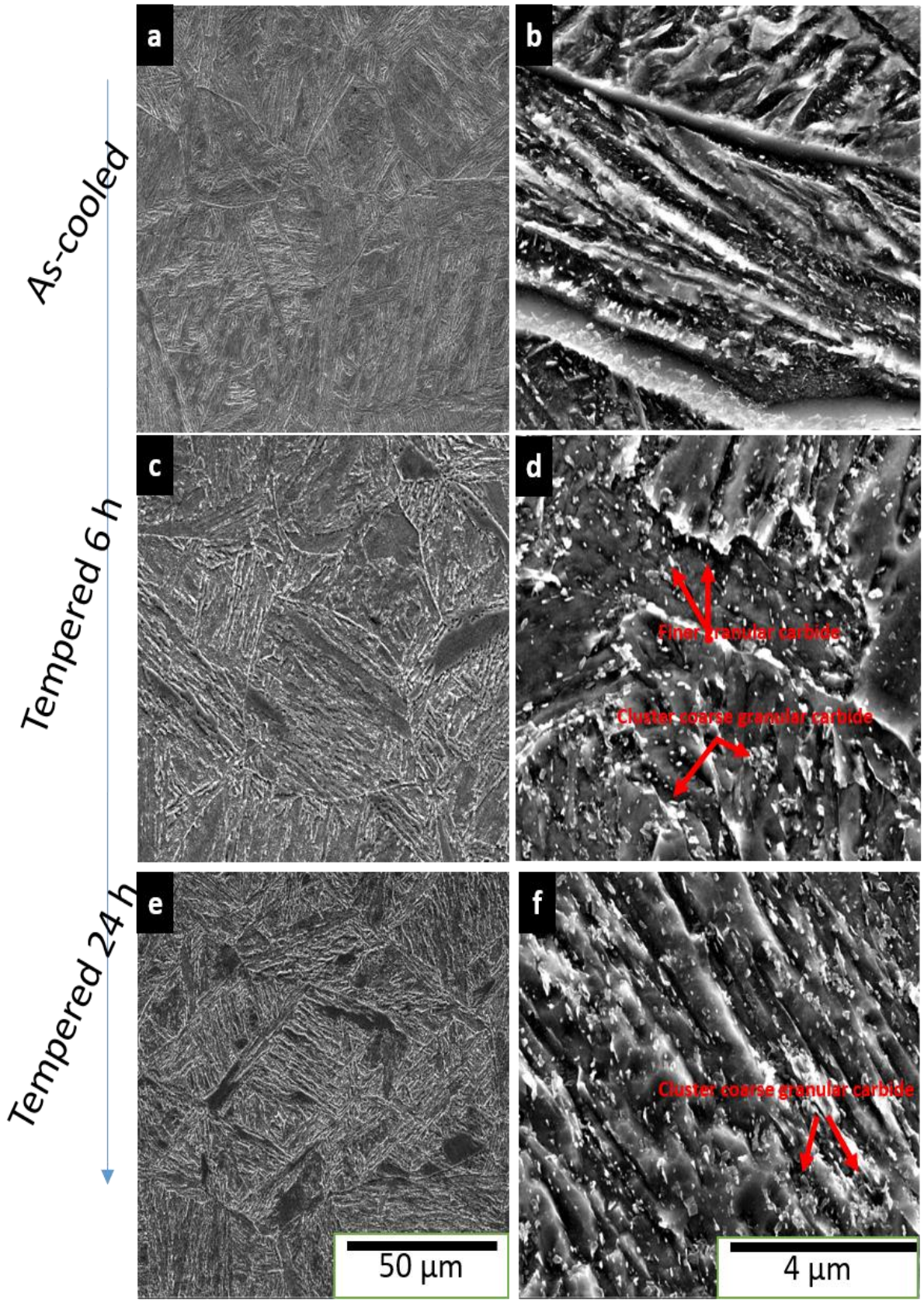

Figure 5-5 Finer PAGS at cooling rate of 0.3 °C/s and different tempering time (a,b)as received, (c,d) 6h tempering and (e, f)24 h tempering.

5.2.5 Microstructure Variation of SA508 G4N with Intermediate PAGS at Cooling Rate of 0.3 °C/s with Tempering 550 °C for 6h and 24h

Figure 5-6 shows the microstructure of SA508 G4N steel with intermediate PAGS at cooling rate 0.3 °C/s and tempered at 550 °C for 6 h and 24 h. The microstructure after tempering is tempered lower bainite and tempered martensite. Both martensitic and bainitic lath sizes increase as the tempering time increases and, in some cases, laths have merged with neighbouring laths to produce much coarser laths [87]. Table 5-6 highlights lath growth and carbide precipitation and growth during as-cooled tempering time for 6 h and 24 h when sample cooled at 0.3 °C /s as intermediate PAGS. Moreover, Table 5-1 provides the carbide and lath sizes after tempering 550 °C for 6h and 24h.

After 6 h tempering, inter and intra bainite carbides grow separately, thus the inter bainite carbide grow faster than intra carbide due to faster solute boundary diffusion on the lath boundaries, promoting growth of the inter bainite carbides, which thus coarsen first [65]. In addition, the finer carbide volume fraction increases rapidly after tempering and precipitates at higher energy positions such as dislocations. After tempering for 24 h, further carbide growth is observed around 17 % and many gather in clusters at the lath boundaries and PAGBs, in addition lath size increases around 8% Figure 5-6f. The clusters of carbides that can be observed at triple junction boundaries suggests there was significant levels of supersaturated carbon atoms in triple junctions [121].

Table 5-6 Summaries lath growth, carbide precipitation and growth during as-cooled tempering time for 6 h and 24 h when sample cooled at 0.3 °C /s with intermediate PAGS.

0.3 °C /s - intermediate PAGS	As-cooled	Tempering 6 h	Tempering 24 h
Carbide precipitation	Inter finer Intra fine needle	Inter finer equiaxed- Intra same size needle	Inter equiaxed finer (cluster) Intra bigger equiaxed
Carbide growth		Size increases by 31 %	Size increases more by 17 %
Lath width		Increase 18 %	Increase around 8 % and damage more

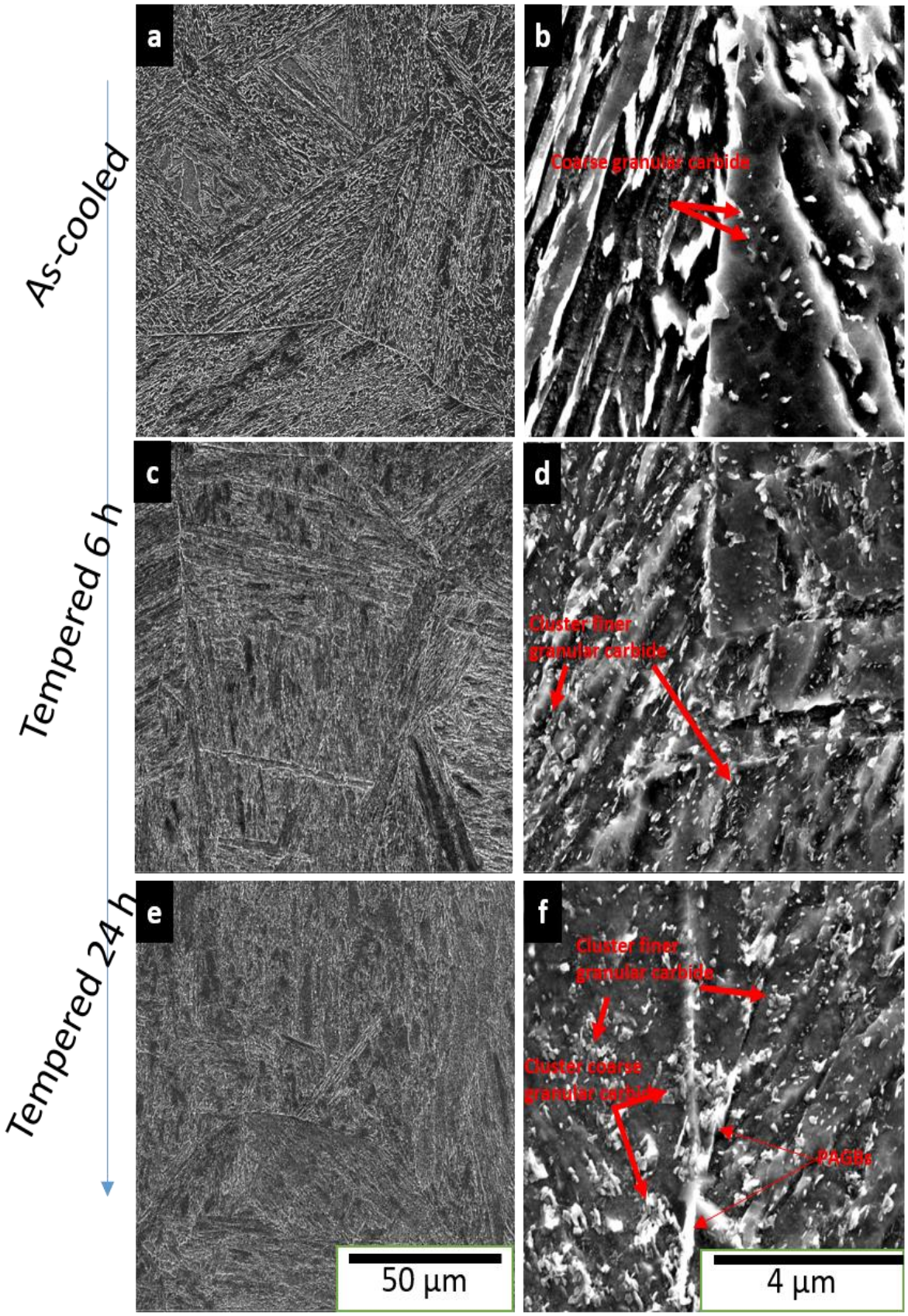

Figure 5-6 Intermediate PAGS at cooling rate of 0.3 °C/s and different tempering time (a) as received (c) 6h tempering (e)24 h tempering.

5.2.6 Microstructure Variation of SA508 G4N with Coarse PAGS at Cooling Rate of 0.3 °C/s with Tempering temperature at 550 °C for 6h and 24h

Figure 5-7 presents the microstructure of SA508 G4N steel with coarse PAGS of cooling rate of 0.3 °C/s and tempered at 550 °C for 6 h and 24 h. The predominant microstructure in the tempering stage is tempered lower bainite and tempered martensite. The response to tempering was very similar to that of the previous section for the intermediate PAGS at the same cooling rate as shown in Figure 5-7 and Table 5-7.

Table 5-7 Summaries lath growth, carbide precipitation and growth during as-cooled material with tempering for 6 h and 24 h when sample cooled at 0.3 °C /s with coarse PAGS.

0.3 °C /s - coarse PAGS	As-cooled	Tempering 6 h	Tempering 24 h
Carbide precipitation	Intra fine needle carbide	Inter equiaxed- Intra fine equiaxed	Inter needle coarse Intra coarse equiaxed Cluster
Carbide growth		Sizes increase by 26 %	Increase more by 15 %
Lath width		Increase around 12 %	Increase more by 10 %

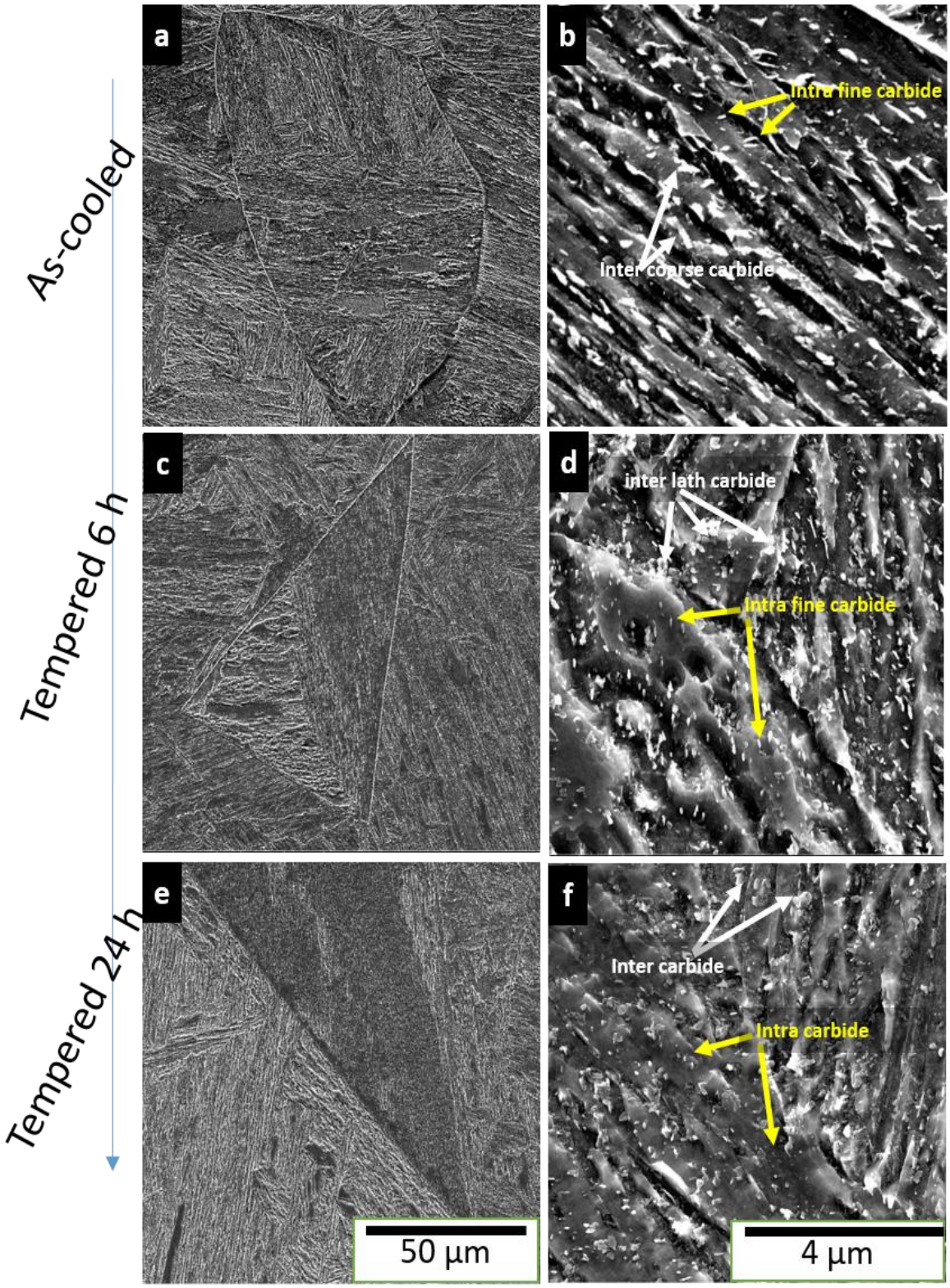

Figure 5-7 Coarse PAGS at cooling rate of 0.3 °C/s and different tempering time (a,b) as-received (c,d) 6 h tempering (e, f)24 h tempering, (white) is cluster inter lath carbide, (yellow) intra fine carbide.

5.2.7 Microstructure Variation of SA508 G4N with Finer PAGS at Cooling Rate of 3 °C/s with Tempering at 550 °C for 6 h and 24 h.

Figure 5-8 shows the microstructure of SA508 G4N steel with finer PAGS with cooling rate of 3.0 °C/s and tempered at 550 °C for 6 h and 24 h. The predominant microstructure is tempered martensite. Martensitic lath width increases around 46 %, and in some cases, laths merge with neighbouring laths to produce coarser laths.

The carbide morphology of the as-quenched sample is intra lath fine needle-like shape carbides aligned in different directions (green) (tempered martensite) for the coarse martensitic laths, while it is difficult to observe either intra or inter lath carbides in the finer martensitic laths, Figure 5-8b [76]. At tempering for 6 h, the as quenched inter martensite carbides have become coarse by around 24 % and equiaxed, while new fine needle-like shaped carbides have nucleated and grown within the martensitic laths. Furthermore, some new fine equiaxed carbides (yellow) form at grain boundaries or sub-structure boundaries, Figure 5-8d. It is also possible to recognize coarse clusters of equiaxed carbides at PAGBs and in particular, at triple junctions. At tempering for 24 h, inter martensite lath carbides cluster (white) as well as increase in number and size by about 27 %, Figure 5-8e, f. However, there is no significant growth in intra martensitic lath carbide, again suggesting that there is significant Si content within these carbides leading to their stabilisation [65]. It should also be noted the dislocation density of the martensitic microstructure is higher in comparison to the bainitic microstructure and thus enhances the rate of carbide formation in martensite compared to bainite, Figure 5-8d, f [122]. Table 5-8 summaries lath growth and carbide precipitation and growth during as-cooled tempering time for 6 h and 24 h when sample cooled at 3 °C /s with finer PAGS. The clusters of carbides that can be observed at triple junction boundaries suggests there were significant levels of supersaturated carbon atoms at triple junctions and a previous studied reported similar observation [121].

Table 5-8 Summaries lath growth, carbide precipitation and growth during as-cooled with tempering time for 6 h and 24 h when sample cooled at 3 °C /s with finer PAGS.

3 °C /s -finer	As-cooled	Tempering 6 h	Tempering 24 h
Carbide precipitation	Intra fine needle	Coarse inter equiaxed carbide- fresh intra fine equiaxed	Inter needle cluster- Intra equiaxed (no change size)
Carbide growth		Carbide coarsening by 24 %	More around 27 %
Lath width		Increase around 24 %	Increase by 22 %

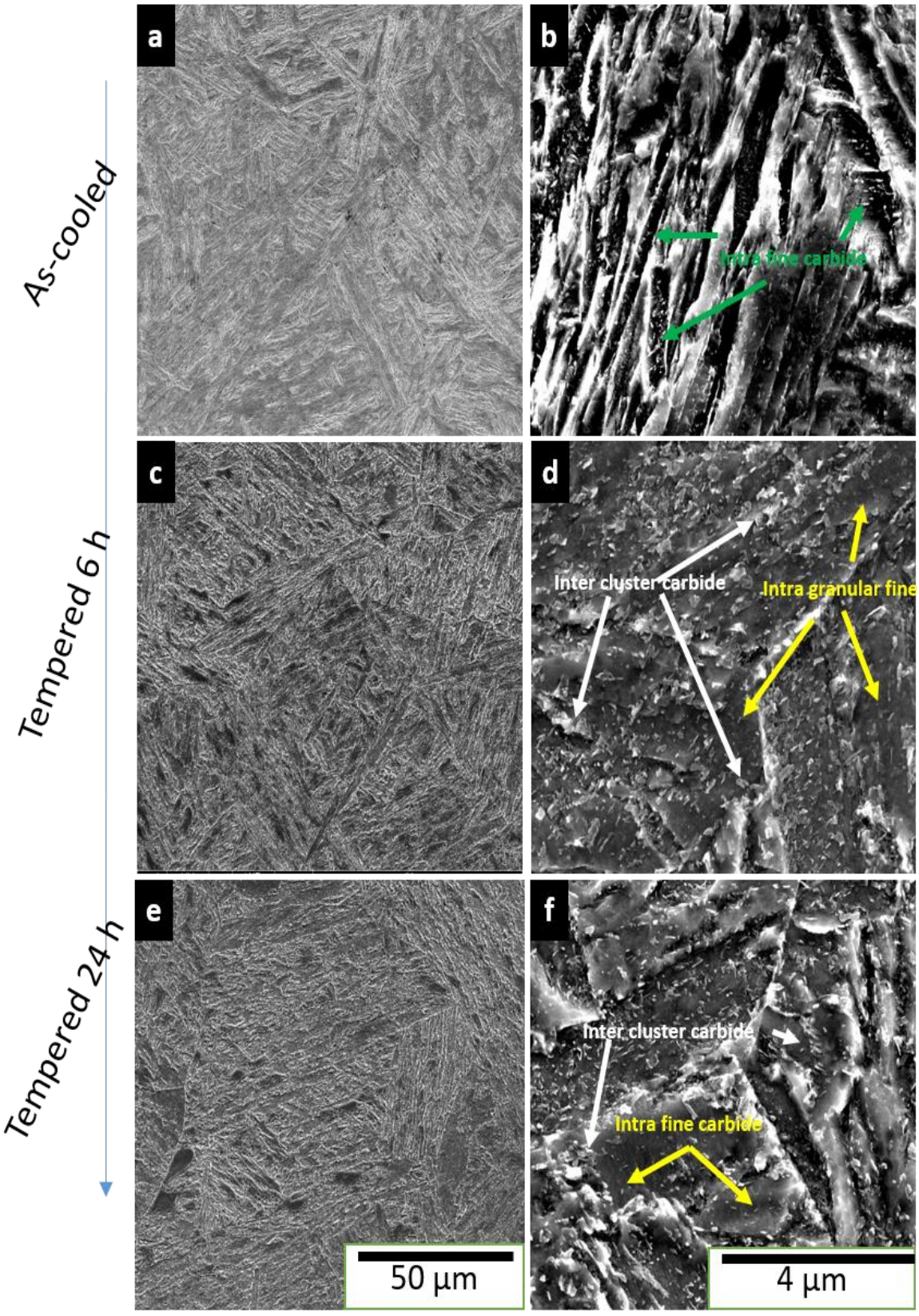

Figure 5-8 Finer PAGS at cooling rate of 3°C/s and different tempering time (a,b)as received (c,d) 6 h tempering (e, f)24 h tempering, (white) is cluster inter lath carbide, (green) intra fine carbide.

5.2.8 Microstructure Variation of SA508 G4N with Intermediate PAGS at Cooling Rate of 3 °C/s with Tempering at 550 °C for 6h and 24h.

Figure 5-9 shows the microstructure of SA508 G4N steel with intermediate PAGS and at cooling rate of 3.0 °C/s and tempered at 550 °C for 6 h and 24 h. The predominant microstructure after tempering stage is tempered martensite. By comparison to the as-cooled specimens, tempered martensitic lath width increases and, in some cases, laths have merged to form much larger laths.

Figure 5-9b shows the as-cooled specimen with martensite microstructure containing inter lath equiaxed carbides and intra lath like-needle finer carbides. In general, the tempering generated further formation of carbides at lath boundaries but no new intra lath carbides and promoted the growth of existing carbides. At tempering 6 h, most of the pre-existing inter and intra lath carbides became coarser by 32 % and equiaxed, while there was also nucleation and growth of new inter lath carbides, which were needle-like in shape, Figure 5-9d.

Increasing tempering time to 24 h lead to a change in morphology of the inter lath (white) carbide to more needle-like shape and there was some level of clustering (white) at PAGBs and triple-junction boundaries, Figure 5-9f. On the other hand, the volume fraction and the size of intra lath carbides (yellow) decreases at the longer tempering time. It is interesting to note that in this case there does not appear to be as big effect of Si on retarding intra lath growth, suggesting that the chemical difference in the intra and inter lath carbides is not as significant as it is in bainite [52]. Table 5-9 summaries lath growth and carbide precipitation and growth during as-cooled tempering time for 6 h and 24 h when sample cooled at 3 °C /s with intermediate PAGS.

Lath width increases as a result of tempering time, and the response to tempering was very similar to that of the previous section for the finer PAGS at the same cooling rate of 3 °C /s, Figure 5-9d, f [122].

Table 5-9 Summaries lath growth, carbide precipitation and growth during as-cooled specimen tempering time for 6 h and 24 h when sample cooled at 3 °C /s with intermediate PAGS.

3 °C /s - intermediate	As-cooled	Tempering 6 h	Tempering 24 h
Carbide precipitation	Inter equiaxed carbide Intra finer	coarser inter equiaxed carbide Fine intra equiaxed	Inter coarse some cluster Intra fine equiaxed Cluster
Carbide growth		Grow around 32 %	Grow more by 24 %
Lath width		Increase around 29 %	Increase more by 38 %

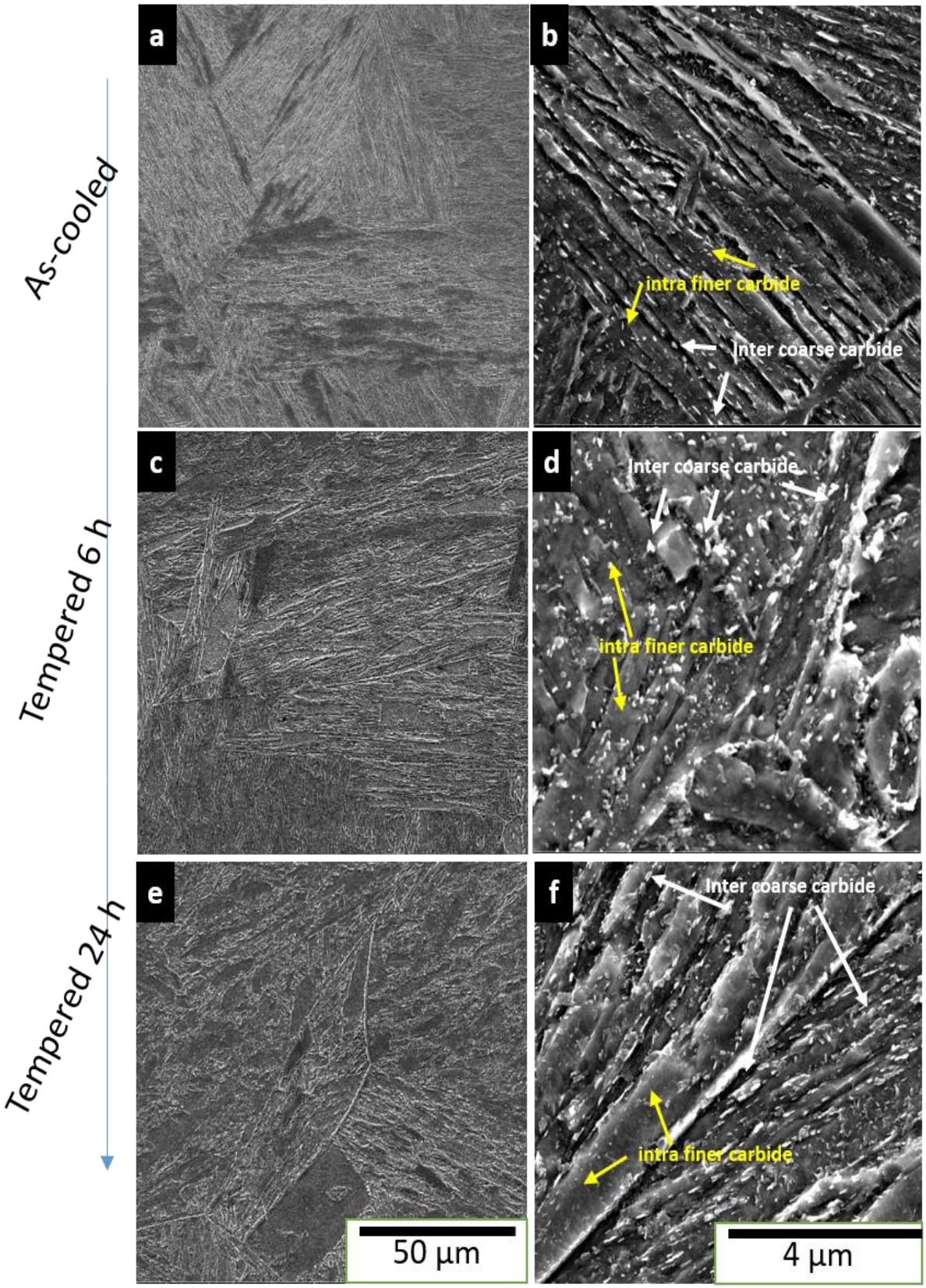

Figure 5-9 Intermediate PAGS at cooling rate of 3 °C/s and different tempering time (a,b)as received (c,d) 5h tempering (e, f)24 h tempering. (white) cluster inter lath carbide, (yellow) intra fine carbide.

5.2.9 Microstructure Variation of SA508 G4N with Coarse PAGS at Cooling Rate of 3 °C/s with Tempering 550 °C for 6h and 24h

Figure 5-10 shows the microstructure of SA508 G4N steel with coarse PAGS and at cooling rate of 3.0 °C/s and tempered at 550 °C for 6 h and 24 h. The dominate morphology is the tempered martensite. A similar microstructure evolution to the previous section discussing intermediate PAGS at cooling rate of 3.0 °C/s and tempered at 550 °C for 6 h and 24 h .

Table 5-10 summarises lath growth and carbide precipitation and growth during as-cooled tempering time for 6 h and 24 h when sample cooled at 0.07 °C /s with coarse PAGS.

Table 5-10 Summaries lath growth, carbide precipitation and growth during the as-cooled tempering time for 6 h and 24 h when sample cooled at 3 °C /s with coarse PAGS.

3 °C /s - coarse PAGS	As-cooled	Tempering 6 h	Tempering 24 h
Carbide precipitation	Intra fine carbide	Inter coarse equiaxed- Intra needle size increases	Inter equiaxed coarse Intra finer equiaxed (no cluster)
Carbide growth		Grow around 25 %	Grow more by 16 %
Lath width		Increase around 28 %	Increase more by 24 %

5.3 Investigation the Variation of PAGS of Individual Cooling Rate of Tempering temperature at 550 °C for 6 h and 24 h

In this section, the effect of variation of PAGS against one cooling rate followed by tempering is investigated to understand its impact on the microstructure evolution.

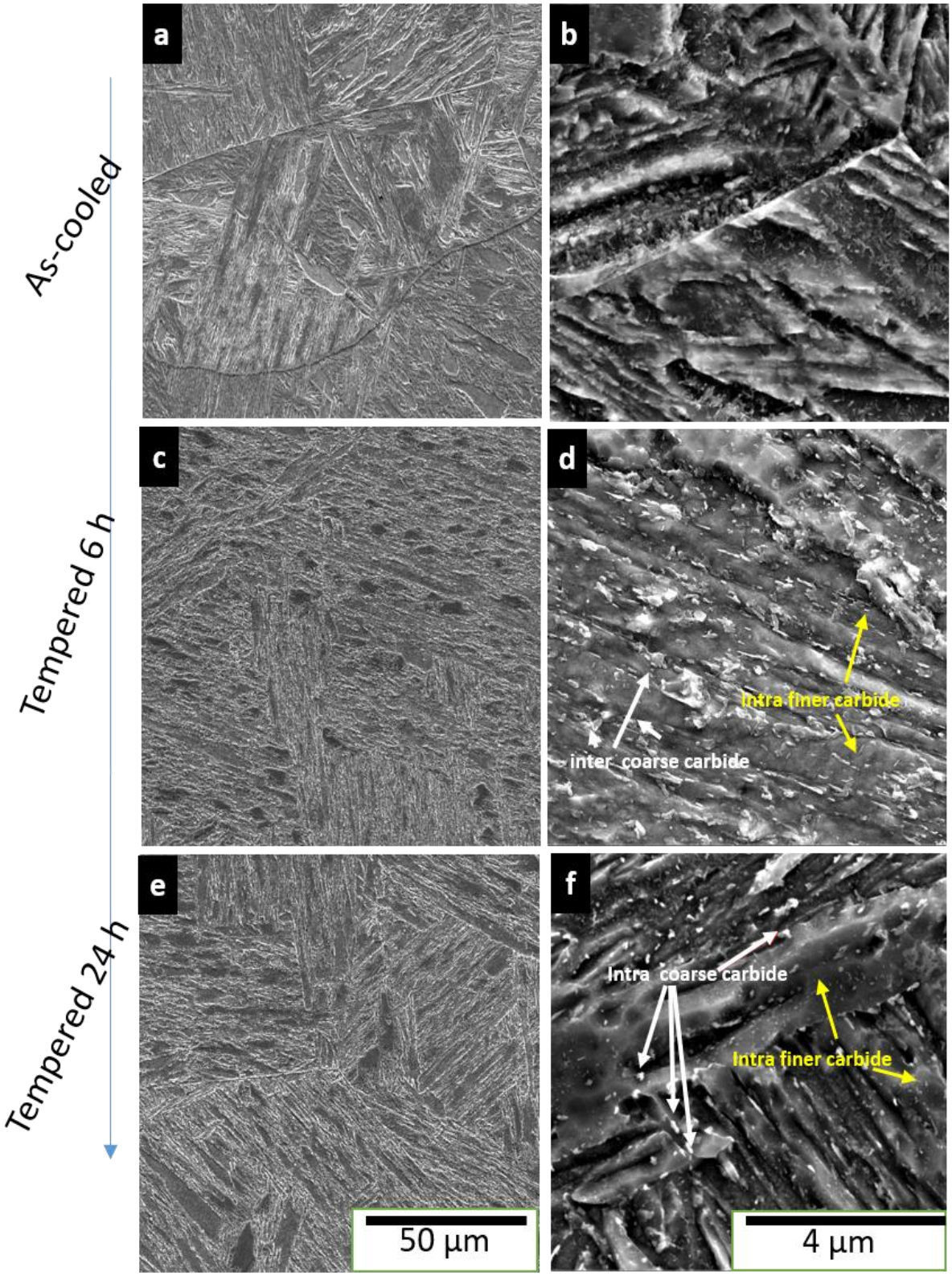

Figure 5-10 Coarse PAGS at cooling rate of 3.0 °C/s and different tempering time (a,b) as received (c,d) 5h tempering (e, f)24 h tempering (white) is intra lath carbide, (yellow) intra fine carbide.

5.3.1 Variation of PAGS at Slower Cooling Rate of 0.07 °C/s with Tempered Steel at 550 °C for 6 h and 24 h

Figure 5-11 shows the microstructure of SA508 G4N steel as a function of variation PAGS at a constant cooling rate of 0.07 °C/s and tempered at 550 °C for 6 h and 24 h. At a cooling rate of 0.07 °C/s, increasing PAGS leads to nucleation of different bainite microstructures. The predominant microstructure is tempered lower bainite for the finer PAGS and granular bainite for the intermediate and coarse PAGS, moreover granular bainite density increases as PAGS increases. Thus, the investigation of an intermediate and coarse PAGS is going to be different from the finer one due to formation granular bainite instead of lower bainite.

At a cooling rate of 0.07 °C/s, a larger PAGS leads to higher new carbide volume fraction. This is caused by the higher level of granular bainite which form wither larger PAGS. After tempering, the material undergoes recovery, reducing the dislocation density. However, the dislocation density remains greater than granular bainite, which also recovers during tempering [75]. Thus, there is a higher potential for precipitation of carbides in the lower bainite. Furthermore, during tempering coarser PAGS granular bainite, the MA decomposed to lower bainite and this leads to expanded volume fractions of lower bainite.

There are two kinds of MA: blocky and needle-like shape with the blocky more stable due to enrichment of carbon content [36]. Moreover, coarse PAGS has higher volume fraction of granular bainite and therefore higher numbers of MA islands. MA decomposed to lower bainite and most likely $M_{23}C_7$ [39] carbides because of the high Cr component of SA508 G4N [36].

The most significant observation of 0.07 °C/s cooling rate is that for finer PAGS 23 µm, lower bainite is predominant microstructure as was discussed in Sections 4.6.1 and 4.6.2. On the other hand, at intermediate and coarse PAGS, the predominant microstructure is granular bainite with a small volume fraction of lower bainite, which is a result comparable to Yang result [39]. Larger PAGS at the slow cooling rate of 0.07 °C/s promotes the formation of granular bainite owing to rapid diffusion of austenite stabilising elements ahead of the transforming front, eventually leading to very stabilised austenite, which upon further cooling partially transforms to martensite to generate the MA islands [37]. Moreover, the volume fraction of blocky MA island increases proportional to PAGS.

The average bainitic lath width is inversely proportional to the PAGS, so increasing PAGS decreases the bainitic lath width, which is not the behaviour found with martensite. After tempering, the volume fraction of bainitic lath inter and intra carbides decrease as the PAGS

increase from intermediate to coarse sizes due to the fact that the MA island volume fraction increases. It has been suggested that higher volume fraction of MA islands in bainitic microstructure leads to a decrease in the dislocation density of granular bainite as a result of higher carbon content at MA island [9].

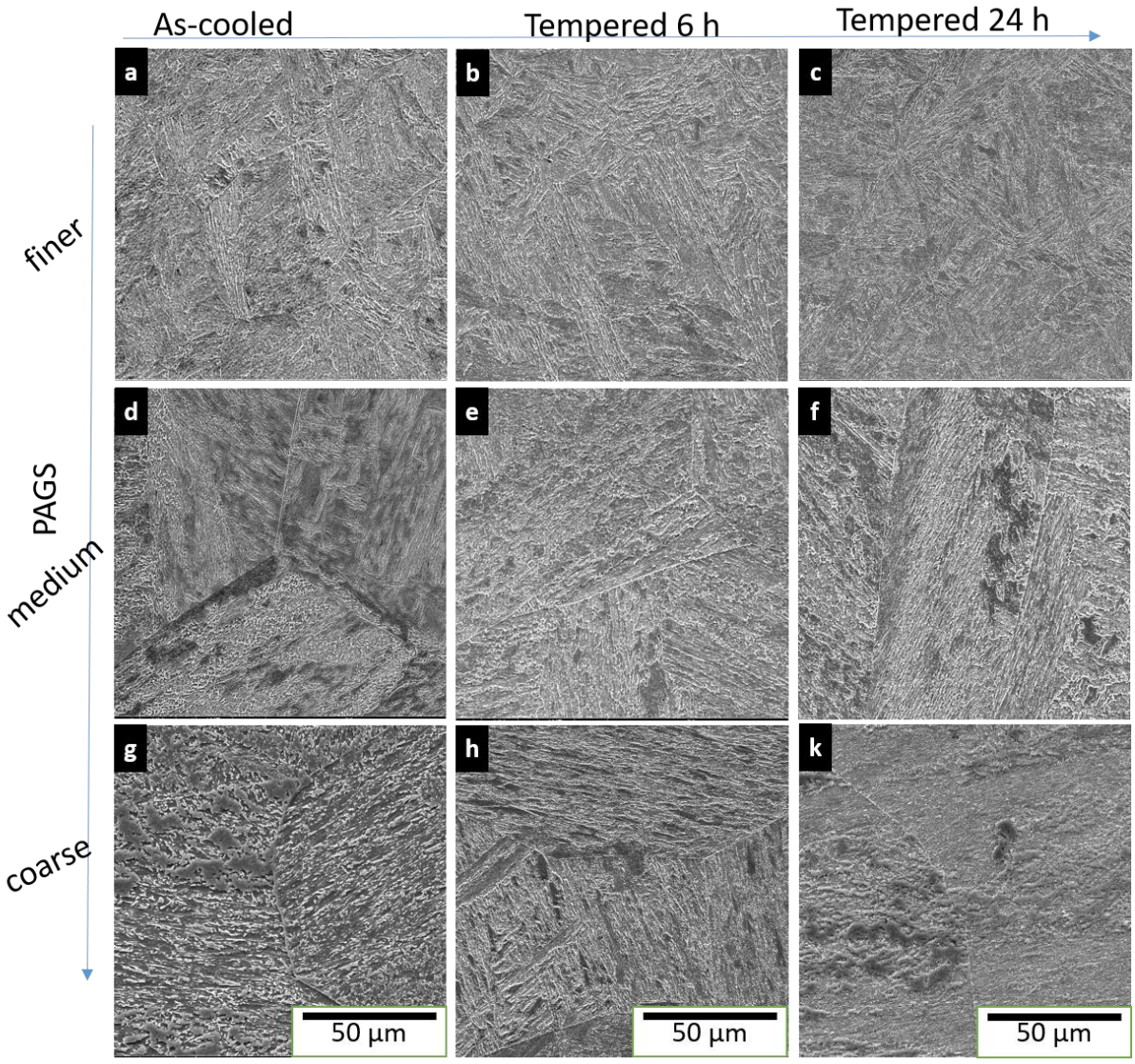

Figure 5-11 Micrograph of different PAGS at cooling rate of 0.07 °C/s and different tempering time (a,b,c) finer PAGS (d, e, f) intermediate (g, h, k)coarse. (a,d,g)as-cool (b,e.h) 5h tempering (c,f,k)24 h tempering.

Figure 5-12 provides a schematic diagrams of carbide formation at the slowest cooling rate of 0.07 °C/s, tempered for 6 h and 24 h variation in austenitisation temperature. Figure 5-12A represents a schematic diagram of the definition of bainitic morphologies.

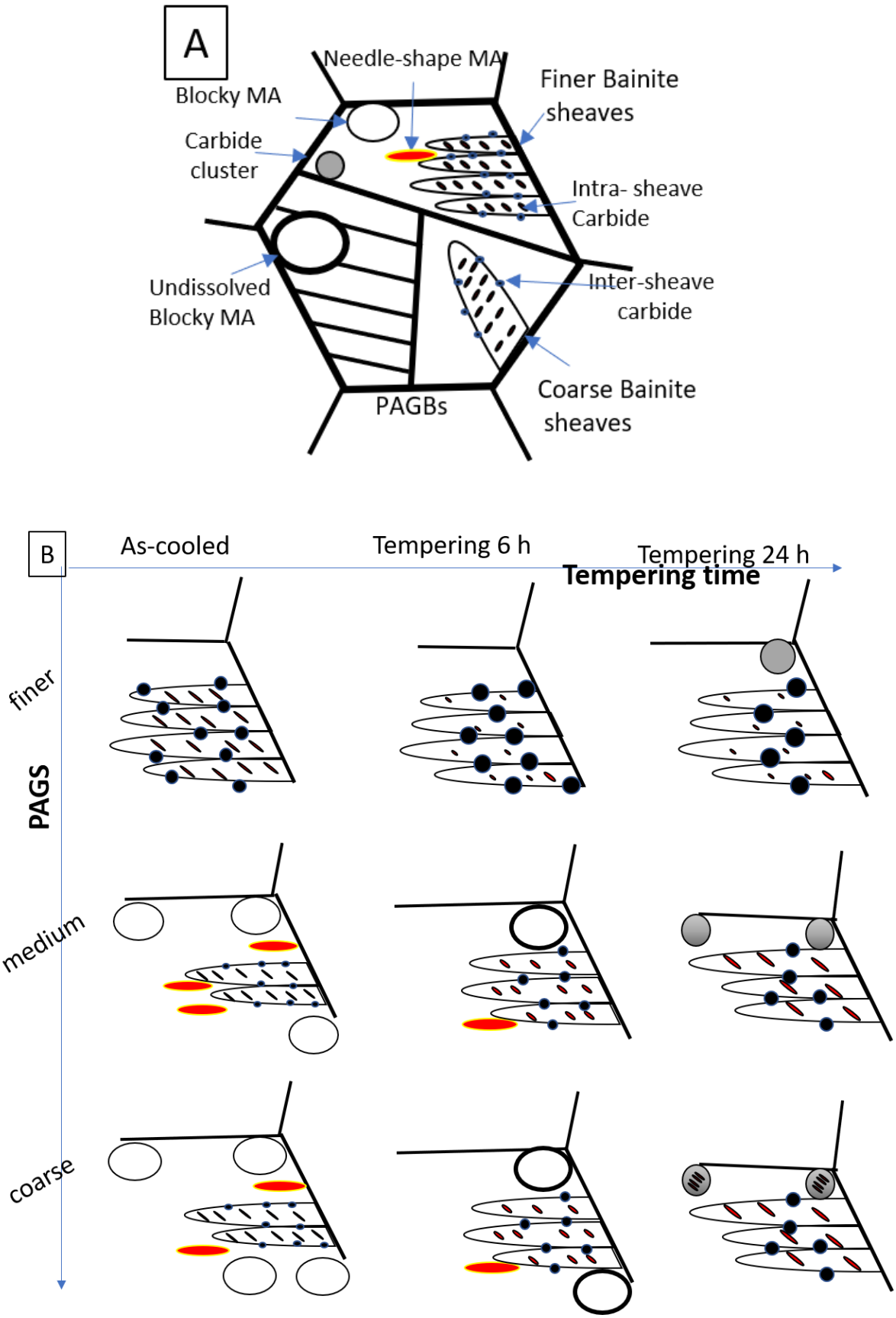

Figure 5-12 (A) definition of bainitic morphologies. (B)Schematic diagram of carbide formation at slower cooling rate of 0.07 °C/s for as-cooled sample, tempered 6 h and 24 h with variation of PAGS.

5.3.2 Variation of PAGS at Cooling Rate of 0.3 °C/s with Tempered Steel at 550 °C for 6 h and 24 h

The dominate morphology after tempering temperature at 550 °C for 6 hour and 24 hour is tempered lower bainite and tempered martensite, with no evidence of granular bainite, Figure 5-13.

The most significant observation at as-cooled material at cooling rate of 0.3 °C/s is that increasing PAGS increases the tempered martensite volume fraction due to an increase in the like hood of auto-tempering. Moreover, after tempering, it can be recognized that there are coarser martensitic and bainitic laths as well as growth of existing carbides and nucleation of new carbides. The new carbide density, however, decreases due to the coarse PAGS martensite and bainite laths having a lower dislocation density because of the higher level of auto-tempering the material experience during cooling. The behaviour of lower bainite lath growth during tempering is not the same as the response following at cooling rate of 0.07 °C/s. For the finer PAGS the lower bainite at 0.3 °C/s Figure 5-5d has higher volume fraction of dislocation density compared to the materials cooled at 0.07 °C/ Figure 5-2d, thus there is a higher potential for precipitation, which after tempering leads to a greater level of precipitation of new carbides. Furthermore, the most remarkable behaviour of martensite lath carbide precipitation after tempering is that the volume fraction of tempered martensite at intermediate PAGS is the lowest among the other PAGS. Martensite carbides appear to form more rapidly at intermediate PAGS at PAGBs and martensite lath boundaries, and this increases the carbide volume fraction on further tempering, which is not the case for the finer and coarser PAGS. Moreover, martensite intra lath clusters of equiaxed carbide is recognised due to higher dislocation area that attracts carbon and nucleates new carbide and enhances increasing size of the existing carbide.

The martensite inter and intra lath carbides grow independently during tempering, however, the growth rate of martensite inter lath carbide is higher due to faster solute boundary diffusion on the lath boundaries Table 5-1. Moreover, carbide clusters are more likely to observed at martensitic lath boundaries and triple junction boundaries with all PAGS Figure 5-8d, f.

Coarse PAGS of 0.3 °C/s as-cooled material has the coarsest average martensite and bainite lath width and this behaviour is translated to the tempering stage where the coarse PAGS have the coarsest average martensite lath width, but the rate of growth is higher for the martensite lath has more potential to be grow during the tempering stage as a result of higher driving force for growth owing to a higher dislocation density than bainite [121].

The most interesting observation of as-cooled specimens at cooling rate of 0.3 °C/s with variation of PAGS is that intra needle-like bainitic lath carbide precipitated with a uniform direction, furthermore after tempering intra carbide become coarse equiaxed-like carbide and finally, becomes needle-like again but much coarser. On the other hand, fine inter equiaxed-like bainitic lath carbides are observed in the case of as-cooled material, then after tempering they grow in size and reduce in number, and finally with tempering for 24 h become needle-like again. Inter bainitic lath carbide numbers decrease but the volume fraction does not change, indicating the coarse carbide consume the finer carbides.

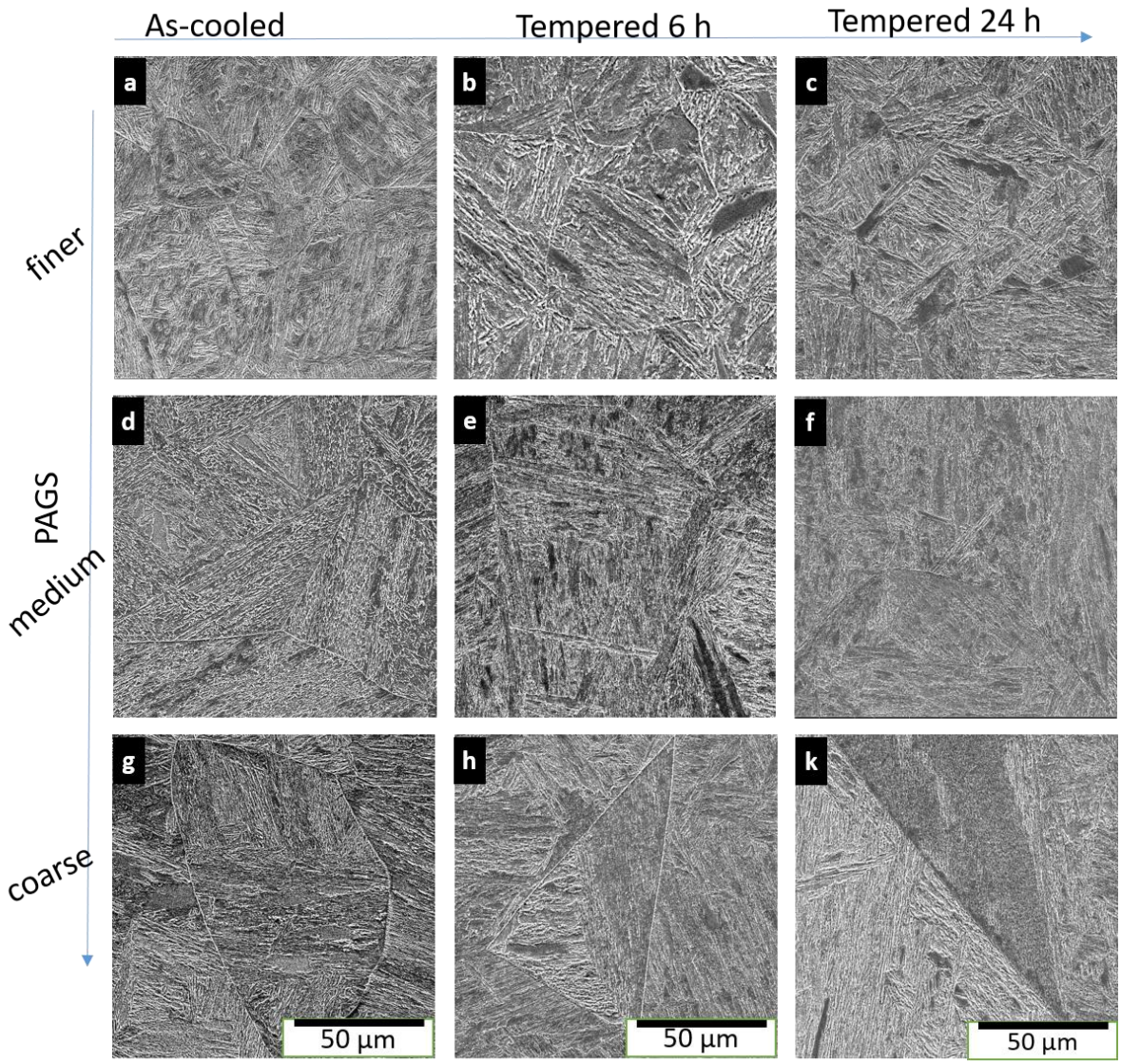

Figure 5-13 Typical micrograph different PAGS at cooling rate of 0.3 °C/s and different tempering time (a,b,c) finer PAGS (d, e, f) intermediate (g, h, k)coarse. (a,d,g)as-cool (b,e.h) 6h tempering (c,f,k)24 h tempering.

5.3.3 Variation of PAGS at Fastest Fooling Rate of 3.0 °C/s with Tempered steel at 550 °C for 6 h and 24 h

Figure 5-14 shows the microstructure of SA508 G4N steel at variation of PAGS and cooling rate at 3.0 °C/s, tempered at 550 °C for 6 h and 24 h. The predominant microstructure is martensitic for all PAGS investigated.

The most significant observation following tempering for 6h is that reducing PAGS increases the growth rate of martensitic laths and carbides Table 4-4 owing to a higher dislocation density in the as-transformed martensite Figure 4-19f. Carbide clusters forms earlier in tempering with coarse PAGS at grain boundaries and triple junctions Figure 5-10d, which is not the case for finer and intermediate PAGS.

The inter and intra martensite lath carbides grow separately after tempering, however the growth rate of martensite inter lath carbide is higher due to faster solute boundary diffusion on the lath boundaries. After tempering for 6 h, the intermediate PAGSs has the largest intra and inter coarse carbides with a much lower number density in comparison to the fine and coarse PAGS. Additionally, the intermediate PAGS has a smaller density of coarse equiaxed carbides at lath boundaries. However, for the coarse PAGS martensite lath needle-like carbides are observed the PAGBs.

Coarse PAGS of 3 °C/s as-cooled material has the coarsest average martensite lath width and this behaviour is translated to the tempering stage where the coarse PAGS have the coarsest average martensite lath width. Figure 5-15b provides a schematic diagrams of carbide formation with highest cooling rate 3.0 °C/s of as-cooled sample, tempered 6 h and 24 h of tested material SA508 G4N with variation austenitisation temperature. Figure 5-15a summaries the definition of martensitic morphologies.

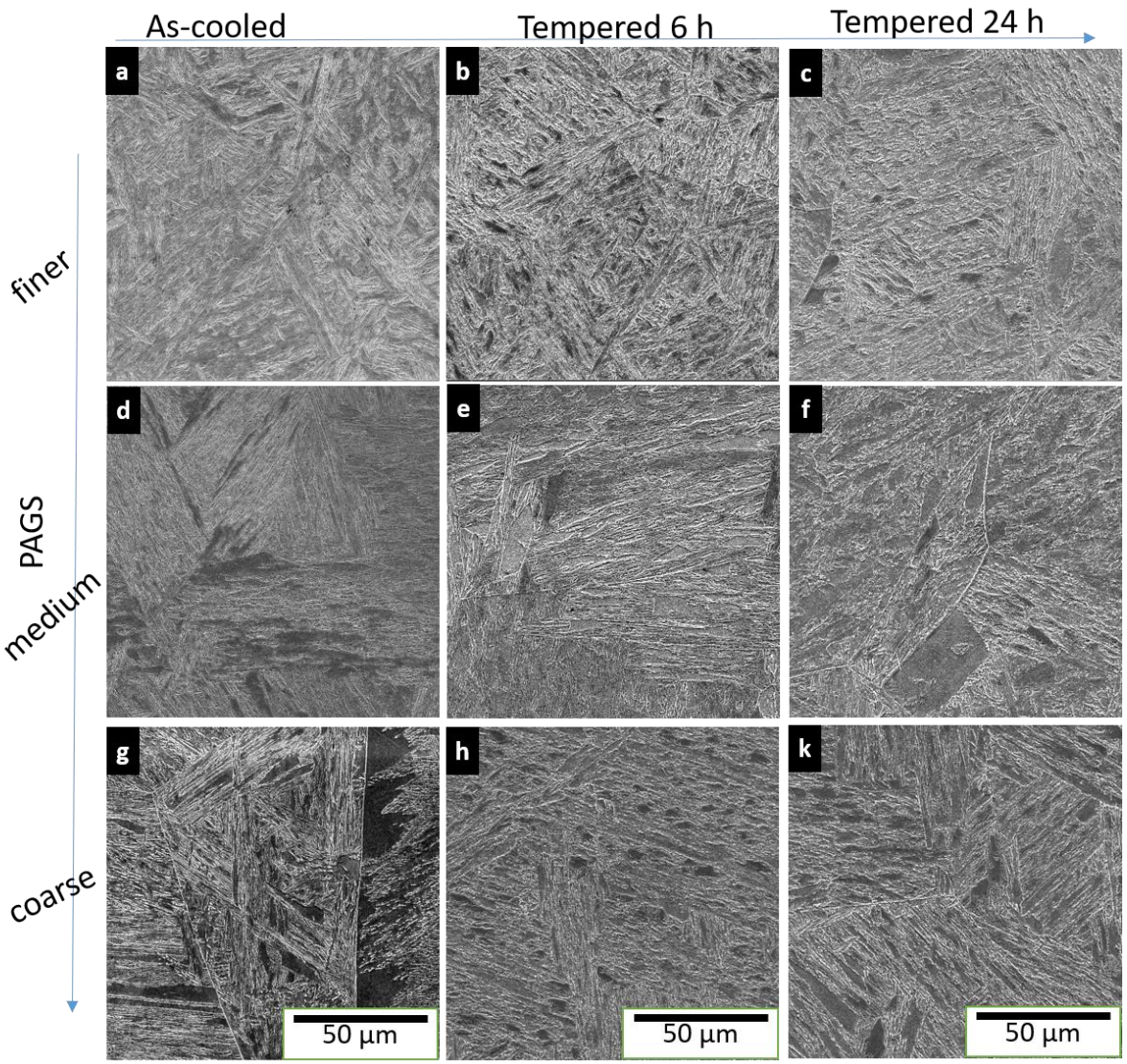

Figure 5-14 Micrograph of different PAGS at cooling rate of 3°C/s and different tempering time (a,b,c) finer PAGS (d, e, f) intermediate (g, h, k) coarse. (a,d,g) as-cool (b,e.h) 6 h tempering (c,f,k)24 h tempering.

5.4 Hardness test

Hardness was evaluated for the as-cooled, tempered for 6 h, and tempered 24 h specimens. A minimum of 10 indentation were made for each sample and the average was considered as the hardness plus the standard deviation was calculated to describe the error in the measurements. In general, materials with coarse bainitic laths had lower hardness in contrast to finer bainite lath material due to lower volume fraction of dislocation density and higher potential for auto tempering, in addition the coarse lath has lower work hardening behaviour owing to the Hall-Petch effect [87].

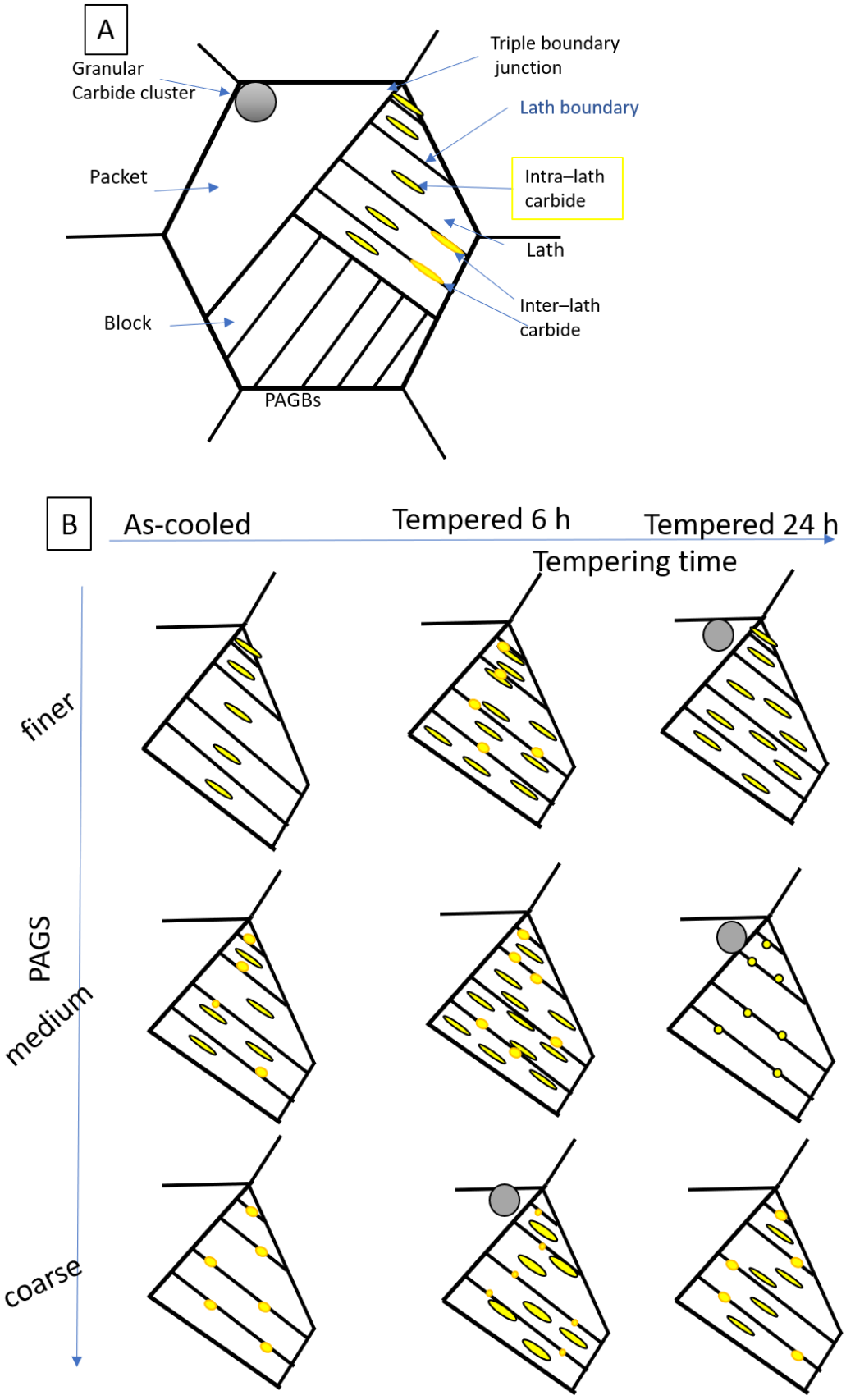

Figure 5-15 Schematic diagram of carbide formation at highest cooling rate of 3.0 °C/s for as-cooled sample, tempered 6 h and 24 h. (A) definition of martensitic morphologies.

5.4.1 Hardness of As-cooled Samples

Figure 5-16a shows a bar chart of hardness values against variation of austenitisation temperatures 950 °C, 1100 °C/s and 1175 °C/s, respectively, while Figure 5-16b represents hardness values with respect to cooling rates at 0.07 °C/s, 0.3 °C/s and 3 °C/s, respectively.

For the fine PAGS (austenitisation temperatures 950 °C) increasing the cooling rate from 0.07 °C/s through to 3 °C/s had its biggest effect from 0.07 °C/s to 0.3 °C/s. This cooling rate jump led to an increase in the hardness from 440 Hv to around 500 Hv, while increasing to 3 °C/s lead to no significant increase in hardness. This suggests the transition from a lower bainite microstructure to a mixed microstructure of Lower bainite and martensite is much more impactful on hardness than the transition from Lower bainite to Martensite, which were the main phases at the higher cooling rates. A similar trend is also observed for the intermediate and coarse PAGS, with an increase of about 50 Hv and 100Hv for the cooling rate jump from 0.07 °C/s to 0.3 °C/s for the intermediate and coarse PAGS, respectively. Martensite microstructure has a higher density of dislocations and a greater amount of carbon in solution in comparison to bainite, thus there is great barriers to dislocation movement in martensite and thus higher hardness [120],[122].

The general trend of the effect of PAGS is that increasing PAGS reduces the hardness, which is in line with the work of Kennett [124] Figure 5-16b. The biggest relative effect is at the slowest cooling rate of 0.07 °C/s where there is a reduction of nearly 70 Hv from the fine to coarse PAGS. At the higher cooling rates, the hardness is higher and the drop from in hardness from fine to coarse PAGS is 40Hv. Hence, in relative terms the effect of PAGS at higher cooling rates is much less than at the slowest cooling rate. This is an interesting observation, increasing PAGS on bainitic morphology leads to decrease in the bainitic lath width and it decreases the hardness values owing to the boundaries acting as strong obstacles of dislocation motion, leading to dislocation pile up, i.e., the Hall-Petch (H-P) relationship [77]. On the other hand, there is no obvious role of the lath length on the hardness values. This would suggest that PAGS has its biggest effect when the transformation temperature is relatively high and there is time during transformation for recover, carbide precipitation or auto tempering. It not very clear with higher cooling rates.

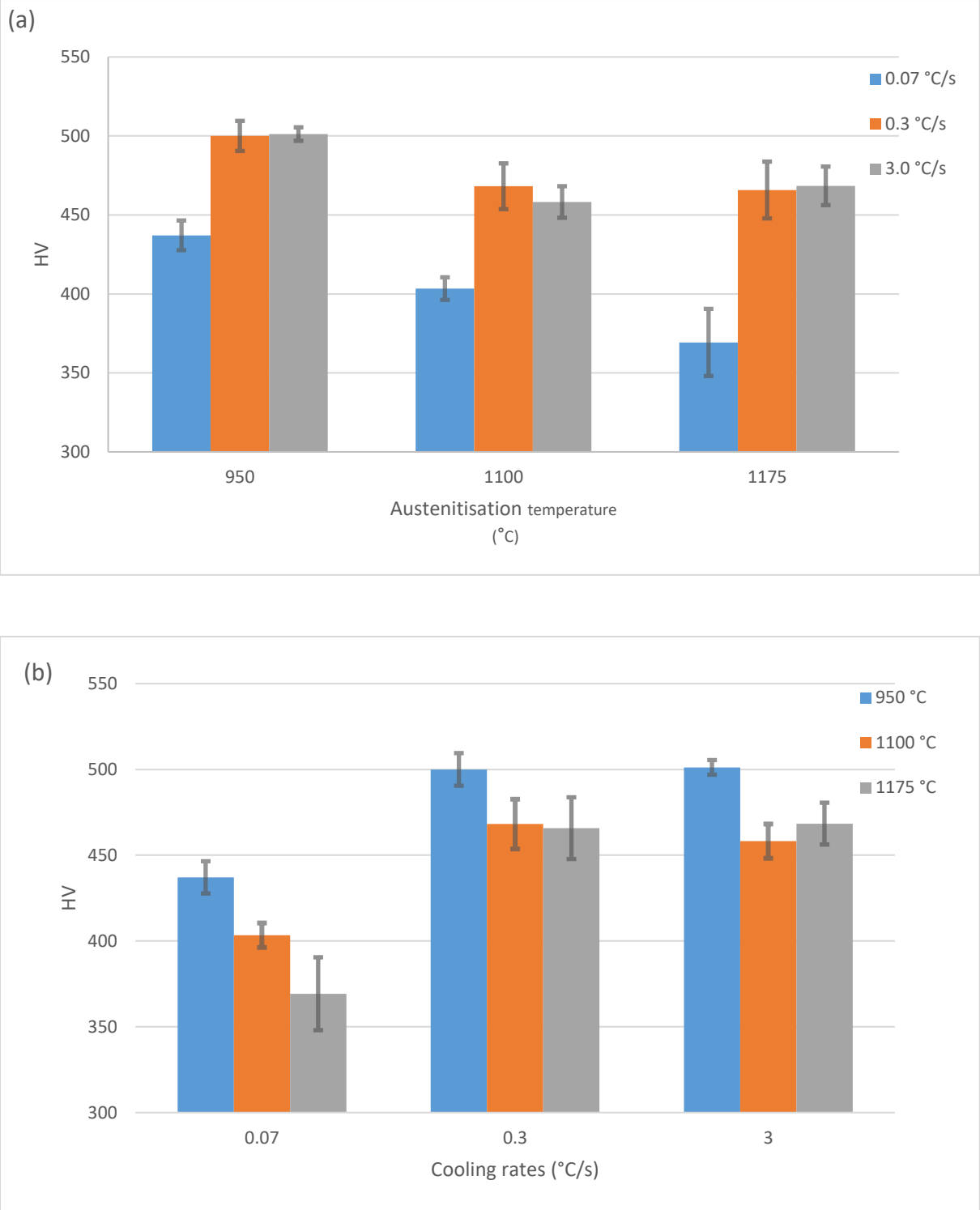

Figure 5-16 Shows Hv hardness results of SA508 G4N as-cooled (a), Hv Vs. austenitisation temperature, (b) Hv Vs. cooling rates.

5.4.2 Hardness Hv with tempering samples at 550 °C for 6 h

Figure 5-17a shows the hardness values against the variation of austenitisation temperature of 950 °C, 1100 °C and 1175 °C, respectively for the tempering parameters of 6 h and 550 °C,

while Figure 5-17b represents hardness values of tested specimens with specimens tempered for 6 h against the variation at cooling rates of 0.07 °C/s, 0.3 °C/s and 3 °C/s, respectively.

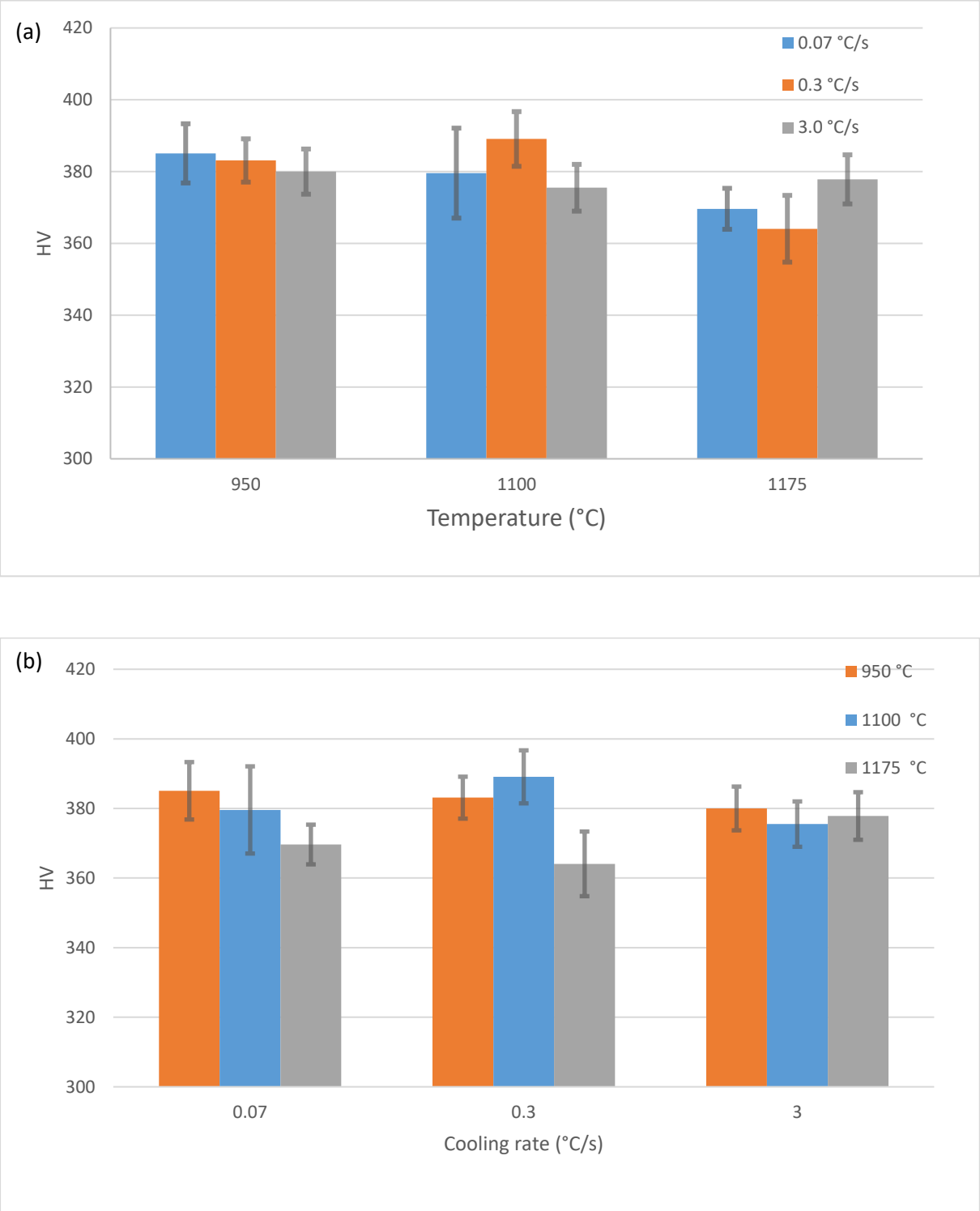

Figure 5-17 Shows Hv hardness results of SA508 G4N tempered at 550 °C for 6 h (a), Hv Vs. austenitisation temperature, (b) Hv Vs. cooling rates.

It is clear that for the higher cooling rates tempering for 6 h significantly reduces the hardness in comparison to the as-cooled specimens. For the slowest cooling rate, there is a reduction in for the fine and intermediate PAGS but in fact the coarse PAGS has similar hardness to as-cooled. In general terms, the effect of PAGS on hardness that was present in the as-cooled samples still exists, but it is not as obvious, i.e., now an increasing PAGS on slightly reduces hardness. It is difficult to say there is any significant effect of cooling rate on the hardness after 6h tempering.

5.4.3 Hardness Hv with tempering samples at 550 °C for 24 h

Figure 5-18a shows the hardness values against variation of austenitisation temperature 950 °C, 1100 °C and 1175 °C, respectively for the tempering parameters of temperature 550 °C for 24 h, while Figure 5-18b shows the hardness values for specimens tempered for 24 h against variation of cooling rates 0.07 °C/s, 0.3 °C/s and 3 °C/s, respectively.

At first glance, it can be recognised that tempering drives to decrease the hardness by more than 130 Hv in comparison to the as-cooled specimens and around 30 Hv in comparison to specimens tempered for 6 h. Moreover, hardness values are relatively uniform and there are no obvious effects of cooling rate or PAGS on the hardness since the Hv value between 340 to 355.

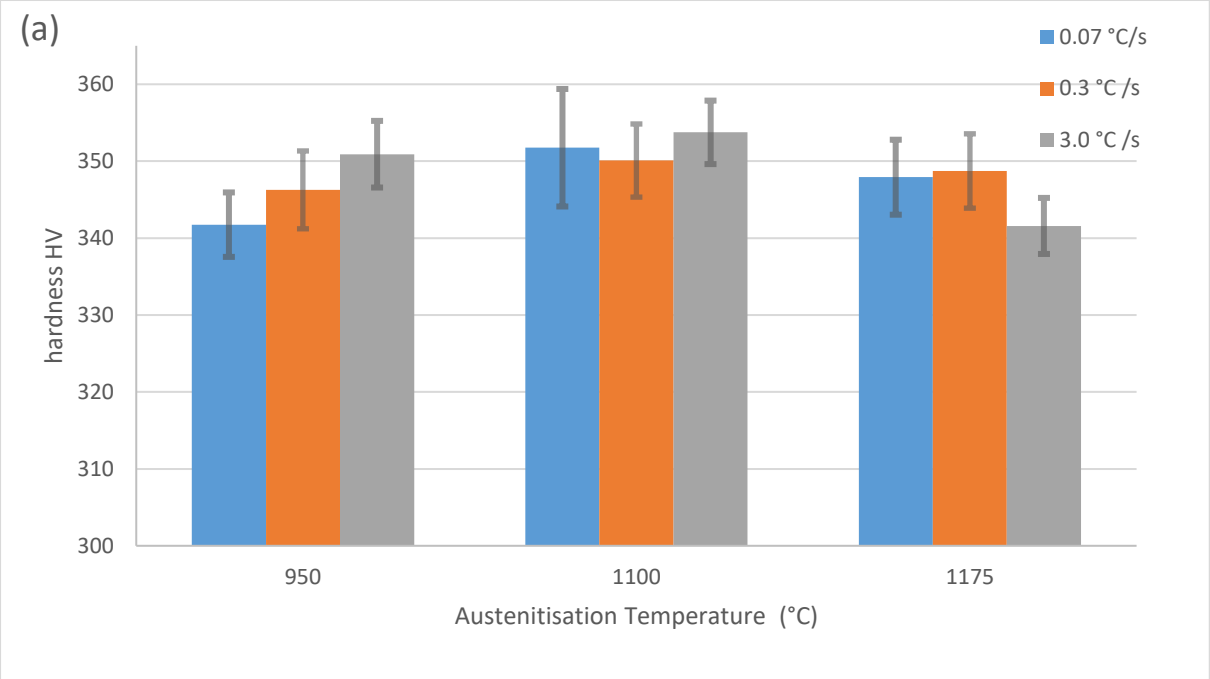

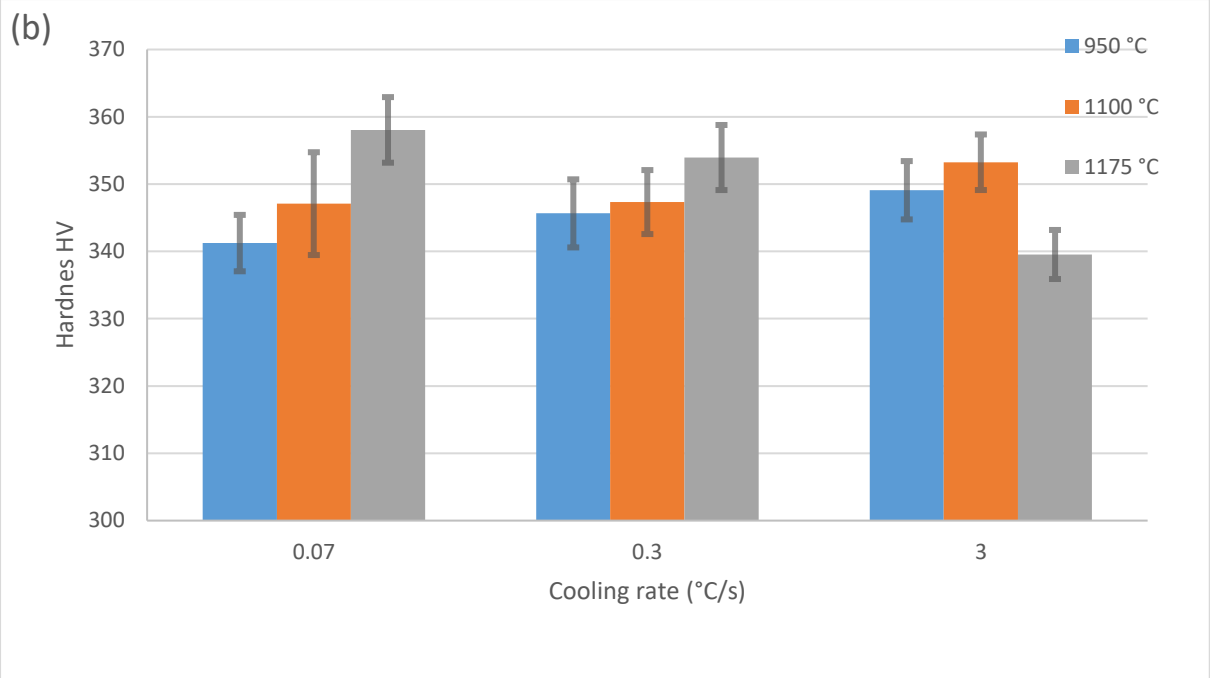

Figure 5-18 Shows Hv hardness results of SA508 G4N tempered at 550 °C for 24 h (a), Hv Vs. austenitisation temperature, (b) Hv Vs. cooling rates.

On the other hand, the most significate trends are that Vickers hardness values slightly uniform with PAGS variation and it fluctuated between 342 and 353 Hv Figure 5-18b. However, at the cooling rates of 0.3 °C/s and 3°C/s, hardness almost does not change when PAGS increases from intermediate to coarse size. Moreover, despite of the variation hardness between the bainite and martensite, the fluctuation of standard deviations is low due to increase the uniformity after tempering stage. After tempering for 24 h, the hardness reaches the minimum regardless of the PAGS, moreover hardness drops due to the fact that over tempering caused by coarsening of tempered carbide particles. Increasing tempering time for 24 h leads to coarse lath width and reduced grain boundary volume fraction. Furthermore the softening resistance is strongly associated with dislocation movement obstacles for example PAGBs, lath boundary and precipitation carbide [125]. The average size of carbides was found to be influenced by tempering conditions. It has been suggested that solute boundary hardening on the lath boundaries and the increasing of the Cr-carbides volume fraction have a key factor to determine the hardness after tempering for 24 h.

5.5 Summary

This chapter highlighted the effect of tempering on microstructures analysed in Chapter 4 as well as the effect it had on hardness. Moreover, the chapter shows the effect of PAGS on carbide and lath size, carbide growth microstructures and hardness in respective to industrial

prospective for new generation PRV. Finally, studying the impact of variation of PAGS and cooling rates on the hardness test is investigated during as-cooled and tempering conditions. At cooling rate of 0.07 °C/s, the predominant microstructure is tempered lower bainite for the finer PAGS and granular bainite for the intermediate and coarse PAGS, moreover granular bainite density increases as PAGS increases. On the other hand, at cooling rate of 3 °C/s after tempering, the microstructure is predominantly tempered martensite, regardless of prior austenite grain size. However, at cooling rate of 0.3 °C/s after tempering, there are coarser martensitic and bainitic laths. Growth of existing carbides and nucleation of new carbides occurs as prior austenite grain size increases. The carbide density decreases when a lower dislocation density is present because of the higher level of auto-tempering the material experience during cooling.

Hardness increases proportional the cooling rates, and reversely proportional with PAGS. Moreover, hardness values decrease as the tempering time increases. Hardness is sensitive to PAGS with bainitic microstructure, however mixture of martensite and bainite microstructure and fully martensitic morphology are less PAGS sensitive. Finer PAGS is harder phase in fully martensite microstructure and this same behaviour to mixture phases due to formation tempered martensite.

6 Conclusion and Further Work

6.1 Chapter Overview

It is well known that because of the risk averse nature of nuclear power plant design and operation the alloy used for RPVs (SA508) will not change significantly, and therefore to go to thicker RPV sections for next generation power plants there must be greater understanding of how the microstructure evolves and can be controlled during manufacture. A key element where there is little information is in the effect of prior austenite grain size on transformation product and morphology, particularly under the cooling rates the RPV would experience during the quality heat treatment. Thus, the objective of this work was to understand the effect of PAGS in SA508 Gr4N on microstructure evolution to give clear guidance to the nuclear industry about any potential issues that having varying austenite grain size at the point of quality heat treatment may have in future performance in service. The conclusions from the work are presented below.

6.2 Conclusion

6.2.1 Austenitising

- Increasing austenitisation temperature produces larger PAGS for SA508 G4N.
- At austenitisation temperatures of 950 °C, 1100 °C and 1175 °C for 5 h, the measured PAGS were 23 μm, 83 μm and more than 412 μm, respectively.

6.2.2 Quenching from Austenitisation Temperatures

- Lower bainite with bainitic laths containing intra needle-like carbides was observed at lower cooling rate of 0.07 °C/s at a fine PAGS.
- A combination of lower bainite and martensite were the dominate phases at a cooling rate of 0.3 °C/s.
- At cooling rate of 3.0 °C/s, fully martensitic structure with lath morphology was predominate.

6.2.3 PAGS

- Lower bainite was observed at 0.07 °C/s cooling rate with a fine PAGS, while increasing PAGS enhances the formation of granular bainite that has a bainitic ferrite matrix with martensite austenite (MA) islands.

- Higher transformation temperature induced by the larger PAGS leads to enhances granular bainite formation.
- Increasing PAGS leads to an increase in tempered martensite volume fraction due to auto-tempering at cooling rate of 3 ℃/s.

6.2.4 Tempering

- Bainitic and martensitic laths width increase during tempering stage.
- For granular bainite Blocky MA islands were more stable than needle-like MA islands during tempering.
- At 0.07 °C/s and 3.0°C/s cooling rates, after tempering for 6 h, there are a rapid equiaxed inter and intra precipitation carbides.

6.2.5 Mechanical Properties

- Finer PAGS increases the hardness value of as-cooled specimens. Also, increasing cooling rates increase hardness.
- Hardness values decrease as the tempering time increases.
- Hardness is sensitive to PAGS with bainitic microstructure.

6.3 Future work

This research has characterised that the effect of PAGS on microstructure evolution as a function of expected cooling rates for thick walled RPVs for next generation nuclear reactors.

Results and conclusions from this work have led to some potential paths for future work, which are listed below:

- As a result of poor mechanical behaviour of granular bainite, pre-tempering could be one method that could be used to modify the steel microstructure and mechanical properties such as fracture toughness and tensile strength. Conducting a pre-tempering stage before the main tempering stage at a lower temperature lower than carbide precipitation could lead to decomposition of MA to different phases such as ferrite, perlite, bainite, martensite and carbides that may have a positive effect of properties
- To complement this, work a detailed assessment of mechanical properties as a function of PAGS and cooling rate should be undertaken.
- Studying the physical properties for instance tensile test and impact toughness of SA508 G4N is widely vital to study the variation of PAGS and its effect on the

microstructure and its impact on the mechanical characterisation. Moreover, mapping properties models has potential to explore and compare tensile strength and toughness from unseen data. Thus, the model provides a data to map the distribution of strength and toughness in large components such as RPV.

- Owing to the significant effect on austenite grain growth, which directly influence hardenability and the mechanical properties of SA508 G4N steels, the precipitation behaviour of aluminium nitride be studied. The grain growth model should be improved to predict the precipitation kinetics, growth and dissolution behaviours and to simulate the distribution of size evolution of these nitrides undergoing various heat treatment, such as reheating or continuous cooling, would be desirable.

References

[1]“Nuclear Power Today | Nuclear Energy - World Nuclear Association.” [Online]. Available: https://www.world-nuclear.org/information-library/current-and-future-generation/nuclear-power-in-the-world-today.aspx. [Accessed: 13-Mar-2020].

[2]B. W. Brook, A. Alonso, D. A. Meneley, J. Misak, T. Blees, and J. B. van Erp, “Why nuclear energy is sustainable and has to be part of the energy mix,” *Sustain. Mater. Technol.*, vol. 1, pp. 8–16, 2014.

[3]A. A. Kiely, “Characterisation and interpretation of austenite grain growth kinetics in an advanced nuclear pressure vessel steel,” CAMBRIDGE UNIVERSITY, 2016.

[4]D. Bodansky, *NUCLEAR ENERGY PRINCIPLES, PRACTICES, AND PROSPECTS*, 2nd ed. New York: Springer-Verlag, 2004.

[5]T. J. Foxon, “Transition pathways for a UK low carbon electricity future,” *Energy Policy*, vol. 52, pp. 10–24, 2013.

[6]M. C. Kim, S.-G. Park, K. Lee, and B.-S. Lee, “Comparison of fracture properties in SA508 Gr.3 and Gr.4N high strength low alloy steels for advanced pressure vessel materials,” *Int. J. Press. Vessel. Pip.*, vol. 131, pp. 60–66, 2015.

[7]N. LIU, Z. LIU, X. HE, Z. YANG, and L. MA, “Hot Deformation Behavior of SA508GR. 4N Steel for Nuclear Reactor Pressure Vessels,” *J. Iron Steel Res. Int.*, vol. 23, no. 12, pp. 1342–1348, 2016.

[8]G. Yan, L. Han, C. Li, X. Luo, and J. Gu, “Effect of Macrosegregation on the Microstructure and Mechanical Properties of a Pressure-Vessel Steel,” *Metall. Mater. Trans. A Phys. Metall. Mater. Sci.*, vol. 48 A, no. 7, pp. 3470–3481, 2017.

[9]N. Huda, Y. Wang, L. Li, and A. P. Gerlich, “Effect of martensite-austenite (MA) distribution on mechanical properties of inter-critical Reheated Coarse Grain heat affected zone in X80 linepipe steel,” *Mater. Sci. Eng. A*, vol. 765, no. August, p. 138301, 2019.

[10] D. Dong, F. Chen, and Z. Cui, “Modeling of Austenite Grain Growth During Austenitization in a Low Alloy Steel,” *J. Mater. Eng. Perform.*, vol. 25, no. 1, pp. 152–164, 2016.

[11] S. G. Park, K. H. Lee, K. D. Min, M. C. Kim, and B. S. Lee, “Influence of the thermodynamic parameters on the temper embrittlement of SA508 Gr.4N Ni-Cr-Mo low alloy steel with variation of Ni, Cr and Mn contents,” *J. Nucl. Mater.*, vol. 426, pp. 1–8, 2012.

[12] S. G. Parka, M.-C. Kimb, B. S. Leeb, and D. M. Weea, “Comparison of the Microstructure & Segregation behavior between SA508 Gr.3 & SA508 Gr.4N High Strength Low Alloy RPV Steel,” in *Transactions of the Korean Nuclear Society Spring Meeting*, 2010, pp. 251–252.

[13] L. Kander, Š. Stejskalová, M. Šmátralová, P. Čížek, and P. Pustejovský, “Structure and properties of A508 Gr. 4N class 3 grade steel,” in *METAL 2013 - 22nd International Conference on Metallurgy and Materials, Conference Proceedings*, 2013, pp. 748–753.

[14] D. XIA *et al.*, “Mechanical Properties and Corrosion Resistance of SA508-4 Low

Carbon Alloy Steel," *Electrochemistry*, vol. 81, no. 4, pp. 262–268, 2013.

[15] S.-G. Park, K.-H. Lee, K.-D. Min, M.-C. Kim, and B.-S. Lee, "Characterization of phase fractions and misorientations on tempered Bainitic/Martensitic Ni-Cr-Mo low alloy RPV steel with various Ni content," *Met. Mater. Int.*, vol. 19, no. 1, pp. 49–54, 2013.

[16] R. Dippenaar, C. Bernhard, S. Schider, and G. Wieser, "Austenite grain growth and the surface quality of continuously cast steel," *Metall. Mater. Trans. B Process Metall. Mater. Process. Sci.*, vol. 45B, no. April, pp. 409–418, 2014.

[17] S. Specification, "Standard Specification for Quenched and Tempered Vacuum-Treated Carbon and Alloy Steel Forgings for Pressure Vessels 1," A508/A508M, 2016.

[18] "• Nuclear power plants worldwide 2018 | Statista." [Online]. Available: https://www.statista.com/statistics/263940/nuclear-power-plants-newly-connected-to-the-grid/. [Accessed: 13-Mar-2020].

[19] D. Dong, F. Chen, and Z. Cui, "A physically-based constitutive model for SA508-III steel: Modeling and experimental verification," *Mater. Sci. Eng. A*, vol. 634, pp. 103–115, 2015.

[20] M. Daly, "Advanced Imaging and Mechanistic Modelling of Ductile Fracture," The University of Manchester, 2014.

[21] M. Kim, B. Lee, K. Lee, and W. Kim, "Mechanical Properties of Sa508 Gr.4N Model Alloys As a High Strength Rpv Steel," *Proc. ASME 2010 Press. Vessel. Pip. Div. Conf. PVP 2010, July 18-22, 2010, Bellevue, Washington, USA*, pp. 1–6, 2015.

[22] B. Marini, X. Averty, P. Wident, P. Forget, and F. Barcelo, "Effect of the bainitic and martensitic microstructures on the hardening and embrittlement under neutron irradiation of a reactor pressure vessel steel," *J. Nucl. Mater.*, vol. 465, pp. 20–27, 2015.

[23] S. Kim, S. Lee, Y.-R. Im, H.-C. Lee, Y. J. Oh, and J. H. Hong, "Effects of alloying elements on mechanical and fracture properties of base metals and simulated heat-affected zones of SA 508 steels," *Metall. Mater. Trans. A*, vol. 32, no. APRIL, pp. 903–911, 2001.

[24] J. William D. Callister, *Materials Science and Engineering An Introduction*, 7th ed. New York: John Wiley & Sons, Inc., 2007.

[25] R. N. Penha, J. Vatavuk, A. A. Couto, S. A. de L. Pereira, S. A. de Sousa, and L. de C. F. Canale, "Effect of chemical banding on the local hardenability in AISI 4340 steel bar," *Eng. Fail. Anal.*, vol. 53, pp. 59–68, 2015.

[26] H. K. D. H. Bhadeshia, *Bainite in steels*, 3rd ed. London: CRC Press, 2015.

[27] S. A. Sajjadi and S. M. Zebarjad, "Isothermal transformation of austenite to bainite in high carbon steels," *J. Mater. Process. Technol.*, vol. 189, no. 1–3, pp. 107–113, 2007.

[28] S. D. Catteau *et al.*, "Carbon and nitrogen effects on microstructure and kinetics associated with bainitic transformation in a low-alloyed steel," *J. Alloys Compd.*, vol. 658, pp. 832–838, 2016.

[29] S. H. Bhadeshia and R. Honeycombe, *Steels, Microstructure and Properties*, 4th ed. Elsevier Ltd, 2006.

[30] Z. X. Qiao, Y. C. Liu, L. M. Yu, and Z. M. Gao, “Formation mechanism of granular bainite in a 30CrNi3MoV steel,” *J. Alloys Compd.*, vol. 475, pp. 560–564, 2009.

[31] S. M. C. van Bohemen and J. Sietsma, “The kinetics of bainite and martensite formation in steels during cooling,” *Mater. Sci. Eng. A*, vol. 527, no. 24–25, pp. 6672–6676, 2010.

[32] R. P. Garrett, S. Xu, J. Lin, and T. A. Dean, “A model for predicting austenite to bainite phase transformation in producing dual phase steels,” *Int. J. Mach. Tools Manuf.*, vol. 44, no. 7–8, pp. 831–837, 2004.

[33] P. J. JACQUES, J. L. RE, and F. Delannay, “On the Influence of Interactions between Phases on the Mechanical Stability of Retained Austenite in Transformation-Induced Plasticity Multiphase Steels,” *Metall. Mater. Trans. A*, vol. 32A, pp. 2759–2768, 2001.

[34] S. J. Lee and Y. K. Lee, “Prediction of austenite grain growth during austenitization of low alloy steels,” *Mater. Des.*, vol. 29, no. 9, pp. 1840–1844, 2008.

[35] H. Zhang, X. Cheng, B. Bai, and H. Fang, “The tempering behavior of granular structure in a Mn-series low carbon steel,” *Mater. Sci. Eng. A*, vol. 528, pp. 920–924, 2011.

[36] Z. Jiang, P. Wang, D. Li, and Y. Li, “Influence of the decomposition behavior of retained austenite during tempering on the mechanical properties of 2.25Cr-1Mo-0.25 V steel,” *Mater. Sci. Eng. A*, vol. 742, no. October 2018, pp. 540–552, 2019.

[37] N. Takayama, G. Miyamoto, and T. Furuhara, “Chemistry and three-dimensional morphology of martensite-austenite constituent in the bainite structure of low-carbon low-alloy steels,” *Acta Mater.*, vol. 145, pp. 154–164, 2018.

[38] A. S. Nishikawa, M. J. Santofimia, J. Sietsma, and H. Goldenstein, “Influence of bainite reaction on the kinetics of carbon redistribution during the Quenching and Partitioning process,” *Acta Mater.*, vol. 142, pp. 142–151, 2018.

[39] Z. Yang, Z. Liu, X. He, S. Qiao, and C. Xie, “Effect of microstructure on the impact toughness and temper embrittlement of SA508Gr.4N steel for advanced pressure vessel materials,” *Sci. Rep.*, vol. 8, no. 1, pp. 1–12, 2018.

[40] C. García De Andrés, F. G. Caballero, C. Capdevila, and L. F. Álvarez, “Application of dilatometric analysis to the study of solid-solid phase transformations in steels,” *Mater. Charact.*, vol. 48, pp. 101–111, 2002.

[41] S. Nambu, N. Shibuta, M. Ojima, J. Inoue, T. Koseki, and H. K. D. H. Bhadeshia, “In situ observations and crystallographic analysis of martensitic transformation in steel,” *Acta Mater.*, vol. 61, no. 13, pp. 4831–4839, 2013.

[42] Q. Luo, “A New XRD Method to Quantify Plate and Lath Martensites of Hardened Medium-Carbon Steel,” *J. Mater. Eng. Perform.*, vol. 25, pp. 2170–2179, 2016.

[43] S. Y. P. Allain, G. Geandier, J. C. Hell, M. Soler, F. Danoix, and M. Gouné, “Effects of Q&P processing conditions on austenite carbon enrichment studied by in situ high-energy X-ray diffraction experiments,” *Metals (Basel).*, vol. 7, pp. 232–245, 2017.

[44] B. S. Lee, M. C. Kim, J. H. Yoon, and J. H. Hong, “Characterization of high strength and high toughness Ni-Mo-Cr low alloy steels for nuclear application,” *Int. J. Press. Vessel. Pip.*, vol. 87, no. 1, pp. 74–80, 2010.

[45] M. Zhou, G. Xu, J. Tian, H. Hu, and Q. Yuan, “Bainitic transformation and properties

of low carbon carbide-free bainitic steels with Cr addition," *Metals (Basel).*, vol. 7, no. 7, pp. 1–13, 2017.

[46] J. Tian, G. Xu, M. Zhou, H. Hu, and X. Wan, "The effects of Cr and Al addition on transformation and properties in low-carbon bainitic steels," *Metals (Basel).*, vol. 7, pp. 1–11, 2017.

[47] J. Tian, G. Xu, Z. Jiang, X. Wan, H. Hu, and Q. Yuan, "Transformation Behavior and Properties of Carbide-Free Bainite Steels with Different Si Contents," *Steel Res. Int.*, vol. 90, no. 3, pp. 1–11, 2018.

[48] S. Kim, Y.-R. Im, S. Lee, H.-C. Lee, S.-J. Kim, and J. Hong, "Effects of alloying elements on fracture toughness in the transition temperature region of base metals and simulated heat-affected zones of Mn-Mo-Ni low-alloy steels," *Metall. Mater. Trans. A*, vol. 35, no. 7, pp. 2027–2037, 2004.

[49] H. K. Se-Hwan Chi, Jun-Hwa Hong, "Irradiation Induced Tensile Property Change of SA 508 Cl 3 Reactor Pressure Vessel Steels," *IGORR*, no. 042, pp. 455–477, 1998.

[50] H. Hu, G. Xu, L. Wang, Z. Xue, Y. Zhang, and G. Liu, "The effects of Nb and Mo addition on transformation and properties in low carbon bainitic steels," *Mater. Des.*, vol. 84, pp. 95–99, 2015.

[51] Y. R. Im, Y. J. Oh, B. J. Lee, J. H. Hong, and H. C. Lee, "Effects of carbide precipitation on the strength and Charpy impact properties of low carbon Mn-Ni-Mo bainitic steels," *J. Nucl. Mater.*, vol. 297, pp. 138–148, 2001.

[52] K.-H. Lee, S. Park, M.-C. Kim, B.-S. Lee, and D.-M. Wee, "Characterization of transition behavior in SA508 Gr.4N Ni-Cr-Mo low alloy steels with microstructural alteration by Ni and Cr contents," *Mater. Sci. Eng. A*, vol. 529, no. 1, pp. 156–163, 2011.

[53] S. G. Park, M. C. Kim, B. S. Lee, and D. M. Wee, "Thermodynamic calculation and observation of microstructural change in Ni-Mo-Cr high strength low alloy RPV steels with alloying elements," *J. Korean Inst. Met. Mater.*, vol. 46, pp. 771–779, 2008.

[54] T. Wen, X. Hu, Y. Song, D. Yan, and L. Rong, "Carbides and mechanical properties in a Fe-Cr-Ni-Mo high-strength steel with different V contents," *Mater. Sci. Eng. A*, vol. 588, pp. 201–207, 2013.

[55] A. Grajcar, W. Zalecki, P. Skrzypczyk, A. Kilarski, A. Kowalski, and S. Kołodziej, "Dilatometric study of phase transformations in advanced high-strength bainitic steel," *J. Therm. Anal. Calorim.*, vol. 118, pp. 739–748, 2014.

[56] A. Navarro-López, J. Sietsma, and M. J. Santofimia, "Effect of Prior Athermal Martensite on the Isothermal Transformation Kinetics Below M s in a Low-C High-Si Steel," *Metall. Mater. Trans. A*, vol. 47, pp. 1028–1039, 2016.

[57] W. bo Liu, P. cheng Song, C. Zhang, D. Yun, C. fa Yao, and Z. gang Yang, "Crystallographic analysis of lath martensite in a 13Cr-5Ni steel by electron backscattering diffraction," *J. Iron Steel Res. Int.*, vol. 25, pp. 213–220, 2018.

[58] H. K. D. H. B. and B. P. H. Pous-Romero, J. Talamantes-Silva, S. S. Al-Bermani and Wynn, "The Prediction of Toughness and Strength in High Integrity Forgings," in *The 19th international Forgemasters meeting*, 2014, pp. 502–506.

[59] G. L. F. A. R. H. GEILS, "A Method for Obtaining Quantitative Dilatometric Data

from Alloys Undergoing a Phase Transformation," *Metallography*, vol. 3, pp. 229–233, 1970.

[60] Y.-J. Yang, J.-X. Fu, R.-J. Zhao, and Y.-X. Wu, "Dilatometric Analysis of Phase Fractions during Austenite Decomposition in Pipeline Steel," in *3rd International Conference on Material, Mechanical and Manufacturing Engineering*, 2015, no. IC3ME, pp. 1974–1978.

[61] H. P. Romero, "Quantitative basis for the structure and properties of a critically-important pressure vessel steel," University of Cambridge, 2014.

[62] X. Zhou, C. Liu, L. Yu, Y. Liu, and H. Li, "Phase Transformation Behavior and Microstructural Control of High-Cr Martensitic/Ferritic Heat-resistant Steels for Power and Nuclear Plants: A Review," *J. Mater. Sci. Technol.*, vol. 31, no. 3, pp. 235–242, 2015.

[63] H. Xikou, L. Zhengdong, Z. Yang, W. Xiaobin, and F. Caishum, "Austenite Grain Growth Behavior of SA508-4N steel for Nuclear Pressure Vessel," *Heat Treat. Met.*, vol. 41, no. 6, pp. 41–47, 2016.

[64] K.-H. Lee, M. J. Jhung, M. C. Kim, and B. S. Lee, "Effects of tempering and PWHT on microstructures and mechanical properties of SA508 GR.4N steel," *Nucl. Eng. Technol.*, vol. 46, no. 3, pp. 413–422, 2014.

[65] Y. Ju, A. Goodall, M. Strangwood, and C. Davis, "Characterisation of precipitation and carbide coarsening in low carbon low alloy Q&T steels during the early stages of tempering," *Mater. Sci. Eng. A*, vol. 738, no. August, pp. 174–189, 2018.

[66] C. Li, L. Han, G. Yan, Q. Liu, X. Luo, and J. Gu, "Time-dependent temper embrittlement of reactor pressure vessel steel: Correlation between microstructural evolution and mechanical properties during tempering at 650 °C," *J. Nucl. Mater.*, vol. 480, pp. 344–354, 2016.

[67] H. Pous-Romero, I. Lonardelli, D. Cogswell, and H. K. D. H. Bhadeshia, "Austenite grain growth in a nuclear pressure vessel steel," *Mater. Sci. Eng. A*, vol. 567, pp. 72–79, 2013.

[68] N. Kozlov and O. Keßler, "Influencing on liquid quenching by surface structuring," *Int. J. Therm. Sci.*, vol. 101, pp. 133–142, 2016.

[69] M. Durand-Charre, "The decomposition of austenite," in *Microstructure of Steels and Cast Irons*, 2004th ed., New York: Springer-Verlag Berlin Heidelberg, 2004, pp. 179–193.

[70] S. H. Talebi, M. Jahazi, and H. Melkonyan, "Retained austenite decomposition and carbide precipitation during isothermal tempering of a medium-carbon low-alloy bainitic steel," *Materials (Basel).*, vol. 11, no. 8, pp. 1–12, 2018.

[71] G. E. Totten, *Steel heat treatment: Metallurgy and technologies*, 2nd ed. CRC Taylor & Francis Group, 2007.

[72] D. C. Saha, E. Biro, A. P. Gerlich, and Y. Zhou, "Effects of tempering mode on the structural changes of martensite," *Mater. Sci. Eng. A*, vol. 673, pp. 467–475, 2016.

[73] L. C. F. Canale, X. Yao, J. Gu, and G. E. Totten, "A historical overview of steel tempering parameters," *Int. J. Microstruct. Mater. Prop.*, vol. 3, no. 4–5, pp. 474–525, 2008.

[74] “What Happens During Tempering of Steel? - Knife Steel Nerds.” [Online]. Available: https://knifesteelnerds.com/2018/04/23/what-happens-during-tempering-of-steel/. [Accessed: 17-Mar-2020].

[75] W. Li, M. Cai, D. Wang, J. Zhang, S. Zhao, and P. Shao, “Studying on tempering transformation and internal friction for low carbon bainitic steel,” *Mater. Sci. Eng. A*, vol. 679, pp. 410–416, 2017.

[76] L. S. Kremnev, “Structure and mechanism of the formation of granular bainite in steel 20Kh2NACh,” *Met. Sci. Heat Treat.*, vol. 39, pp. 367–370, 1997.

[77] X. Liu, F. Yuan, and Y. Wei, “Grain size effect on the hardness of nanocrystal measured by the nanosize indenter,” *Appl. Surf. Sci.*, vol. 279, pp. 159–166, 2013.

[78] J. Reiter, C. Bernhard, and H. Presslinger, “Austenite grain size in the continuous casting process : Metallographic methods and evaluation,” *Mater. Charact.*, vol. 59, pp. 737–746, 2007.

[79] A. Lambert-Perlade, A. F. Gourgues, and A. Pineau, “Austenite to bainite phase transformation in the heat-affected zone of a high strength low alloy steel,” *Acta Mater.*, vol. 52, no. 8, pp. 2337–2348, 2004.

[80] a. Matsuzaki and H. K. D. H. Bhadeshia, “Effect of austenite grain size and bainite morphology on overall kinetics of bainite transformation in steels,” *Mater. Sci. Technol.*, vol. 15, no. 5, pp. 518–522, 1999.

[81] J. Barford, W. Owen, “The effect of austenite grain size and temperature on the rate of bainite transformation,” *J. Iron Steel Inst.*, vol. 197, no. 2, pp. 359–360, 1961.

[82] S. YAMAMOTO, H. Yakoyama, K. Yamada, and M. Niicura, “Effects of the Austenite Grain Size and Deformation in the Unrecrystallized Austenite Region on Bainite Transformation Behavior and Microsturcture,” *ISIJ Int.*, vol. 35, pp. 1020–1026, 1995.

[83] G. E. Dieter, *Mechanical metallurgy.*, 3rd ed. London, UK, 1989.

[84] S. D. Tanner, V. I. Baranov, O. I. Ornatsky, D. R. Bandura, and T. C. George, *An introduction to mass cytometry: Fundamentals and applications*. Wiley VCH, 2012.

[85] A. Di Schino and C. Guarnaschelli, “Effect of microstructure on cleavage resistance of high-strength quenched and tempered steels,” *Mater. Lett.*, vol. 63, pp. 1968–1972, 2009.

[86] K. H. Lee, S. G. Park, M. C. Kim, and B. S. Lee, “Cleavage fracture toughness of tempered martensitic Ni-Cr-Mo low alloy steel with different martensite fraction,” *Mater. Sci. Eng. A*, vol. 534, pp. 75–82, 2012.

[87] L. Morsdorf, O. Jeannin, D. Barbier, M. Mitsuhara, D. Raabe, and C. C. Tasan, “Multiple mechanisms of lath martensite plasticity,” *Acta Mater.*, vol. 121, pp. 202–214, 2016.

[88] M. Yang, S. L. Long, and Y. L. Liang, “Study on the key role of hierarchical microstructure for strength and plasticity in a lath martensitic steel,” *IOP Conf. Ser. Mater. Sci. Eng.*, vol. 324, no. 1, pp. 1–6, 2018.

[89] H. Kitahara, R. Ueji, N. Tsuji, and Y. Minamino, “Crystallographic features of lath martensite in low-carbon steel,” *Acta Mater.*, vol. 54, no. 5, pp. 1279–1288, 2006.

[90] T. Hanamura, S. Torizuka, S. Tamura, S. Enokida, and H. Takechi, “Effect of austenite grain size on transformation behavior, microstructure and mechanical properties of 0.1C-5Mn martensitic steel,” *ISIJ Int.*, vol. 53, no. 12, pp. 2218–2225, 2013.

[91] J. Han *et al.*, “The effects of prior austenite grain boundaries and microstructural morphology on the impact toughness of intercritically annealed medium Mn steel,” *Acta Mater.*, vol. 122, pp. 199–206, 2017.

[92] S. Morito, X. Huang, T. Furuhara, T. Maki, and N. Hansen, “The morphology and crystallography of lath martensite in alloy steels,” *Acta Mater.*, vol. 54, no. 19, pp. 5323–5331, 2006.

[93] JAROMIR MORAVEC, “DETERMINATION OF THE GRAIN GROWTH KINETICS AS A BASE PARAMETER FOR NUMERICAL SIMULATION DEMAND,” *Sci. J.*, 2015.

[94] H. K. D. H. Bhadeshia, “Design of ferritic creep-resistant steels,” *ISIJ Int.*, vol. 41, no. 6, pp. 626–640, 2001.

[95] R. Xing, D. Yu, G. Xie, Z. Yang, X. Wang, and X. Chen, “Effect of thermal aging on mechanical properties of a bainitic forging steel for reactor pressure vessel,” *Mater. Sci. Eng. A*, vol. 720, no. December 2017, pp. 169–175, 2018.

[96] T. H. Lee, Y. J. Lee, S. H. Joo, H. H. Nersisyan, K. T. Park, and J. H. Lee, “Intergranular M23C6 Carbide Precipitation Behavior and Its Effect on Mechanical Properties of Inconel 690 Tubes,” *Metall. Mater. Trans. A Phys. Metall. Mater. Sci.*, vol. 46, pp. 4020–4026, 2015.

[97] H. Sun and Y. Shi, “Investigation on hall-petch relationship in electrodeposited nanocrystalline Cu-Ni-P alloys,” *J. Mater. Sci. Technol.*, vol. 25, no. 3, pp. 347–350, 2009.

[98] J. Cornide, C. Garcia-Mateo, C. Capdevila, and F. G. Caballero, “An assessment of the contributing factors to the nanoscale structural refinement of advanced bainitic steels,” *J. Alloys Compd.*, vol. S577, pp. S43–S47, 2013.

[99] C. Lu, Y. He, Z. Gao, J. Yang, W. Jin, and Z. Xie, “Microstructural evolution and mechanical characterization for the A508–3 steel before and after phase transition,” *J. Nucl. Mater.*, vol. 495, pp. 103–110, 2017.

[100] S. Pallaspuro, S. Mehtonen, J. Kömi, Z. Zhang, and D. Porter, “Effects of local grain size and inclusions on the low-temperature toughness of low-carbon as-quenched martensite,” *Mater. Sci. Eng. A*, vol. 743, no. August 2018, pp. 611–622, 2019.

[101] G. Gao, B. Zhang, C. Cheng, P. Zhao, H. Zhang, and B. Bai, “Very high cycle fatigue behaviors of bainite/martensite multiphase steel treated by quenching-partitioning-tempering process,” *Int. J. Fatigue*, vol. 92, pp. 203–210, 2016.

[102] P. Hughes and W. Flores, “The Effects of Large Scale Forgings and Heat Treatment on the Mechanical Performance of Mooring Connectors,” in *Offshore Technology Conference*, 2010.

[103] H. Zhao, B. P. Wynne, and E. J. Palmiere, “Effect of austenite grain size on the bainitic ferrite morphology and grain refinement of a pipeline steel after continuous cooling,” *Mater. Charact.*, vol. 123, pp. 128–136, 2017.

[104] S. Sun and A. Zhao, “Effect of microstructure morphology on mechanical properties of

quenching and partitioning steel," *Mater. Sci. Technol. (United Kingdom)*, vol. 34, no. 3, pp. 347–354, 2018.

[105] J. H. Chen, G. Z. Wang, Q. Wang, and Y. G. Liu, "Effects of sizes of ferrite grains and carbide particles on toughness of notched and precracked specimens of low-alloy steels," *Int. J. Fract.*, vol. 126, pp. 223–241, 2004.

[106] X. Z. Zhang and J. F. Knott, "Cleavage fracture in bainitic and martensitic microstructures," *Acta Mater.*, vol. 47, no. 12, pp. 3483–3495, 1999.

[107] ASTM, "ASTM E112-13: Standard test methods for determining average grain size," 2013.

[108] S. Song, Z. Yuan, D. Shen, and L. Weng, "Effects of phosphorus grain boundary segregation and hardness on the ductile-to-brittle transition for a 2.25Cr1Mo steel," *J. Wuhan Univ. Technol. Mater. Sci. Ed.*, vol. 22, no. 1, pp. 1–6, 2007.

[109] H. Pous-Romero and H. Bhadeshia, "Coalesced Martensite in Pressure Vessel Steels," *J. Press. Vessel Technol.*, vol. 136, no. 3, pp. 031402-1-031402–6, 2014.

[110] R. Radis and E. Kozeschnik, "Kinetics of AlN precipitation in microalloyed steel," *Model. Simul. Mater. Sci. Eng.*, vol. 18, no. 5, 2010.

[111] K. Zhu, H. Chen, J. P. Masse, O. Bouaziz, and G. Gachet, "The effect of prior ferrite formation on bainite and martensite transformation kinetics in advanced high-strength steels," *Acta Mater.*, vol. 61, no. 16, pp. 6025–6036, 2013.

[112] D. ZHANG, "Characterisation and Modelling of Segregation in continuously cast Steel Slab," The University of Birmingham, 2015.

[113] C. Sun, P. Fu, H. Liu, H. Liu, N. Du, and Y. Cao, "crystals The Effect of Lath Martensite Microstructures on the Strength of Medium-Carbon Low-Alloy Steel," *Crystals*, vol. 10, p. 232, 2020.

[114] S. Morito, H. Saito, T. Maki, and T. Furuhara, "Effect of PAGS on crystallography and morphology of lath martensite in low carbon steels," *ISIJ Int.*, vol. 45, no. 1, pp. 91–94, 2004.

[115] J. W. Morris, C. Kinney, K. Pytlewski, and Y. Adachi, "Microstructure and cleavage in lath martensitic steels," *Sci. Technol. Adv. Mater.*, vol. 14, no. 1, 2013.

[116] W. Bleck and F. Gerdemann, "Improved mechanical properties by control of bainite transformation," *Mater. Manuf. Process.*, vol. 26, no. 1, pp. 43–50, 2011.

[117] S. Hesamodin Talebi, H. Ghasemi-Nanesa, M. Jahazi, and H. Melkonyan, "In situ study of phase transformations during non-isothermal tempering of bainitic and martensitic microstructures," *Metals (Basel).*, vol. 7, 2017.

[118] C. H. Young and H. K. D. H. Bhadeshia, "Strength of mixtures of bainite and martensite," *Mater. Sci. Technol. (United Kingdom)*, vol. 10, pp. 209–214, 1994.

[119] K. Tamaki and J. Suzuki, "precipitation of carbide during tempering of Cr-Mo steels," *Res. Re[. Fac. Eng. Mie Univ*, vol. 7, no. 1982, pp. 39–52, 1982.

[120] L. Lan, M. Yu, and C. Qiu, "On the local mechanical properties of isothermally transformed bainite in low carbon steel," *Mater. Sci. Eng. A*, vol. 742, no. August 2018, pp. 442–450, 2019.

[121] Y. Zhou, T. Jia, X. Zhang, Z. Liu, and R. D. K. Misra, "Investigation on tempering of

granular bainite in an offshore platform steel," *Mater. Sci. Eng. A*, vol. 626, pp. 352–361, 2015.

[122] S. H. He, B. B. He, K. Y. Zhu, R. Ding, H. Chen, and M. X. Huang, "Revealing the role of dislocations on the stability of retained austenite in a tempered bainite," *Scr. Mater.*, vol. 168, pp. 23–27, 2019.

[123] X. C. Xiong, B. Chen, M. X. Huang, J. F. Wang, and L. Wang, "The effect of morphology on the stability of retained austenite in a quenched and partitioned steel," *Scr. Mater.*, vol. 68, no. 5, pp. 321–324, 2013.

[124] S. C. Kennett, G. Krauss, and K. O. Findley, "Prior austenite grain size and tempering effects on the dislocation density of low-C Nb-Ti microalloyed lath martensite," *Scr. Mater.*, vol. 107, pp. 123–126, 2015.

[125] Z. Zhang, D. Delagnes, and G. Bernhart, "Microstructure evolution of hot-work tool steels during tempering and definition of a kinetic law based on hardness measurements," *Mater. Sci. Eng. A*, vol. 380, no. 1, pp. 222–230, 2004.